NASA Technical Paper 1653

Application of Two Design Methods for Active Flutter Suppression and Wind-Tunnel Test Results

Jerry R. Newsom, Irving Abel,
and H. J. Dunn

MAY 1980

NASA

NASA Technical Paper 1653

Application of Two Design Methods for Active Flutter Suppression and Wind-Tunnel Test Results

Jerry R. Newsom, Irving Abel,
and H. J. Dunn
Langley Research Center
Hampton, Virginia

National Aeronautics
and Space Administration

**Scientific and Technical
Information Office**

1980

SUMMARY

The synthesis, implementation, and wind-tunnel test of two flutter-suppression control laws for an aeroelastic model equipped with a trailing-edge control surface are presented. One control law is based on the aerodynamic energy method, and the other is based on results of optimal control theory. Analytical methods used to design the control laws and evaluate their performance are described. The test objective was to demonstrate an increase in flutter dynamic pressure of at least 44 percent over a range of Mach numbers by using active flutter suppression. At Mach 0.6, 0.8, and 0.9, increases in flutter dynamic pressure were obtained but the full 44-percent increase was not achieved. However at Mach 0.95, the 44-percent increase was achieved with both control laws. Experimental results indicate that the performance of the systems is not so effective as that predicted by analysis. Also, the results indicate that wind-tunnel turbulence plays an important role in both control-law synthesis and demonstration of system performance.

INTRODUCTION

Application of active control technology, such as gust and maneuver load alleviation and flutter suppression, offers the potential for substantial payoffs in terms of reduced structural mass (ref. 1). Because of its impact on safety of flight in case of system failure, active flutter suppression is probably further from application in production aircraft than other active control concepts. In order to reduce technical risks and explore the full benefits of active flutter suppression, research is underway to advance this technology with analytical studies (e.g., refs. 2 and 3), wind-tunnel studies (refs. 4 and 5), and flight experiments with both full-scale aircraft and remotely piloted drones (refs. 6 and 7).

Two methods that have been proposed for synthesizing active flutter-suppression control laws are the relaxed aerodynamic energy method (ref. 8) and the optimal control theory (ref. 9). The method described in reference 8 takes into account advances in the aerodynamic energy method since it was originally developed in reference 10. The optimal control-theory method involves the practical implementation of an optimal control law from a very limited number of feedback sensors.

The purpose of this paper is to report on the design of two flutter-suppression control laws which were synthesized by using these methods and to present results of wind-tunnel tests of their performance. The aeroelastic model used for this study is described in reference 11 and was tested previously to evaluate the performance of a flutter-suppression system. The objective of this study was to design control laws which would demonstrate at least a 44-percent increase in flutter dynamic pressure (20-percent increase in flutter velocity) in the Mach number range from 0.6 to 0.9.

Aeroelastic analysis techniques used to calculate system performance are presented in appendix A. Numerical results from applying the aerodynamic energy and optimal control-theory synthesis techniques are presented in appendixes B and C, respectively. A description of the mechanization of the control laws is presented in appendix D.

SYMBOLS

a_1, a_2	control-law gains, aerodynamic energy method
b	reference semichord, m
b_r	semichord length at spanwise location of inboard accelerometer, m
C(s)	Laplace transform of output
c	local chord, m
dt	differential time
f	frequency, Hz
f(s)	polynomial factor in feedback filter
g	acceleration in gravitational units, $1g = 9.8\ m/sec^2$
G(s)	transfer function relating wing motion to control-surface deflection
H(s)	transfer function relating control-surface deflection to wing motion
$H_\delta(i\omega)$	control-surface frequency-response function
h	vertical displacement, m
$\ddot{h}$	vertical acceleration, g units
I_v	servovalve current
i	$= \sqrt{-1}$
J	cost function
K_f	filter gain
K_p	pressure gain in servo-actuator loop
K_v	forward gain in servo-actuator loop
k	reduced frequency, $\omega b/V$

L	reference length used in gust spectrum, m
M	Mach number
PSD	power spectral density
Δp	differential pressure across actuator
Q	hydraulic fluid flow rate
$Q(s)$	common denominator of transfer functions
q	dynamic pressure, $\frac{1}{2}\rho V^2$, kPa
q_{max}	= 1.44 × Calculated q_f
$R(s)$	Laplace transform of reference input
s	Laplace variable
u	control input
$\bar{u}$	optimal control input
$\hat{u}$	practical control input
V	free-stream velocity, m/sec
w_g	gust velocity, m/sec
α	angle of attack at spanwise location of inboard accelerometer
$\beta_1, \ldots, \beta_4$	aerodynamic lag
δ_a	control-surface deflection
δ_c	control-surface command to actuator
δ_c'	control-surface command from control law
ζ	viscous-damping coefficient
ρ	fluid density, kg/m^3
σ_{w_g}	root-mean-square gust velocity, m/sec
ϕ	phase angle of $G(i\omega)\ H(i\omega)$

$\phi_I(\omega)$ input gust power spectrum (Von Kármán)

ϕ_m phase margin

$\phi_o(\omega)$ output power spectrum of control-surface response

ω circular frequency, rad/sec

ω_n natural frequency, rad/sec

Matrices:

$[A]$ system dynamics matrix, open loop

$[\bar{A}]$ system dynamics matrix for optimal control-law synthesis

$[A_i]$ real aerodynamic coefficient matrix

$\{B\}$ control distribution vector

$[C_\phi]$ row matrix of mode-shape amplitudes

$[F_i]$ real coefficients of equations of motion

$\{G_i\}$ real gust-velocity coefficients in equations of motion

$[I]$ identity matrix

$[K]$ generalized stiffness matrix

$[K^*]$ optimal gain matrix

$[M]$ generalized mass matrix

$[Q]$ output weighting matrix

$[\hat{Q}]$ matrix representing approximate aerodynamic forces in Laplace plane

$\{q\}$ generalized coordinate vector

$[R]$ control weighting matrix

$[T]$ transfer function matrix

$[T_N]$ transfer function numerator matrix

$\{u\}$ control vector

$\{X\}$ state variable vector

$\{\bar{X}\}$ state variable vector for optimal control-law synthesis

$\{Y\}$ output vector

$[\phi]$ matrix of modal deflections at sensor location

Subscripts:

f flutter

inbd location of inboard accelerometer

outbd location of outboard accelerometer

peak peak value

rms root-mean-square value

0.65c 65-percent chord

0.30c 30-percent chord

Dots over symbols denote derivative with respect to time.

AEROELASTIC MODEL AND ANALYSIS METHOD

The aeroelastic model used for this study was originally built to support the DAST (Drones for Aerodynamic and Structural Testing) flight program (ref. 7). The model is a dynamically scaled representation of a transport-type research wing and is scaled to flutter within the operational limits of the Langley Transonic Dynamics Tunnel. The model is equipped with a hydraulically actuated trailing-edge control surface which is located between the 76.3-percent and 89.3-percent semispan stations and is 20 percent of the local wing chord. A photograph of the model mounted in the wind tunnel is presented in figure 1; its geometry is given in figure 2.

Structural Model

The bending and torsional stiffness of the model is provided by a single aluminum spar of uniform cross section. Airfoil sections, constructed of balsa wood and fiber glass, are attached to the spar in such a manner as not to contribute to the bending and torsional stiffness of the wing.

For aeroelastic analysis purposes, the first 10 elastic modes were calculated by using a finite-element model of the spar with airfoil sections represented as lump masses. The calculated frequencies, which cover a range of 5.23 to 118.15 Hz, and generalized masses for these modes are presented in table I. Prior to wind-tunnel tests, six modal frequencies and mode lines were experimentally determined (mode 3, which is a fore and aft mode, was not measured) and are presented in figure 3.

Actuator Model

The control surface is driven by an electrohydraulic servo-actuator system similar to that described in reference 4. The servo-actuator loop serves two functions: For zero command inputs it maintains a fixed control-surface position relative to the wing; and for time varying inputs, it provides control-surface motion in a manner dictated by the control law over its operating frequency range. Control-surface displacement and rate capabilities for this actuator are approximately $\pm 14^{o}$ and 820 deg/sec, respectively.

During previous wind-tunnel tests of this model (ref. 11), the actuator transfer function was experimentally measured. During those previous tests, a 100-Hz double-pole filter was added to the actuator electronics to decouple the actuator from higher frequency structural modes. The combination of the filter and actuator results in a transfer function associated with implementing the control-system hardware. The following actuator transfer function was used during the design process to model the actuator dynamics and filter:

$$\frac{a(s)}{c'(s)} = \frac{1.915 \times 10^{7}}{(s + 214)(s^{2} + 179.4s + 8.945 \times 10^{4})} \times \frac{100 \times 2}{(s + 100 \times 2)^{2}} \frac{\text{deg}}{\text{deg}} \qquad (1)$$

Aerodynamic Model

Unsteady aerodynamic forces for the wing and control surface were computed for different values of reduced frequency and Mach number by using a doublet lattice aerodynamic computer program. The aerodynamic model used in this study is described in reference 11. Unsteady aerodynamic forces were calculated for the first 10 calculated structural modes, for a control-surface rotation, and for a sinusoidal gust.

Analysis Method

For analysis purposes the structure, the control-surface actuator, and the unsteady aerodynamic models are combined by approximating the variation in frequency of the unsteady aerodynamics with a rational polynomial in the variable s. A description of the analysis methods used to calculate the flutter characteristics and the control-surface activity due to gusts is presented in appendix A.

CONTROL LAWS

A block diagram of the two control laws that were designed for the wind-tunnel model is given in figure 4. The synthesis techniques used were the aerodynamic energy method and the optimal control theory. Details of the synthesis methodology for each of these techniques are presented.

Because the physical size and location of the control surface were fixed on the model, these quantities were not varied during the control-law design process. Two locations for measuring wing accelerations were considered. (See fig. 2.) The location of the inboard accelerometer is that specified by the aerodynamic energy method. The outboard accelerometer is located at the position used during the previous wind-tunnel tests (ref. 11). The inboard accelerometer was used in the aerodynamic energy method, and the outboard accelerometer was used in the optimal control-theory technique. In order to show the difference in the mode shapes at the accelerometer locations, calculated modal displacements in each of the flexible modes for both accelerometer locations are given in table I.

The design point selected for control-law synthesis was $M = 0.9$; $q = 7.72$ kPa. This design-point dynamic pressure corresponds to a 44-percent increase in the measured flutter dynamic pressure of reference 11. System performance was then evaluated at $M = 0.6$, 0.7, and 0.8 to insure that the control laws performed satisfactorily at off-design points.

Some Design Considerations

As stated previously, the objective of this study was to design control laws and to demonstrate experimentally their capability of providing at least a 44-percent increase in flutter dynamic pressure at Mach numbers from 0.6 to 0.9. This increase is illustrated in figure 5 (denoted by q_{max}) and is based on the calculated system-off flutter characteristics. In order to demonstrate this increase in flutter dynamic pressure, the active control system must operate in the presence of tunnel turbulence within the rate and deflection limits of the actuator.

For design and analysis purposes a model of tunnel turbulence is required. Measured values of tunnel turbulence (velocity fluctuations) were not available. A gust analysis was performed in reference 11 by using a Von Kármán turbulence spectrum in which the characteristic length was varied until the calculated root-mean-square (rms) control-surface deflection matched the corresponding experimental data. Although this turbulence spectrum may not be an accurate representation of the tunnel turbulence, it did provide a reasonable measure of control-surface deflection over the range of dynamic pressures encountered during the previous tests. Based on these results, a Von Kármán turbulence spectrum with a characteristic length of 30.48 m and an intensity of 0.30 m/sec was used in the design of the control laws.

The commanded control-surface deflection and rate in response to tunnel turbulence led to design goals on allowable rms control-surface deflection and rate. Based on previous experimental results of an active flutter-suppression system that was tested on this model, control-surface deflection was the critical factor; it is shown in reference 11 that rms control-surface deflections of 6.5° corresponded to commanded peak deflections greater than the $\pm 14^{\circ}$ available from the actuator. Therefore, in the present design study, predicted rms control-surface deflection to tunnel turbulence should be less than 6° rms for dynamic pressures up to q_{max} at all Mach numbers considered. No specific

constraint was placed on control-surface rate, except that the predicted peak rate must be within the actuator limit (820 deg/sec) for a peak to rms ratio the same as that considered for control-surface deflection $\left(\text{i.e., } \frac{\dot{\delta}_{a,peak}}{\dot{\delta}_{a,rms}} \leqq \frac{14}{6}\right.$ or $\left.\dot{\delta}_{a,rms} \leqq 351 \text{ deg/sec}\right)$.

The resulting design goals were:

(1) At M = 0.6, 0.7, 0.8, and 0.9, the model will demonstrate at least a 44-percent increase in flutter dynamic pressure above the system-off boundary.

(2) Maximum control-surface deflections due to turbulence will be $\leqq 6^{\circ}$ rms.

(3) At M = 0.6, 0.7, 0.8, and 0.9, the active flutter-suppression system will have a minimum ±6-dB gain margin at all dynamic pressures up to q_{max} to account for uncertainties in the design.

Synthesis Using Aerodynamic Energy Method

The control law used in this work is referred to in reference 12 as a localized-type transfer function. For a single trailing-edge control surface the general form of this control law is expressed as

$$\delta_c'(s) = \begin{bmatrix} 0 & -1.86 \end{bmatrix} + \left(\frac{a_1 s^2}{s^2 + 2\zeta_1 \omega_1 s + \omega_1^2} + \frac{a_2 s^2}{s^2 + 2\zeta_2 \omega_2 s + \omega_2^2} \right) \begin{bmatrix} 4 & 2.8 \end{bmatrix} \begin{Bmatrix} \frac{h_{0.30c}}{b_r} \\ \alpha \end{Bmatrix} \tag{2}$$

where a_1, ζ_1, ω_1, a_2, ζ_2, and ω_2 are positive free parameters. These parameters permit the general form of the control law to be applied to a specific problem. The matrix coefficients 0, -1.86, 4, and 2.8 are derived in reference 12 for a two-dimensional wing (i.e., the case of a wing undergoing simple harmonic motion in pitch and plunge). The objective in this study is to apply the method to a three-dimensional problem.

For the present application, the constant term $\begin{bmatrix} 0 & -1.86 \end{bmatrix}$ is deleted and through a simple transformation (ref. 12) the terms $h_{0.30c}$ and α are replaced by a single term $h_{0.65c}$. These modifications are made to simplify the implementation of the control law. The form of the control law used in the present study becomes

$$\delta_c'(s) = \left(\frac{a_1 s^2}{s^2 + 2\zeta_1 \omega_1 s + \omega_1^2} + \frac{a_2 s^2}{s^2 + 2\zeta_2 \omega_2 s + \omega_2^2} \right) \frac{4h_{0.65c}}{b_r} \tag{3}$$

Reference 8 presents an approach for determining the free parameters in equation (3) that provide the required stability while maintaining minimum control-surface activity in response to turbulence. For this study the effects of the actuator and the goal of providing a ±6-dB gain margin are included in the synthesis procedure. The following steps are used to synthesize the control law:

Step 1: Assign initial values to the free parameters in equation (3) that stabilize the wing at the design Mach number and dynamic pressure.

Step 2: With the values of free parameters from step 1, determine new values of the free parameters which result in minimum control deflection in a continuous gust analysis at the design point.

Step 3: Determine control activity due to turbulence over a range of tunnel conditions to insure that the off-design goals are satisfied.

Step 4: Add the actuator transfer function and determine its effect on stability.

Step 5: Based on the results of step 4, design a compensator that provides a minimum of ±6-dB gain margin at the maximum dynamic pressure for each Mach number considered.

Step 6: Determine control-surface activity for the system including compensator and compare with the results of step 3; modify compensator if necessary.

Step 7: Check system stability over a range of Mach numbers and dynamic pressures.

By applying these steps, the following transfer function was synthesized for the wind-tunnel-model control law:

$$\frac{\delta_a(s)}{\ddot{h}_{inbd}} = \left(\frac{\delta_a}{\delta_c'} \right) \frac{147.35(s + 78)}{\left[s^2 + 2(1)5.9s + 5.9^2 \right]} \frac{\text{deg}}{g} \tag{4}$$

where $\ddot{h}_{0.65c} = \ddot{h}_{inbd}$. Numerical results are presented in appendix B. As shown in this appendix, the control law meets all the goals of the design except the 6-dB gain margin at M = 0.8 and 0.9. However the static gain of the control law, that is,

$$\left.\frac{\delta_a}{\ddot{h}_{inbd}}\right|_{@s=0} = 50 \text{ dB}$$

is quite large and could result in a static deflection of the control surface due to direct-current drift in the accelerometer output. In order to reduce the static gain while minimizing changes at the higher frequencies, an arbitrary filter of the form $s/(s + 10)$ was added to the control law defined by equation (4). This filter reduced the static gain to zero while adding less than 10° of phase lag at the flutter frequency. When this filter was added to the control law defined by equation (4), the overall system gain had to be adjusted slightly to maintain the -6-dB gain margin for all Mach numbers. The resulting control law is

$$\frac{\delta_a(s)}{\ddot{h}_{inbd}} = \left(\frac{\delta_a}{\delta_c'}\right)\frac{151.92s(s + 78)}{(s + 10)\left[s^2 + 2(1)5.9s + 5.9^2\right]} = H(s)\ \frac{\text{deg}}{g} \tag{5}$$

A Nyquist plot of the open-loop transfer function $G(i\omega)\ H(i\omega)$ (where $H(i\omega)$ is defined by eq. (5) for $s = i\omega$ and $G(i\omega)$ is the wing transfer function indicated in fig. 4) at $M = 0.9$ and $q = 7.72$ kPa is presented in figure 6. Gain margins (defined as $-20 \times \log_{10} |G(i\omega)\ H(i\omega)|_{@\phi=-180^{\circ}}$) of -6.4 dB and 5.7 dB and phase margins of -50° and 27° are indicated in figure 6. Control-surface activity as a function of Mach number and dynamic pressure is presented in figure 7. Control-surface deflection is below the 6° rms design goal. The dynamic-pressure root locus at $M = 0.9$ is presented in figure 8. With the control law defined by equation (5), the flutter mode is well damped through q_{max}. A comparison of these results with those of appendix B (where $H(s)$ is defined by eq. (4)) shows that the $s/(s + 10)$ filter has little effect on the predicted performance of the system.

Synthesis Using Optimal Control-Theory Method

The method used to synthesize the optimal control law is described in reference 9. For purposes of completeness, the steps used to derive this control law are given. The method can be divided into two parts: (1) Synthesis of a full-state feedback control law using optimal regulator theory; and (2) synthesis of a practical (acceleration) feedback control law using the results of (1).

Full-state feedback control-law design process.- Optimal regulator theory provides for the minimization of a quadratic cost function of the output and control variables (ref. 13)

$$J = \int_0^{\infty} \left[\{Y\}^T[Q]\{Y\} + \{u\}^T[R]\{u\}\right]dt \tag{6}$$

This minimization results in an optimal full-state feedback control law. The procedure can be summarized as follows:

Step 1: Define the output and control variables that relate to the performance goals (e.g., minimum control-surface displacement).

Step 2: Select initial weighting matrices ($\lceil Q \rceil$ and $\lceil R \rceil$) in the cost function.

Step 3: Solve for the optimal gains, thus minimizing the quadratic cost function.

Step 4: Evaluate the design and, if necessary, adjust the weighting matrices until performance goals are met.

Practical control-law design process.- The design process involves finding the coefficients of a transfer function $H(s)$ that minimizes the deviation of the open-loop frequency response $\frac{\hat{u}}{u}(i\omega)$ from the full-state open-loop frequency response $\frac{\bar{u}}{u}(i\omega)$. Figure 9 shows block diagrams of the full-state feedback and practical systems. If the deviation away from the full-state feedback system is small, the performance of the practical control law will be similar to that of the full-state feedback control law.

The form of the transfer function $H(s)$ to be used is

$$H(s) = K_f \frac{\prod_{i=1}^{m} (s^2 + 2\zeta_i \omega_{ni} s + \omega_{ni}^2)}{\prod_{j=1}^{n} (s^2 + 2\zeta_j \omega_{nj} s + \omega_{nj}^2)} f(s) \tag{7}$$

The design variables are the gain K_f, damping ratios ζ, and natural frequencies ω_n. The function $f(s)$ is included to help achieve any desired characteristics of the filter such as high-frequency rolloff.

An error function can be defined as the difference between $\frac{\hat{u}}{u}(i\omega)$ and $\frac{\bar{u}}{u}(i\omega)$ over a set of frequency points for which a close fit is desired. An optimization algorithm can then be used to find the design variables K_f, ζ, and ω_n that minimize the error function. The procedure can be outlined as follows:

Step 1: Compute the open-loop frequency response $\bar{u}/u$.

Step 2: Compute the frequency response between the output $\ddot{h}$ and the control u.

Step 3: Choose the initial number of numerator factors m and denominator factors n of the filter.

Step 4: Choose an $f(s)$ to incorporate any desired characteristics of the filter such as high-frequency rolloff.

Step 5: Minimize the error function by using an optimization algorithm such as that of Davidon and Fletcher and Powell (refs. 14 and 15, respectively).

Step 6: Examine the open-loop frequency response $\frac{\hat{u}}{u}(i\omega)$ to establish any possible changes to $f(s)$.

Step 7: If any changes to $f(s)$ are established, repeat step 5.

Step 8: Repeat steps 3 to 7 for a family of m and n.

Step 9: Select the m, n, and $f(s)$ that provide the smallest value of the error function.

Step 10: Evaluate the design for a range of Mach numbers and dynamic pressures.

By applying this methodology, the following transfer function was synthesized for the wind-tunnel-model control law:

$$\frac{\delta_a}{\ddot{h}_{outbd}} = \left(\frac{\delta_a}{\delta_c'}\right)\left(\frac{2214}{s}\right)\frac{\left[s^2 + 2(0.127)(121.21)s + 121.21^2\right]}{\left[s^2 + 2(0.962)(297.62)s + 297.62^2\right]}$$

$$\times \frac{\left[s^2 + 2(0.088)269.14s + 269.14^2\right]}{\left[s^2 + 2(0.964)294.91s + 294.91^2\right]}\frac{\text{deg}}{g} \tag{8}$$

Numerical results are presented in appendix C. As shown in this appendix, the control law meets all the design requirements except the -6-dB gain margin at $M = 0.6$. Before the control law was implemented, the direct-current drift, which was referred to previously, in the accelerometer output had to be accounted for. This problem is particularly critical in the present control law because of the infinite static gain associated with a pure integrator of the form $1/s$. In order to alleviate this problem, the term $1/s$ was replaced by $1/(s + 10)$, and an arbitrary washout filter of the form $s/(s + 1)$ was added to drive the static gain to zero. These changes add only a small amount

of phase lag (-10°) in the flutter frequency range. The resulting control law is

$$\frac{\delta_a}{\ddot{h}_{outbd}} = \left(\frac{\delta_a}{\delta_c'}\right)\left(\frac{2214}{s + 10}\right)\left(\frac{s}{s + 1}\right)\frac{\left[s^2 + 2(0.127)(121.21)s + 121.21^2\right]}{\left[s^2 + 2(0.962)(297.62)s + 297.62^2\right]}$$

$$\times \frac{\left[s^2 + 2(0.088)(269.14)s + 269.14^2\right]}{\left[s^2 + 2(0.964)(294.91)s + 294.91^2\right]} = H(s)\ \frac{\text{deg}}{g} \qquad (9)$$

A Nyquist plot of the open-loop transfer function $G(i\omega)\ H(i\omega)$ (where $H(i\omega)$ is defined by eq. (9)) at $M = 0.9$ and $q = 7.24$ kPa is presented in figure 10. Control-surface activity as a function of Mach number and dynamic pressure is presented in figure 11. The closed-loop root locus is presented in figure 12. A comparison of these results with those of appendix C (where $H(s)$ is defined by eq. (8)), shows that the filter addition has little effect on either the Nyquist diagram or the control-surface activity.

WIND-TUNNEL TESTS

Wind Tunnel

All experimental studies were conducted in the Langley Transonic Dynamics Tunnel. The tunnel is a closed-circuit continuous-flow facility with a 4.88-m square test section. It operates at stagnation pressures from near vacuum to slightly above atmospheric and at Mach numbers from near 0 to 1.2. Mach number and dynamic pressure can be varied simultaneously, or independently, with either air or freon as a test medium. Freon was used for all tests in this study.

Control-Law Mechanization

A simplified block diagram of the flutter-suppression system was previously presented in figure 4. A detailed description of the flutter-suppression-system mechanization is presented in appendix D. Both control laws were programmed on an analog computer located in the tunnel control room. The analog computer processed the accelerometer output signal from the wing, and the control law being used determined the appropriate actuator command signal. The command signal was then passed to the servo-actuator system which controlled the position of the control surface. For the flutter-suppression system-off tests, the control surface was kept at 0° deflection by applying hydraulic pressure to the actuator.

Test Techniques and Procedures

In evaluation of a flutter-suppression system, it is necessary to measure damping of the flutter mode. Most techniques used to measure damping involve exciting the model with a known input through the control surface and measuring the transient response. Previous tests of the model indicated a difficulty in measuring a reliable flutter mode damping through control-surface excitation because of relatively large amounts of wing acceleration caused by tunnel turbulence. Therefore no attempt was made to measure damping during these tests. However the Peak-Hold Spectrum method described in reference 4 was used during online tests to evaluate the performance of the systems. Instead of damping, this method uses the inverse of the model response to turbulence as a stability criterion.

For most of these tests, Mach number was held constant while dynamic pressure was increased by continuously bleeding freon into the tunnel. Data were gathered and analyzed at points where both dynamic pressure and Mach number were held constant. The primary data acquired during the tunnel tests included rms control-surface deflection, time-response strip chart recordings of control-surface deflection, and peak acceleration response of the wing at discrete test points obtained by using a spectrum analyzer. All instrumentation signals (including strain gauges, accelerometers, and control-surface position sensor) were recorded on magnetic tape.

Wing without flutter-suppression (system-off) tests were performed to establish the basic-wing flutter boundary. These tests were followed by closed-loop (system-on) tests of both control systems to evaluate their effect on raising the flutter dynamic pressure.

RESULTS AND DISCUSSION

Experimental flutter studies of the model were conducted at Mach numbers of 0.6, 0.8, 0.9, and 0.95. During the closed-loop testing, unexpectedly large control-surface deflections of a random nature were encountered above the system-off flutter boundary. Because of these peak deflections (which at times approached the $\pm 14^{\circ}$ limit as dynamic pressure was increased), the test objectives of demonstrating a 44-percent increase in flutter dynamic pressure from $M = 0.6$ to $M = 0.9$ could not be met. However, tests were added at $M = 0.95$ that were successful in demonstrating the 44-percent increase for both control laws.

Wing Without Flutter Suppression

Experimental results.- The system-off flutter characteristics are presented in figure 13 in terms of the variation of flutter dynamic pressure and flutter frequency with Mach number. These experimental results repeated those measured at $M = 0.6$ and $M = 0.8$ in the earlier study of reference 11. Results from the present test at $M = 0.9$ indicate about a 9-percent decrease in flutter dynamic pressure from the earlier results. This decrease is believed to be attributable to slight differences in the mass distribution of

the model between the two tests. (During the previous tests the model was equipped with a leading-edge control-surface actuator combination. Prior to the present studies the actuator was replaced with a rigid connection which resulted in some slight mass differences.)

Comparison of analytical and experimental results.- The dynamic pressure root locus plot at $M = 0.9$ for the system off is presented in figure 14. Calculations were also performed at $M = 0.6$, 0.7, 0.8, and 0.95 to establish the calculated flutter boundary shown in figure 13. The agreement between calculations and experiment is good across the Mach number range.

Wing With Flutter Suppression

A summary of the maximum dynamic pressures to which the model was tested (above that for the wing without flutter suppression) is presented in figure 15. The test objective of demonstrating a 44-percent increase in flutter dynamic pressure from $M = 0.6$ to $M = 0.9$ was not achieved. However, at $M = 0.95$, both control laws demonstrated a 44-percent increase in flutter dynamic pressure. At $M = 0.9$, increases in dynamic pressure of 35 percent and 27 percent were demonstrated by the optimal control law and the energy control law, respectively, before control-surface saturation occurred. At saturation, the control surface was forced against its mechanical stop, thus resulting in a system-off flutter instability. At $M = 0.6$ and 0.8, both control laws demonstrated increases in dynamic pressure, but these tests were terminated when it became obvious that the 44-percent increase could not be achieved.

The performance of the flutter-suppression systems is illustrated by the oscillograph records of the outboard wing accelerometer and the control-surface position presented in figure 16. (The records shown are for the aerodynamic energy control law, but similar results were also obtained for the optimal control law.) The test condition was a dynamic pressure 10 percent above the system-off flutter point at $M = 0.9$. Time is increasing from left to right in the figure. The trace starts with the flutter-suppression system turned on. The system was turned off for approximately 4.5 sec and then turned on again. During the time the control system was turned off, the wing began to flutter as evidenced by the rapid buildup of acceleration amplitude. The effect of turning the system back on was a rapid suppression of the oscillatory motion.

Another illustration of the performance of the control systems is presented in figure 17. Presented in the figure is the peak output acceleration plotted against frequency obtained from the spectrum analyzer for the wing without flutter suppression and for each of the two control laws turned on. These data were measured at a dynamic pressure just below the system-off flutter dynamic pressure at $M = 0.9$. A decrease in amplitude and an upward shift in frequency of the maximum response resulting from operation of the flutter-suppression systems are illustrated.

Aerodynamic energy method results.- The first series of closed-loop tests were performed at $M = 0.9$. During this first series of tests, it became evident from measurements of the actuator hydraulic pressure that the control

surface was approaching the rate limit of the actuator (rate saturation) because of the response in the 40- to 50-Hz range. Analysis results (fig. 7) did not predict rates in the range of saturation (820 deg/sec) for the control law. Refer to figure 3 and note that the inboard accelerometer is located in an area of significant modal response for the fourth and fifth flexible modes. In lieu of adding electronic filters to reduce this response, the feedback sensor was shifted from the inboard to the outboard accelerometer. The outboard accelerometer is located very near the node lines for these modes. Since this method was developed for a two-dimensional wing, it is not surprising that small variations in the accelerometer location may be required. No attempts were made to adjust the overall gain of the flutter-suppression system even though the modal displacement in the first flexible mode is approximately 20 percent greater at the outboard accelerometer location.

An alternate aerodynamic energy control law was therefore implemented on the model by simply replacing $\ddot{h}_{inbd}$ by $\ddot{h}_{outbd}$ in equation (5). A Nyquist plot of the open-loop transfer function (based on $\ddot{h}_{outbd}$) at $M = 0.9$ and $q = q_{max}$ is presented in figure 18. By comparing these results with those in figure 6, a significant change in the positive gain margin is apparent. The Nyquist plot indicated that the positive gain margin could have been significantly improved by simply reducing the overall gain of the control law to reflect the increased amplitude of the first mode at the outboard accelerometer location. Control-surface activity for the alternate control law as a function of dynamic pressure at various Mach numbers is presented in figure 19. A comparison of these results with those in figure 7 shows only slight increases in control-surface activity. A root locus plot ($M = 0.9$) using the alternate aerodynamic energy control law is presented in figure 20. Comparing root loci between the two aerodynamic energy control laws (figs. 8 and 20) shows that the roots of the first flexible mode are not significantly changed. The roots of the second and fourth flexible modes couple in the alternate control law to produce an instability. However the instability occurs above q_{max}. During wind-tunnel tests of the alternate energy control law the rate saturation problem did not reoccur.

Experimental results were obtained for both accelerometer locations at $M = 0.6$, 0.8, and 0.9. At $M = 0.95$, only the outboard accelerometer was used. Figure 21 presents the control-surface rms deflection and the frequency of the flutter mode from the spectrum analyzer at $M = 0.6$, 0.8, 0.9, and 0.95. For comparison purposes analytical results are also presented. At $M = 0.6$, the measured rms displacement is well below the calculated data. At the other Mach numbers the rms deflections compare more favorably with analysis. Frequency of the flutter mode compares reasonably well with predicted results across the Mach number range. Predicted values of flutter dynamic pressure, flutter frequency, and control-surface response at q_{max} for the aerodynamic energy control laws are given in table II.

Optimal control-theory method results.- At $M = 0.9$, a 35-percent increase in flutter dynamic pressure (see fig. 15) was demonstrated before excessive control-surface deflection saturated the system, thereby resulting in system-off flutter. At $M = 0.6$ and 0.8, the tests were terminated after small increases were achieved in dynamic pressure because of peak control-surface deflections. At $M = 0.95$, the desired 44-percent increase in flutter dynamic

pressure was demonstrated. At this condition peak control-surface deflections were in the range of 9^{o}.

Figure 22 presents the rms control deflection and the frequency of the flutter mode from the spectrum analyzer at M = 0.6, 0.8, 0.9, and 0.95. For comparison purposes analytical results are also presented. In general, the measured rms deflection is well below that of the analytical data. Frequency of the flutter mode compares favorably with the analytical data across the Mach number range. Predicted values of flutter dynamic pressure, flutter frequency, and control-surface response at q_{max} for the optimal control theory control law are given in table II.

Problem Areas

The major problem that occurred during the wind-tunnel tests was excessive control-surface peak deflections. Even though the rms control deflection was below that predicted by analysis (see figs. 21 and 22), the peak deflections were beyond the capability of the actuator. The ratios of measured peak to average rms control deflections at M = 0.9 and M = 0.95 as a function of dynamic pressure are presented in figure 23. Also presented are unpublished data acquired during the wind-tunnel study reported in reference 11. Based on the previous study, it was assumed that at the higher dynamic pressures the maximum ratio of peak to rms control deflection would be in the range of 3. Since the maximum rms control deflection was predicted to be less than 4^{o} at M = 0.9, the resulting peak deflections would be well within the actuator limits. At M = 0.9 for the optimal control law, ratios of measured peak to rms control deflection ranged from a minimum of 3.3 at the lower dynamic pressures to a maximum of 4.7 at the higher dynamic pressures. At this Mach number the 44-percent goal could not be achieved because of control-surface saturation. At M = 0.95 for the optimal control law, this ratio varies from a minimum of 1.6 to a maximum of 2.1 and the goal of a 44-percent increase in dynamic pressure was achieved.

Control-surface deflection is a function of dynamic pressure, the intensity and frequency distribution of the turbulence in the wind tunnel, and the effectiveness of the flutter-suppression system. It was impossible during the wind-tunnel tests to separate these effects quantitatively. As mentioned previously, an adequate model of wind-tunnel turbulence is not available. In addition, the response of the wing to tunnel turbulence (both system on and off) was so large that subcritical measurements aimed at evaluating the flutter mode damping could not be performed. However, some qualitative data are available which indicate areas of concern.

During the tests the relative stability of the wing was evaluated by using the Peak-Hold Spectrum method, as described in reference 4. As stated previously, instead of damping, this method uses the inverse of the model response to turbulence as a measure of relative stability. For the flutter mode the inverse amplitude obtained from a Peak-Hold Spectrum is plotted against dynamic pressure. At flutter the inverse amplitude goes to zero. These data can be used to establish a damping trend which can then be extrapolated to predict the flutter dynamic pressure. Measurements of the inverse amplitude of the flutter

mode at $M = 0.9$ as a function of dynamic pressure are presented in figure 24 (the inverse amplitude is normalized by dynamic pressure in an effort to separate the forced response due to dynamic-pressure changes from those due to damping changes). Results are presented for the flutter-suppression system turned off and on (optimal control law). A curve drawn through the system-off points (circular symbols) indicates that the flutter point can be reasonably extrapolated from the subcritical data. Extrapolating the system-on points (square symbols) indicates that flutter would occur between the measured saturation point ($q = 6.64$ kPa) and the predicted flutter point ($q = 9.03$ kPa).

The impact of these results becomes more apparent when predicted values of flutter mode damping are considered. The predicted flutter mode damping for the system off, the aerodynamic energy control law, the optimal control law, and the control law published in reference 11 are presented in figure 25. Between 5 and 7 kPa the level of damping for all three control laws is substantially larger than the maximum value of damping for the system off. By assuming that the parameter on the ordinate in figure 24 is proportional to damping, the level of damping indicated by the system-on curve is of the same order as that for the system-off data. (For example, at $q = 6.5$ kPa, the system-on damping is the same as the system-off damping at $q = 3.8$ kPa.) This level of damping is not indicated by the analysis. Therefore, it can be assumed that the control systems are not so effective in generating damping in the flutter mode as predicted. In general, control-surface aerodynamic hinge moments are overpredicted by unsteady theory when compared to experimental data and could account for the differences between theory and experiment.

Wind-tunnel turbulence compounds the problem of excessive control-surface deflections. As shown in reference 16, the magnitude of unsteady pressure fluctuations in the Langley Transonic Dynamics Tunnel peaks between $M = 0.85$ and $M = 0.9$ and then decreases rapidly as Mach number is increased. During most of the wind-tunnel tests Mach number was held constant while dynamic pressure was increased by bleeding in freon. The last run at $M = 0.95$ was performed by varying dynamic pressure and Mach number simultaneously along a line of constant tunnel pressure. During this run a significant reduction in the control-surface response occurred above $M = 0.93$. At $M = 0.95$, peak deflections of the control surface were in the range of 6° even though the dynamic pressure was only 6 percent less than the maximum dynamic pressure at $M = 0.9$. At $M = 0.9$, control-surface deflections were greater than 14°, thereby resulting in saturation. This problem indicates a pressing need for a satisfactory definition of wind-tunnel turbulence.

To date three control laws have been experimentally tested on the model. These include the two control laws described in this paper and the control law presented in reference 11. At $M = 0.9$ increases in flutter dynamic pressure, prior to control-surface saturation, have varied from 42 percent (ref. 11) to 35 percent for the optimal control law and to 27 percent for the aerodynamic energy control law. Predicted values of rms control-surface deflection are in the opposite order; that is, the aerodynamic energy control law requires the least deflection, followed by the optimal control law, and finally the control law from reference 11. Refer to figure 25 and note that the predicted level of flutter mode damping varies in the same order as the dynamic pressure for which each control law is saturated. It appears that a minimum level of flutter mode

damping (which is sufficient for stability) is required to overcome the forced response of the model because of turbulence.

CONCLUSIONS

Two methods for designing active flutter-suppression control laws, the aerodynamic energy method and the optimal control theory, have been presented. These methods were applied to an aeroelastic wind-tunnel model equipped with a hydraulically actuated trailing-edge control surface. The resulting systems were tested in the Langley Transonic Dynamics Tunnel. Some important conclusions of this study are:

1. The application of both the aerodynamic energy method and the optimal control theory resulted in control laws that were effective in suppressing flutter. At Mach 0.6, 0.8, and 0.9, modest increases in the flutter dynamic pressure were measured. At Mach 0.95, both control laws demonstrated 44-percent increases in flutter dynamic pressure.

2. Calculations with the synthesized control laws indicated larger values of flutter mode damping than the test data showed. Additional work is required to account for the uncertainties in the unsteady aerodynamics of oscillating control surfaces.

3. A Von Kármán gust spectrum does not appear to represent accurately the wind-tunnel turbulence model. Additional work is needed to define accurately the tunnel turbulence model and its application to the prediction of control-surface activity because it is a major factor in the design and evaluation of system performance.

Langley Research Center
National Aeronautics and Space Administration
Hampton, VA 23665
March 12, 1980

APPENDIX A

AEROELASTIC ANALYSIS

A description of the analysis used to calculate the flutter characteristics, both with and without active controls, is given in this appendix. Also given is a description of the gust-response analysis used to calculate control-surface deflection and rate.

The equations of motion for a flexible vehicle may be expressed in matrix form as

$$\left([M]s^2 + [2\zeta M\omega_n]s + [K] + \frac{1}{2}\rho V^2[\hat{Q}]\right)\{q\} = -\frac{1}{2}\rho V\{\hat{Q}_G\}w_g \tag{A1}$$

where $[M]$ represents the generalized mass matrix; $[2\zeta M\omega_n]$, the structural damping matrix; $[K]$, the generalized stiffness matrix; $[\hat{Q}]$, the complex aerodynamic matrix due to motion; $\{\hat{Q}_G\}$, the complex aerodynamic vector due to gust disturbance; and $\{q\}$, the response vector. All the matrices in equation (A1) are of the size $n \times (n + r)$, where n is the number of structural modes and r is the number of active control surfaces. By expressing the response vector as

$$\{q\} = \begin{Bmatrix} q_s \\ q_c \end{Bmatrix} \tag{A2}$$

equation (A1) can be written as

$$\left([M_s \vdots M_c]s^2 + [2\zeta M\omega_n \vdots 0]s + [K_s \vdots K_c] + \frac{1}{2}\rho V^2[\hat{Q}_s \vdots \hat{Q}_c]\right)\begin{Bmatrix} q_s \\ q_c \end{Bmatrix} = -\frac{1}{2}\rho V\{\hat{Q}_G\}w_g \tag{A3}$$

where the subscript s denotes a structural quantity and c, a control quantity. The equation that relates control-surface motion to wing response (control law) can be expressed as

$$\{q_c\} = [T][\phi]\{q_s\} \tag{A4}$$

where $[T]$ is the transfer function matrix and $[\phi]$ is the matrix of modal displacements at the sensor location. Typically, $[T]$ is expressed as a rational polynomial in s by letting

$$[T] = \frac{[T_N]}{Q(s)}$$

where $Q(s)$ is a scalar polynomial representing the common denominator of all the elements of $[T]$, and $[T_N]$ is a matrix of the resulting numerators. Equation (A4) can now be expressed as

$$\{q_c\} = \frac{[T_N][\phi]}{Q(s)} \{q_s\} \tag{A5}$$

Typically, the elements of the aerodynamic matrices $\hat{Q}_s$, $\hat{Q}_c$, and $\hat{Q}_G$ are available as tabular functions of reduced frequency k, whereas the control law is expressed in terms of a rational polynomial in the Laplace variable s. The variation of the aerodynamic matrices with s can be approximated by the representation

$$[\hat{Q}] = [A_0] + [A_1]\left(\frac{b}{V}\right)s + [A_2]\left(\frac{b}{V}\right)^2 s^2 + \sum_{m=3}^{6} \frac{[A_m]s}{s + \frac{V}{b}\beta_{m-2}} \tag{A6}$$

where $[\hat{Q}]$ is $\hat{Q}_s$, $\hat{Q}_c$, and $\hat{Q}_G$ and all of the matrix coefficients and β-values are real. Substitution of equations (A5) and (A6) into equation (A3) and multiplication by $Q(s)$ yields a matrix polynomial expression in s of the form

$$([F_0] + [F_1]s + [F_2]s^2 + \ldots [F_m]s^m)\{q_s\} = (\{G_0\} + \{G_1\}s + \ldots \{G_m\}s^m)w_g \tag{A7}$$

where the matrix coefficients $[F_j]$ and $\{G_j\}$ are functions of Mach number, velocity, and dynamic pressure. For flutter analyses only the homogeneous part of equation (A7) is solved; that is

$$([F_0] + [F_1]s + [F_2]s^2 + \ldots [F_m]s^m)\{q_s\} = 0 \tag{A8}$$

APPENDIX A

By using the relationship

$$\{X\} = \begin{Bmatrix} s^{m-1} & \{q_s\} \\ s^{m-2} & \{q_s\} \\ \cdot & \cdot \\ \cdot & \cdot \\ \cdot & \cdot \\ s^0 & \{q_s\} \end{Bmatrix}$$

equation (A8) can be reduced to a set of first-order equations of the form

$$s\{X\} = [A]\{X\} \tag{A9}$$

The eigenvalues of equation (A9) are the roots of the characteristic flutter equation. Root loci can be constructed to correspond to the variation in the eigenvalues of the system described by equation (A9) as a function of dynamic pressure.

Gust-response analyses are performed by using power-spectral-density (PSD) techniques similar to those described in reference 11. The modal response of the system per unit gust velocity can be determined by solving equation (A7) at discrete values of $s(s = i\omega)$; that is

$$\frac{\{q_s(i\omega)\}}{w_g} = \left[\left([F_0] + [F_1]s + [F_2]s^2 + \ldots [F_n]s^n\right)\{q_s\}\right]^{-1} \times \left[\left(\{G_0\} + \{G_1\}s + \ldots \{G_n\}s^n\right)w_g\right]$$

The control-surface response can then be evaluated by

$$\frac{\{q_c(i\omega)\}}{w_g} = \frac{[T_N][\phi]}{Q(i\omega)} \frac{\{q_s(i\omega)\}}{w_g} \tag{A10}$$

The PSD functions of control-surface response are determined by

$$\phi_o(\omega) = \phi_I(\omega)\left|H_\delta(i\omega)\right|^2$$

where $H_\delta(i\omega)$ = Element of control-surface frequency-response vector $\left\{\frac{q_c(i\omega)}{w_g}\right\}$ (eq. (A10)) and $\phi_I(\omega)$ = Input gust spectrum defined by

$$\frac{\sigma w_g^2 L\left[1 + \frac{8}{3}(1.339L\omega/V)^2\right]}{\pi V[1 + (1.339L\omega/V)^2]^{11/6}}$$

where $\sigma w_g = 1.0$. The rms value of the control-surface response per unit rms gust velocity σw_g is defined by

$$\left(\frac{\delta_a}{\sigma w_g}\right)_{rms} = \left(\frac{q_c}{\sigma w_g}\right)_{rms} = \left(\int_0^\infty \phi_o(\omega)\ d\omega\right)^{1/2} \qquad (A11)$$

APPENDIX B

NUMERICAL RESULTS OBTAINED BY USING AERODYNAMIC ENERGY METHOD

The numerical results obtained from applying the aerodynamic energy method are presented in this appendix. The format of the appendix parallels the design steps described in the text. Analytical methods used to perform the design steps are described in the following references:

(a) Optimization (ref. 8)

(b) Nyquist criterion (ref. 17)

(c) Stability and gust response (ref. 11)

The design steps are as follows:

Step 1 - Initialization of free parameters: The boundary corresponding to a 44-percent increase in flutter dynamic pressure is indicated by the dashed-line curve in figure 5. Based on previous experience and guidelines presented in reference 8, the following values were assigned the free parameters in equation (3)

$\omega_1 = 35$ $\omega_2 = 75$

$\zeta_1 = 0.99$ $\zeta_2 = 0.99$

$a_1 = 2.0$ $a_2 = 2.0$

The resulting system is stable above the boundary defined by q_{max}.

Step 2 - Minimum control-surface activity: The design point selected for the optimization was $M = 0.9$; $q = 7.72$ kPa. During the optimization, the free parameters were constrained as follows:

$0 \leqq (\omega_1, \omega_2) \leqq 75$

$0.5 \leqq (\zeta_1, \zeta_2) \leqq 1.0$

$0 \leqq (a_1, a_2) \leqq 2.0$

The following results were obtained when the system was optimized for minimum control-surface deflection at the design point:

APPENDIX B

$a_1 = 0.984$ $\quad a_2 = 0$

$\zeta_1 = 1.0$ $\quad \zeta_2 = 1.0$

$\omega_1 = 5.9$ $\quad \omega_2 = 75.0$

resulting in

$$\delta_c'(s) = \left[\frac{0.984s^2}{s^2 + 2(1.0)5.9s + 5.9^2}\right]\frac{4h_{inbd}}{b_r} \text{ rad} \qquad \text{(B1)}$$

Control-surface rates and displacements at the design point are

$\dot{\delta}_{a,rms} = 189.2$ deg/sec

$\delta_{a,rms} = 3.62^o$

Step 3 - Control-surface activity over a range of tunnel conditions: By using equation (B1), control-surface rates and deflections were calculated at $M = 0.6$, 0.7, 0.8, and 0.9 as a function of dynamic pressure. These results are presented in figure 26. Maximum control-surface rate and displacement occur at $M = 0.6$; $q_{max} = 10.62$ kPa and are 260 deg/sec and 4.9^o, respectively. Control-surface activity below q_{max} is well within the goals set for the design.

Step 4 - Addition of actuator transfer function: A block diagram of the flutter-suppression system is illustrated in the following sketch:

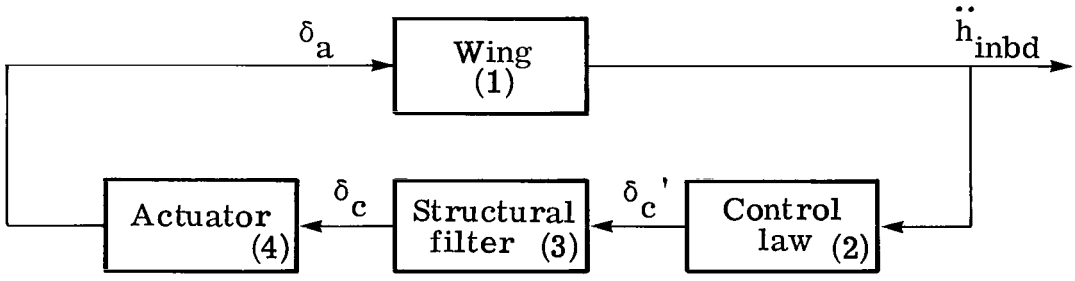

Sketch A

APPENDIX B

The transfer function relating control deflection δ_a to the command δ_c' is (see eq. (1))

$$\frac{\delta_a(s)}{\delta_c'(s)} = \frac{(1.915 \times 10^7)(628.3)^2}{(s + 214)(s^2 + 179.4s + 8.945 \times 10^4)(s + 628.3)^2} \frac{\text{deg}}{\text{deg}}$$

By using equation (B1) and letting $\ddot{h}_{inbd} = s^2 h_{inbd}$, the control-system transfer function is written as

$$\frac{\delta_a}{\ddot{h}_{inbd}} = \left(\frac{\delta_a}{\delta_c}\right)\left(\frac{\delta_c}{\delta_c'}\right)\left(\frac{\delta_c'}{\ddot{h}_{0.65c}}\right)$$

or

$$\frac{\delta_a}{\ddot{h}_{0.65c}} = \frac{8.02 \times 10^{16}}{[s^2 + 2(1)5.9s + 5.9^2](s + 628.3)^2(s + 214)(s^2 + 179.4s + 8.945 \times 10^4)} \frac{\text{deg}}{g} \quad \text{(B2)}$$

The stability of the closed-loop system was determined by using a Nyquist analysis (ref. 17). This method was chosen because of the ease in determining gain margins. In order to apply the Nyquist method, the blocks in sketch A are combined in the following manner:

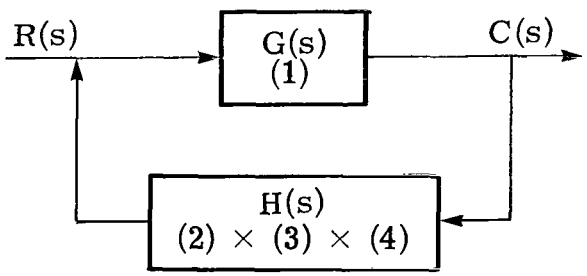

Sketch B

where G(s) is the wing transfer function with respect to control-surface motion (block (1) in sketch A) and H(s) is the transfer function defined by block (2) × block (3) × block (4) (sketch A). The closed-loop transfer function is defined by

$$\frac{C(s)}{R(s)} = \frac{G(s)}{1 + G(s)H(s)}$$

The stability of the closed-loop system is determined by evaluating encirclements of the $-1 + 0i$ point by the locus of the open-loop transfer function $G(i\omega)\,H(i\omega)$ as ω varies from ∞ to $-\infty$.

The locus of $G(i\omega)\,H(i\omega)$ at the design point is presented in figure 27. (Since $G(i\omega)\,H(i\omega)$ and $G(-i\omega)\,H(-i\omega)$ are symmetrical with respect to the real axis, only the results for positive frequencies are presented.) Arrows indicate increasing frequency. The dashed-line curve represents a unit circle, the center of which is at the origin of the complex plane. Since there are no net clockwise encirclements of the $-1 + 0i$ point, the closed-loop system is unstable at the design point for the control system defined by equation (B2). The frequency of the instability is approximately 84 rps.

Step 5 - Compensator design: In order to account for phase lags introduced by equation (1), a simple lead filter of the form $s + \omega_a$ was introduced into equation (B2). The value of ω_a was fixed by determining the amount of phase lead required to compensate for the phase lag introduced by equation (1) at the instability frequency of 84 rps; that is,

Denominator terms	Phase lag @ω = 84
$(s + 628.3)^2$	15.2°
$(s + 214)$	21.4°
$(s^2 + 179.4s + 8.945 \times 10^4)$	10.4°
	47.0° total lag

The value of ω_a, to compensate for the 47° phase lag, is 78 rps. When $s + 78$ was added to equation (B2), the overall gain was adjusted so that the static gain ($\omega = 0$) from equation (B2) was retained. This results in the control-system transfer function

$$\frac{\delta_a}{\ddot{h}_{0.65c}} = \frac{1.03 \times 10^{15}(s + 78)}{\left[s^2 + 2(1)5.9s + 5.9^2\right](s + 628.3)^2(s + 214)(s^2 + 179.4s + 8.945 \times 10^4)} \frac{\text{deg}}{g} \qquad \text{(B3)}$$

Nyquist plots of the open-loop transfer function $G(i\omega)\,H(i\omega)$ (with $H(s)$ defined by eq. (B3)) indicated that the gain margins at q_{max} for all Mach numbers were less than

±6 dB. The static gain was then increased until a minimum gain margin of -6 dB was achieved at q_{max} for all Mach numbers. The resulting control-system transfer function is

$$\frac{\delta_a}{\ddot{h}_{inbd}} = \left(\frac{\delta_a}{\delta_{c'}}\right)\left[\frac{147.35(s + 78)}{s^2 + 2(1)5.9s + 5.9^2}\right]\frac{deg}{g} \qquad (B4)$$

The Nyquist plot, with H(s) defined by equation (B4), at q_{max} for M = 0.9 is presented in figure 28. At M = 0.6 and 0.7, the ±6-dB gain margin requirement is met. At M = 0.9 and 0.8, gain margins are slightly less than 6 dB. Reducing the static gain at M = 0.9 and 0.8 would allow the ±6-dB gain margin to be achieved but would also require gain scheduling to achieve the -6-dB gain margin at the lower Mach numbers. Since gain-margin goals are somewhat arbitrary, the control-system transfer function defined by equation (B4) was judged to be acceptable in meeting the gain-margin design goals.

Step 6 - Control-surface activity with actuator and compensator: By using equation (B4), control-surface rates and deflections were calculated at four Mach numbers as a function of dynamic pressure. These results are presented in figure 29. At the design point (M = 0.9; q_{max} = 7.72 kPa), control-surface rate and displacement are

$$\dot{\delta}_{a,rms} = 181 \text{ deg/sec}$$

and

$$\delta_{a,rms} = 3.62^{o}$$

Compare these results with those of step 3, and note that the response of the control surface at the design point has not been adversely affected. Compare the results of figure 29 with those of figure 26, and note that the maximum rates at the higher dynamic pressures are reduced, the rates at the lower dynamic pressures are increased, and the deflections remain relatively unchanged. Control-surface rates and displacements are given in table II.

Step 7 - Closed-loop dynamic-pressure root loci: Flutter calculations were performed across the Mach number range by using the transfer function defined by equation (B4). At M = 0.9 and M = 0.8, the flutter dynamic pressures are well above the boundary defined by q_{max} (fig. 5). At M = 0.6 and 0.7, no flutter is predicted up to a maximum dynamic pressure of 12.2 kPa. Figure 30 presents

a typical dynamic-pressure root locus at M = 0.9. A comparison of these results with those of figure 14 (no flutter suppression) indicates that flutter is delayed by modifying flexible modes 1 and 2. The higher frequency modes are largely unaffected by the flutter-suppression system. Without flutter suppression, flutter is predicted to occur at a dynamic pressure of 5.03 kPa. With flutter suppression, flutter is predicted to occur at a dynamic pressure of 11.2 kPa.

APPENDIX C

NUMERICAL RESULTS OBTAINED BY USING OPTIMAL CONTROL THEORY

The numerical results obtained from applying the optimal control-theory method are presented in this appendix.

Optimal Control-Law Design

For the optimal control-law design, zero-state weighting ($[Q] = 0$) was selected since this yields a set of gains that provide the smallest control-input amplitude (ref. 17). Once the full-state feedback gain matrix was determined, the optimal Nyquist diagram for the single input case was constructed by solving

$$\frac{\bar{u}(i\omega)}{u(i\omega)} = [K^*][i\omega I - \bar{A}]^{-1}\{B\} \tag{C1}$$

The resulting Nyquist diagram (fig. 31) is a counterclockwise circle of radius unity centered on the (-1,0) point. The full-state feedback control law provides gain margins of -6 dB and ∞ and phase margins of $\pm 60^{\circ}$.

Practical Control-Law Design

By using the accelerometer location shown in figure 2, the output frequency response was calculated by

$$\frac{\ddot{h}_{outbd}}{u(i\omega)} = [C_\phi][i\omega I - A]^{-1}\{B\} \tag{C2}$$

where $[C_\phi]$ is a row matrix of mode-shape displacements (table I) at the sensor location. In the frequency plane the feedback filter (eq. (7)) has the form

$$H(i\omega) = K_f \frac{\prod_{i=1}^{m} \left[(i\omega)^2 + 2\zeta_i \omega_{ni}(i\omega) + \omega_{ni}^2\right]}{\prod_{j=1}^{n} \left[(i\omega)^2 + 2\zeta_j \omega_{nj}(i\omega) + \omega_{nj}^2\right]} f(i\omega) \tag{C3}$$

APPENDIX C

Various values of m and n were tried, and the combination that provided the smallest value of the error function ($m = 2$, $n = 2$) was determined. The low-frequency (3 rad/sec to 60 rad/sec) portion of the open-loop frequency response (not shown) indicated the need for an integrator. The error function was again minimized with the previously determined values of m and n and with $1/(i\omega)$ as the polynomial factor $f(i\omega)$ in the filter. The optimization algorithm did not result in a -6-dB gain margin; therefore the gain K_f was increased until a gain margin of -6 dB was achieved, thereby resulting in the control law

$$\frac{\delta_c'}{\ddot{h}_{outbd}} = \frac{2214}{s}\left[\frac{s^2 + 2(0.127)(121.21)s + 121.21^2}{s^2 + 2(0.962)(297.62)s + 297.62^2}\right] \times \left[\frac{s^2 + 2(0.088)(269.14)s + 269.14^2}{s^2 + 2(0.964)(294.91)s + 294.91^2}\right]\frac{deg}{g} \tag{C4}$$

Calculations were performed across the Mach number range by using the control law defined by equation (C4). All across the Mach number range, the flutter dynamic pressures are above the 44-percent-increase requirement. Figure 32 presents the dynamic-pressure root locus at $M = 0.9$. A comparison of these results with those of figure 14 (no flutter suppression) indicates that the control law increases the damping of the flutter mode while having very little effect on the other modes. Control-surface deflections and rates are presented in figure 33 for all four Mach numbers as a function of dynamic pressure. The largest values of $\delta_{a,rms}$ (5.5°) and $\dot{\delta}_{a,rms}$ (270 deg/sec) occur at the largest value of dynamic pressure investigated ($M = 0.6$; $q = 10.77$ kPa). Open-loop frequency responses (Nyquist diagrams) with $H(s)$ defined by equation (C4) were calculated to establish gain and phase margins. Figure 34 shows the Nyquist diagram at the design condition. The gain margins are -6.27 dB and 13.60 dB with phase margins of -59° and 41°. The Nyquist diagrams at the other Mach numbers (not shown) are similar in character to that at $M = 0.9$.

APPENDIX D

CONTROL-SYSTEM MECHANIZATION

A brief description of the design and operation of the actuator loops and control-law feedback loops is given in this appendix. The flutter-suppression control system (fig. 4) consists of the trailing-edge actuator loop, the optimal control law or the energy control-law loop and a structural filter. The actuator loop is an electrohydraulic position feedback system contained in a hard wired unit that could not be modified during the test. The control laws were programmed on the analog computer and could be modified as necessary to adjust the performance of the control system. A second-order low-pass filter was included to avoid a previously encountered high-frequency wing structural hydraulic-fluid instability.

Actuator Loop

Figure 35 is a block diagram of the actuator loop. The actuator loop must be capable of displacing the control surfaces in the exact manner dictated by the control law over the operating frequency range of the system. The actuator performance can be described as follows:

(1) The bandwidth of the actuator loop must be sufficiently greater than the closed-loop operating frequency of the control system but small enough to avoid high-frequency instabilities.

(2) The actuators must have sufficient amplitude and rate capability.

(3) The actuators must provide sufficient torque to drive the control surface under all operating conditions.

(4) The hysteresis of the actuator must be small enough so that the performance is not degraded. In this case, 0.1° was considered adequate.

The operation of the loop, as shown in figure 35, can be described in the following manner. A trailing-edge command voltage δ_c is compared to the trailing-edge position δ_a; the error is amplified by the forward-loop gain K_v. The servovalve amplifier converts this signal into the servovalve current I_v, which controls the flow Q of the hydraulic fluid into the actuator. The integral of this flow rate is proportional to the change in the position of the trailing edge. The surface will continue to move until the error between the surface and the command is zero. Because of the deadband inherent in the construction of the servovalve, the actuator response will have a certain degree of hysteresis. The degree of hysteresis is inversely proportional to the static forward-loop gain of the system. Since increasing the forward-loop gain destabilizes the system, the pressure-loop gain K_p is used to obtain the desired transient response of the system, while the forward-loop gain K_v is adjusted to control the hysteresis. This stabilizing gain must have the static component removed with a high-pass filter so that the actuator will not respond to any applied loads that the control surface encounters. The

measured frequency response and hysteresis of the closed-loop system are shown in figures 36 and 37, respectively. The actuator deadband from figure 37 indicates that the hysteresis of the actuator was 0.1°. By characterizing the response shown in figure 36 as a second-order system, it can be shown that the dominant oscillatory mode of approximately 40 Hz has a critical damping ratio of 0.24 and characterizes the motion of the actuator.

Control-Law Feedback Loop

The control-law feedback provides the required compensation from the sensor to the trailing-edge command. The control laws were programmed on an analog computer. The capabilities were as follows:

(1) The program was able to use either accelerometer signal with either control law

(2) Either control law was selected

(3) The control law was able to be switched on or off

The differential equations for the energy control law, the optimal control law, and the structural filter were programmed on the analog computer by the application of Johnson's mechanization method for transfer functions (ref. 18). The analog program that results from using this method is presented in figure 38. The system was scaled so that a sinusoidal acceleration input of 5g at a frequency of 8 Hz would neither exceed a trailing command of 20° nor overload any amplifier in the analog circuit. Refer to figure 38, and note that manual switch 4 is used to choose the sensor to be used in the control law. Switch 0 was used to select the control law to be used. When this relay was in the set position, the energy control law was engaged, and when it was reset, the optimal control law was engaged. Manual switch 3 was used to turn the control command on or off. In the off position, a zero trailing-edge command was sent to the actuator control loop.

REFERENCES

1. Hood, Ray V.: Active Controls Changing the Rules of Structural Design. Astronaut. & Aeronaut., vol. 10, no. 8, Aug. 1972, pp. 50-55.

2. Abel, Irving; Perry, Boyd, III; and Murrow, Harold N.: Two Synthesis Techniques Applied to Flutter Suppression on a Flight Research Wing. J. Guid. & Control, vol. 1, no. 5, Sept.-Oct. 1978, pp. 341-346.

3. Doggett, Robert V., Jr.; and Townsend, James L.: Flutter Suppression by Active Control and Its Benefits. Proceedings of the SCAR Conference - Part 1, NASA CP-001, [1977], pp. 303-333.

4. Sanford, Maynard C.; Abel, Irving; and Gray, David L.: Development and Demonstration of a Flutter-Suppression System Using Active Controls. NASA TR R-450, 1975.

5. Sevart, Francis D.: Development of Active Flutter Suppression Wind Tunnel Testing Technology. AFFDL-TR-74-126, U.S. Air Force, Jan. 1975.

6. Roger, Kenneth L.; Hodges, Garold E.; and Felt, Larry: Active Flutter Suppression - A Flight Test Demonstration. J. Aircr., vol. 12, no. 6, June 1975, pp. 551-556.

7. Murrow, H. N.; and Eckstrom, C. V.: Drones for Aerodynamic and Structural Testing (DAST) - A Status Report. J. Aircr., vol. 16, no. 8, Aug. 1979, pp. 521-526.

8. Nissim, E.; and Abel, I.: Development and Application of an Optimization Procedure for Flutter Suppression Using the Aerodynamic Energy Concept. NASA TP-1137, 1978.

9. Newsom, Jerry R.: A Method for Obtaining Practical Flutter-Suppression Control Laws Using Results of Optimal Control Theory. NASA TP-1471, 1979.

10. Nissim, E.: Flutter Suppression Using Active Controls Based on the Concept of Aerodynamic Energy. NASA TN D-6199, 1971.

11. Abel, Irving: An Analytical Technique for Predicting the Characteristics of a Flexible Wing Equipped With an Active Flutter-Suppression System and Comparison With Wind-Tunnel Data. NASA TP-1367, 1979.

12. Nissim, E.: Recent Advances in Aerodynamic Energy Concept for Flutter Suppression and Gust Alleviation Using Active Controls. NASA TN D-8519, 1977.

13. Kwakernaak, Huibert; and Sivan, Raphael: Linear Optimal Control Systems. John Wiley & Sons, Inc., c.1972.

14. Davidon, William C.: Variable Metric Method for Minimization. ANL-5990, Rev. (Contract W-31-109-eng-38), U.S. At. Energy Comm., Nov. 1959.

15. Fletcher, R.; and Powell, M. J. D.: A Rapidly Convergent Descent Method for Minimization. Computer J., vol. 6, no. 2, July 1963, pp. 163-168.

16. Dougherty, N. S., Jr.: Prepared Comment on the Cone Transition Reynolds Number Data Correlation Study. Flight/Ground Testing Facilities Correlation, AGARD-CP-187, 1976, pp. 3A-1 - 3A-7.

17. Peloubet, R. P., Jr.; Haller, R. L.; Cunningham, A. M.; Cwach, E. E.; and Watts, D.: Application of Three Aeroservoelastic Stability Analysis Techniques. AFFDL-TR-76-89, U.S. Air Force, Sept. 1976.

18. Hausner, Arthur: Analog and Analog/Hybrid Computer Programming. Prentice-Hall, Inc., c.1971.

TABLE I.- CALCULATED FREQUENCY, GENERALIZED MASS, AND MODAL DISPLACEMENT DATA

Mode	Natural frequency, Hz	Generalized mass, kg	Modal displacements	
			Outboard accelerometer	Inboard accelerometer
1	5.23	3.68	0.923	0.767
2	19.13	7.77	-.636	-.470
3	20.91	7.04	-.000	-.000
4	25.77	2.97	.345	-.205
5	46.11	4.71	.176	-.359
6	61.23	4.76	.236	-.751
7	79.68	5.16	.020	-.663
8	86.03	11.30	.000	.001
9	98.09	7.56	.044	-.997
10	118.15	5.50	.017	-.121

TABLE II.- SUMMARY OF ANALYTICAL CLOSED-LOOP RESULTS

Analysis condition		Aerodynamic energy h_{inbd}				Aerodynamic energy h_{outbd}				Optimal control law h_{outbd}			
M	q_{max}, kPa (a)	q_f, kPa	f_f, Hz	$\delta_{a,rms}$, deg (b)	$\dot{\delta}_{a,rms}$, deg/sec (b)	q_f, kPa	f_f, Hz (c)	$\delta_{a,rms}$, deg (b)	$\dot{\delta}_{a,rms}$, deg/sec (b)	q_f, kPa	f_f, Hz	$\delta_{a,rms}$, deg (b)	$\dot{\delta}_{a,rms}$, deg/sec (b)
0.6	10.62	>12	---	5.2	235	11.83	24.0	5.9	245	11.93	6.7	6.2	309
.7	9.79	>12	---	4.7	225	10.73	23.9	5.1	227	10.89	6.9	5.8	298
.8	8.69	11.40	5.3	4.2	215	9.62	23.7	4.5	211	9.93	7.1	5.2	270
.9	7.24	10.44	5.3	3.6	187	8.28	23.4	3.7	186	9.03	7.0	4.1	218
.95	6.34	------	---	---	---	7.57	23.2	3.3	165	8.76	6.9	3.3	180

[a] $1.44q_f$ (analysis) from figure 5.
[b] Evaluated at $q = q_{max}$.
[c] Instability in mode 2.

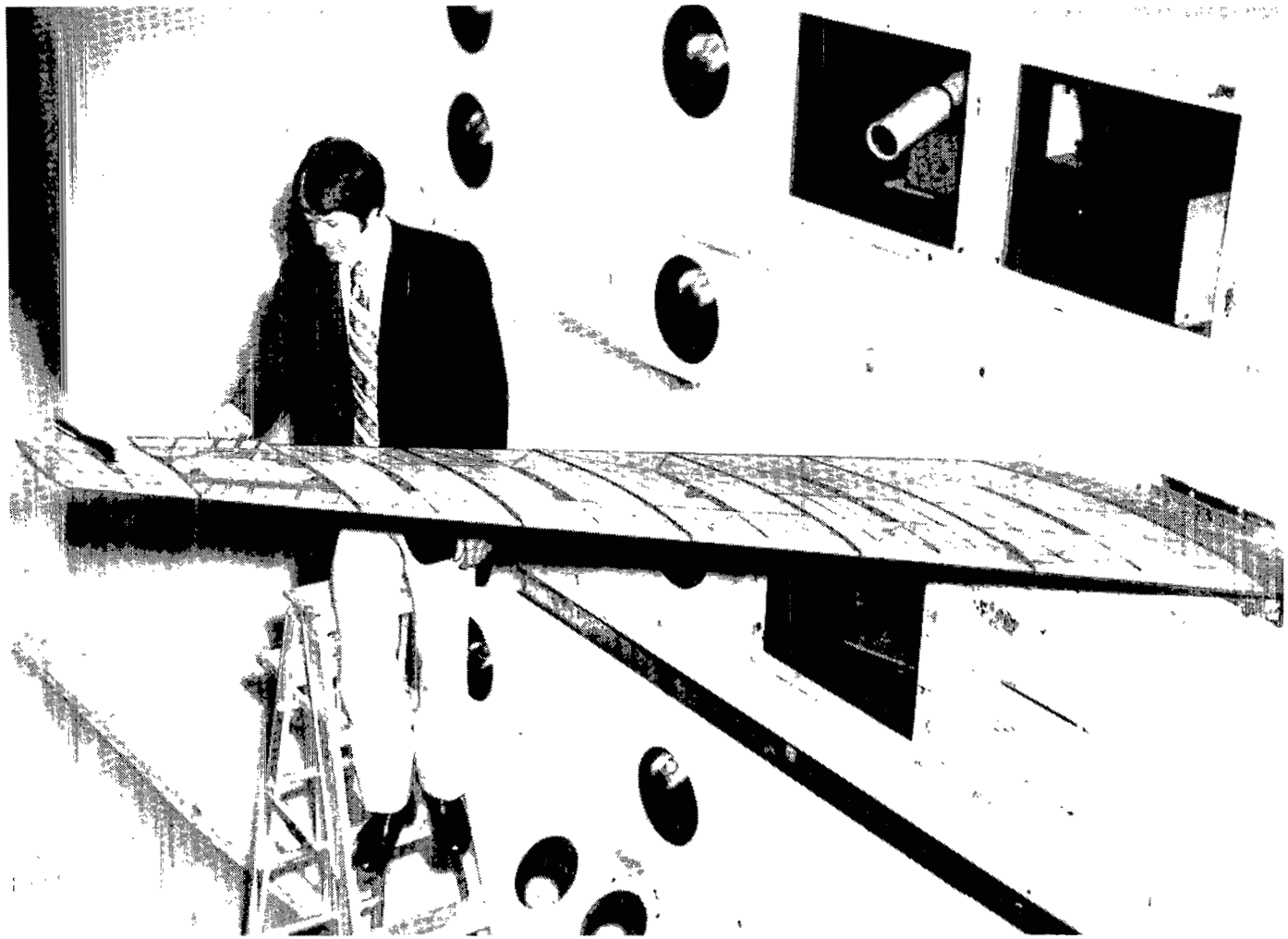

L-78-976

Figure 1.- Flutter-suppression model in Langley Transonic Dynamics Tunnel.

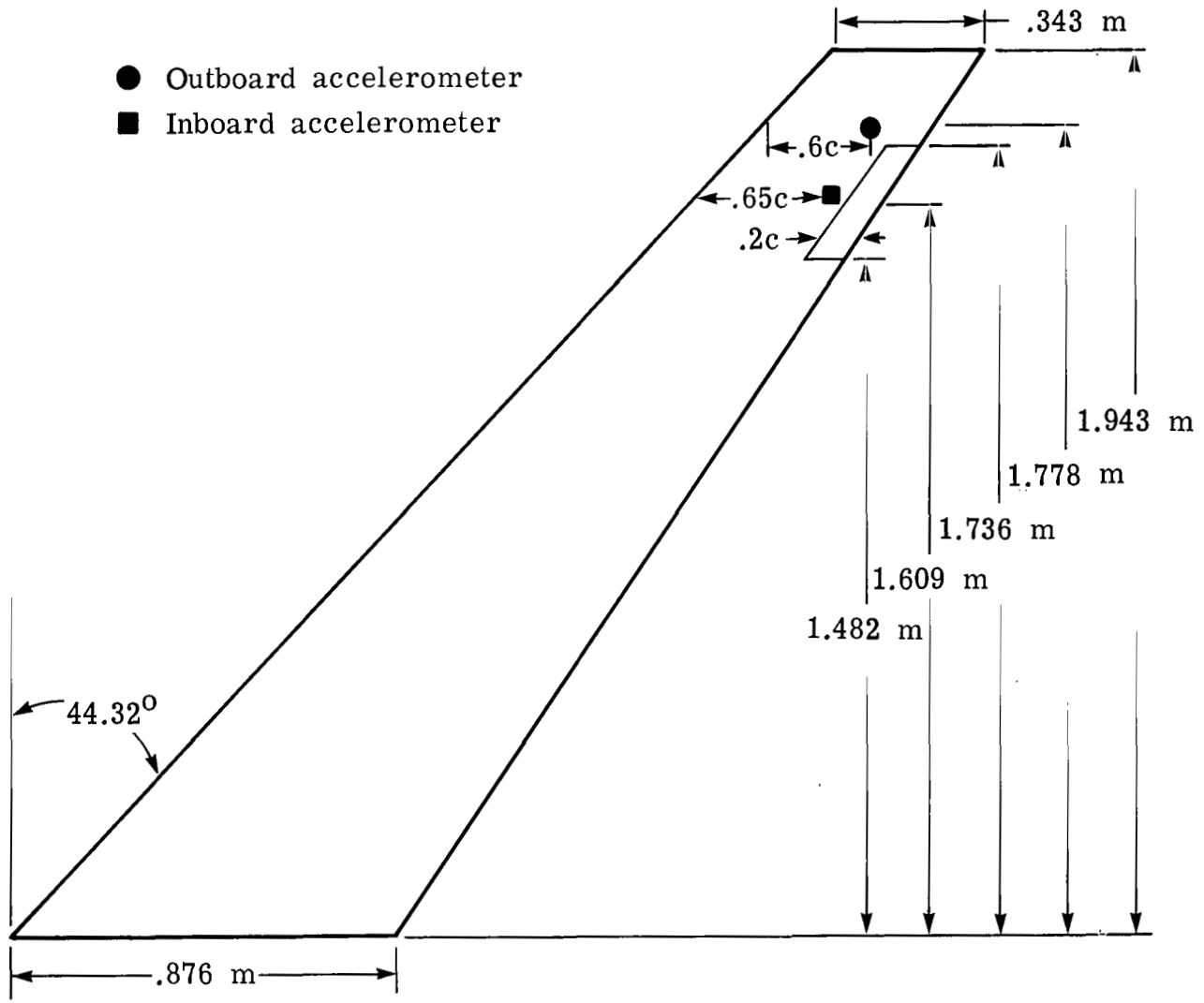

Figure 2.- Model geometry.

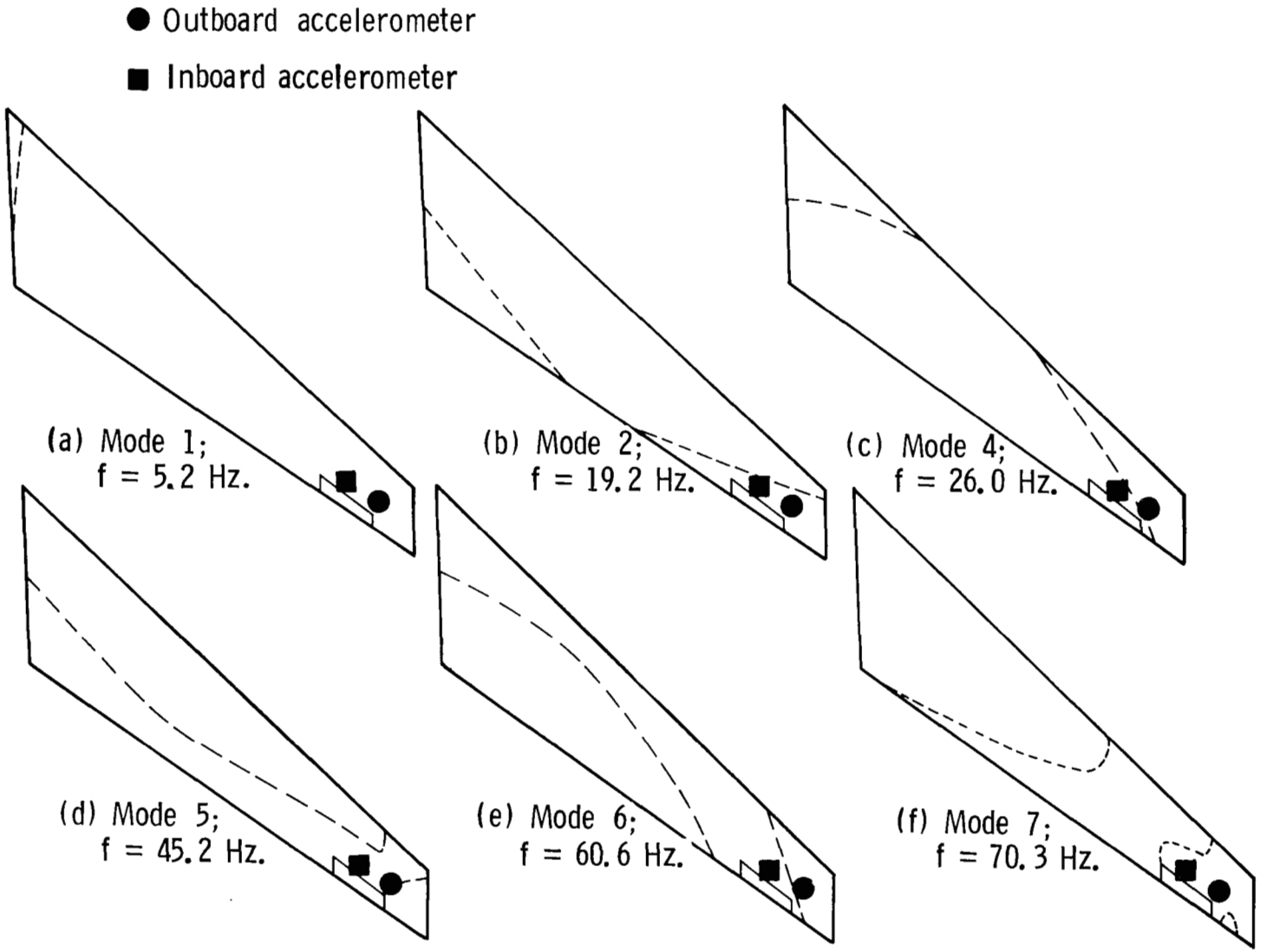

Figure 3.- Measured node lines and frequencies of first six natural vibration modes.

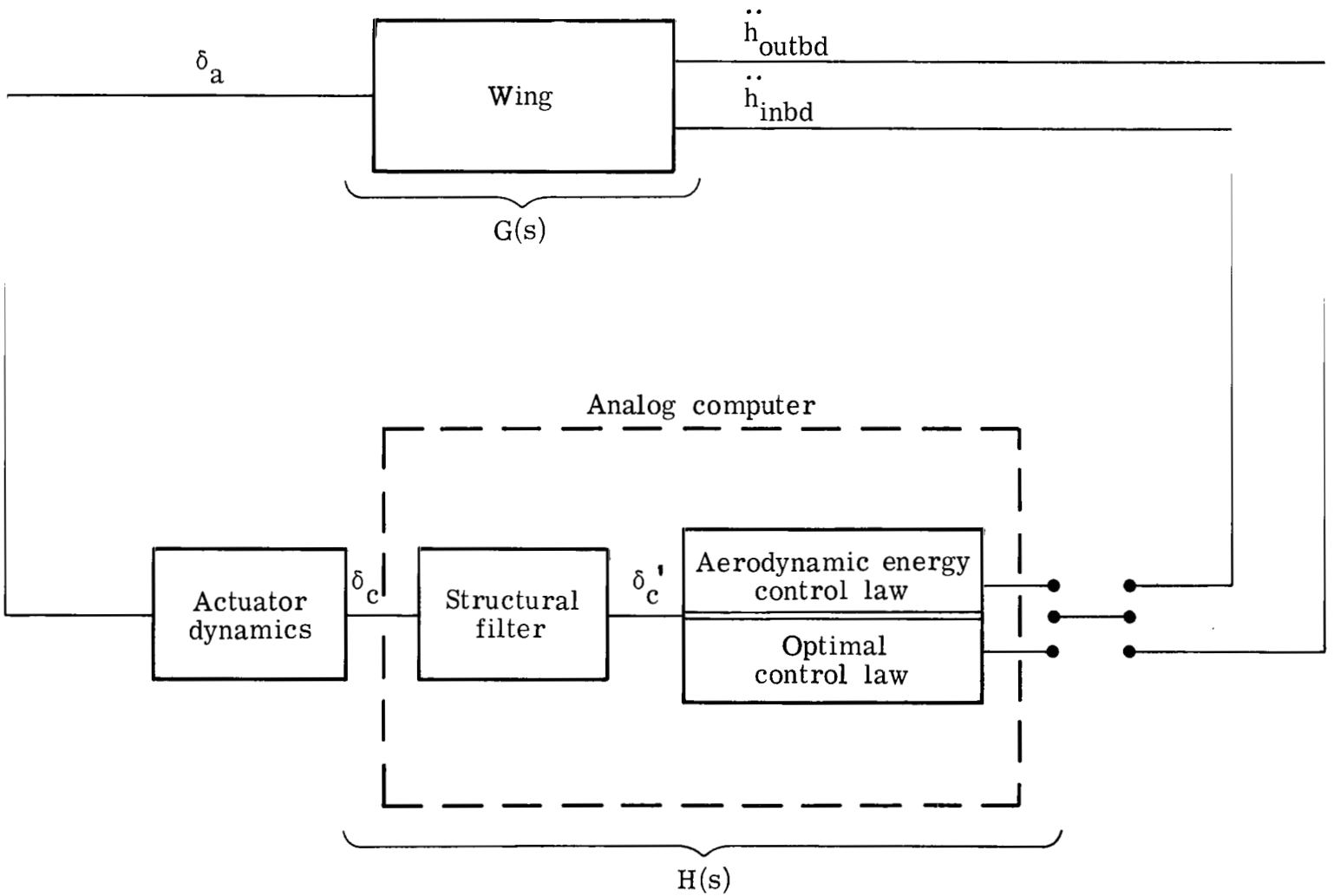

Figure 4.- Simplified block diagram of flutter-suppression system.

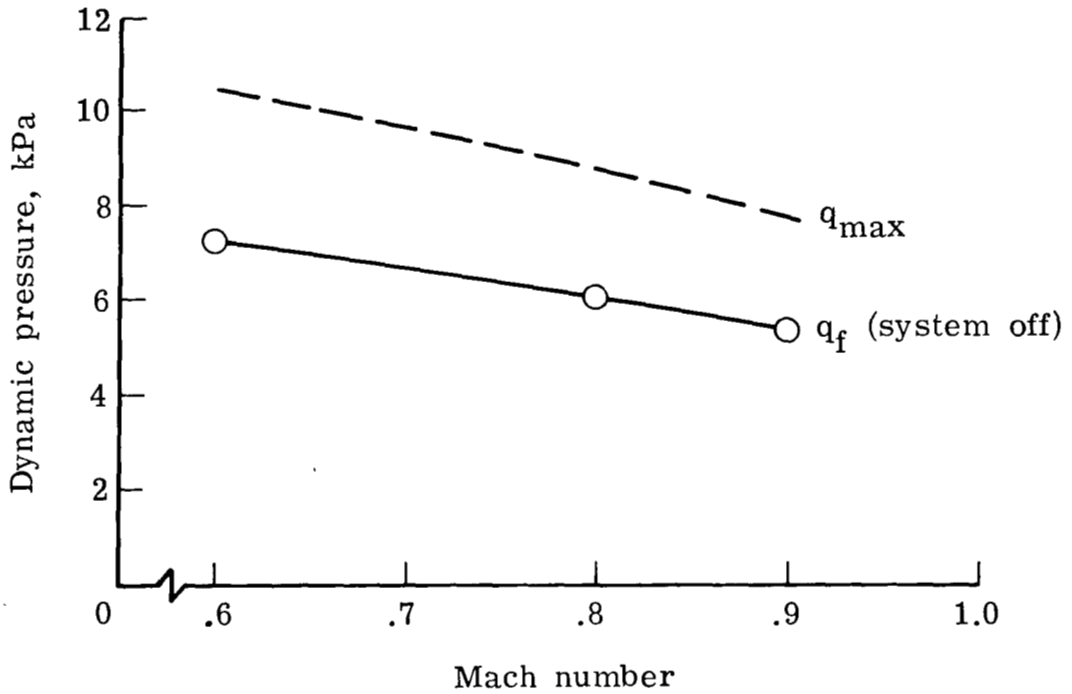

Figure 5.- Calculated flutter boundary (system off) used for flutter-suppression control-law design.

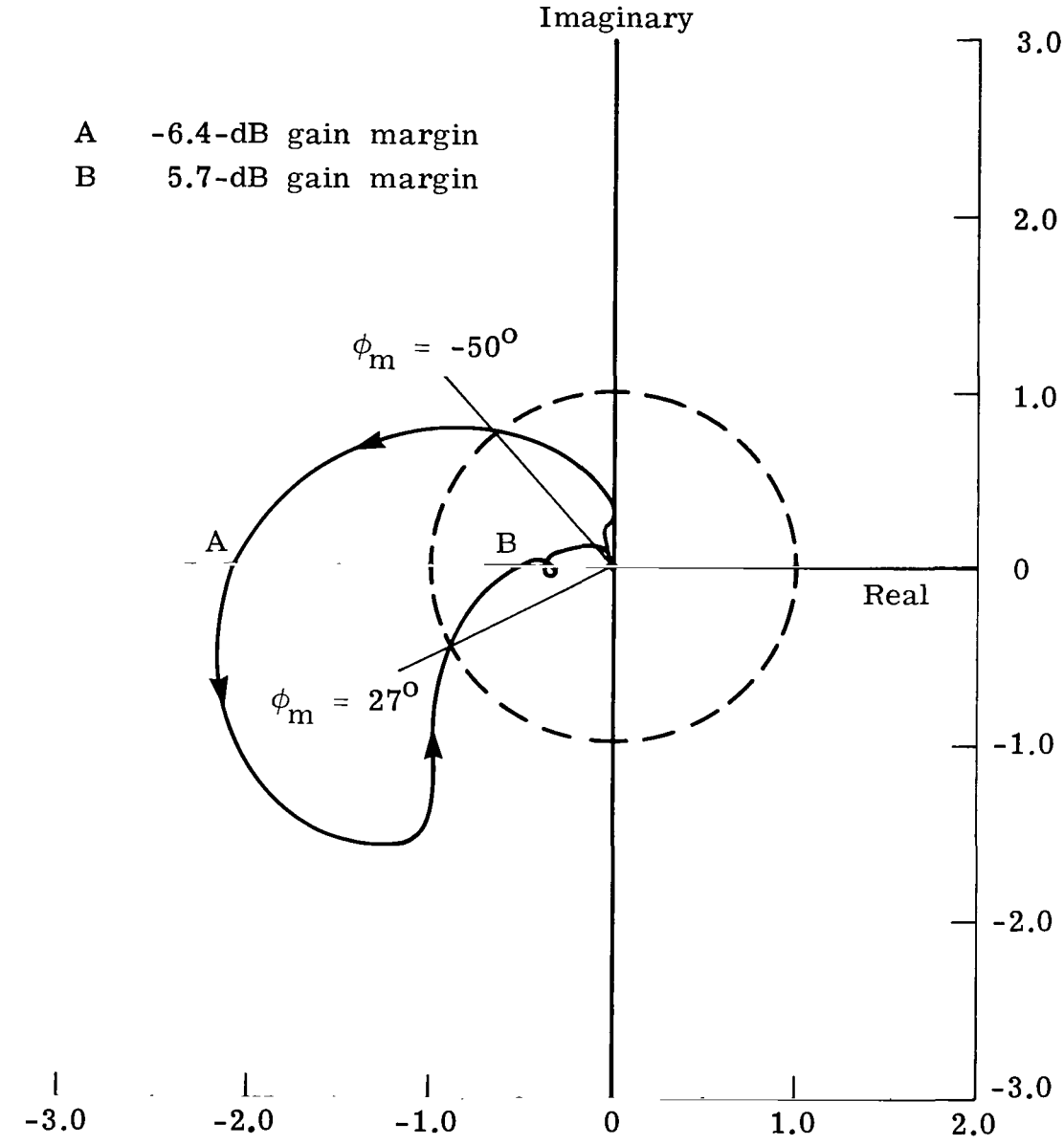

Figure 6.- Nyquist plot of open-loop transfer function $G(i\omega)\,H(i\omega)$. $M = 0.9$; $q = q_{max}$. ($H(i\omega)$ defined by eq. (5); arrows indicate increasing frequency.)

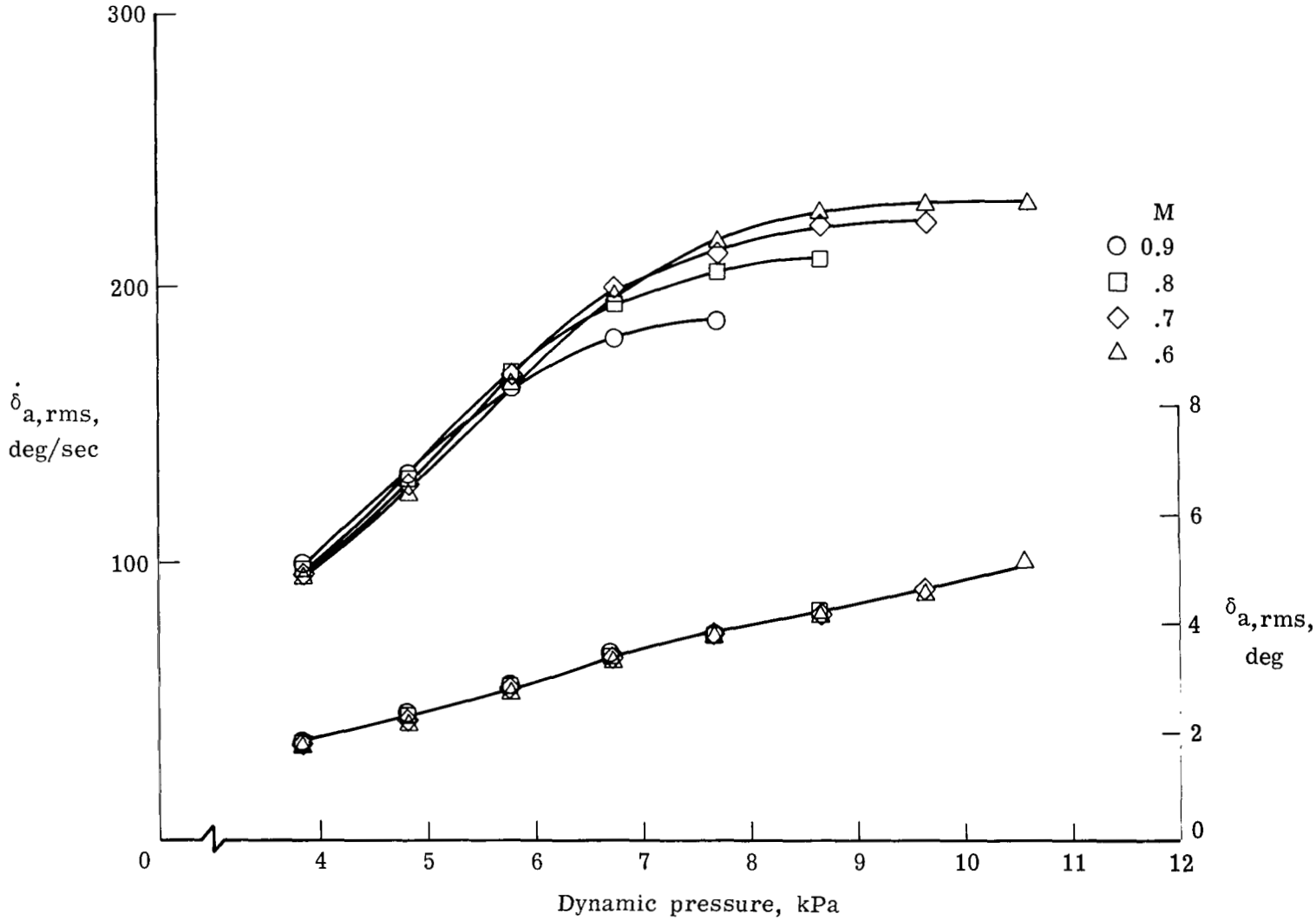

Figure 7.- Variation with dynamic pressure of rms response of control surface at various Mach numbers. (Control law defined by eq. (5).)

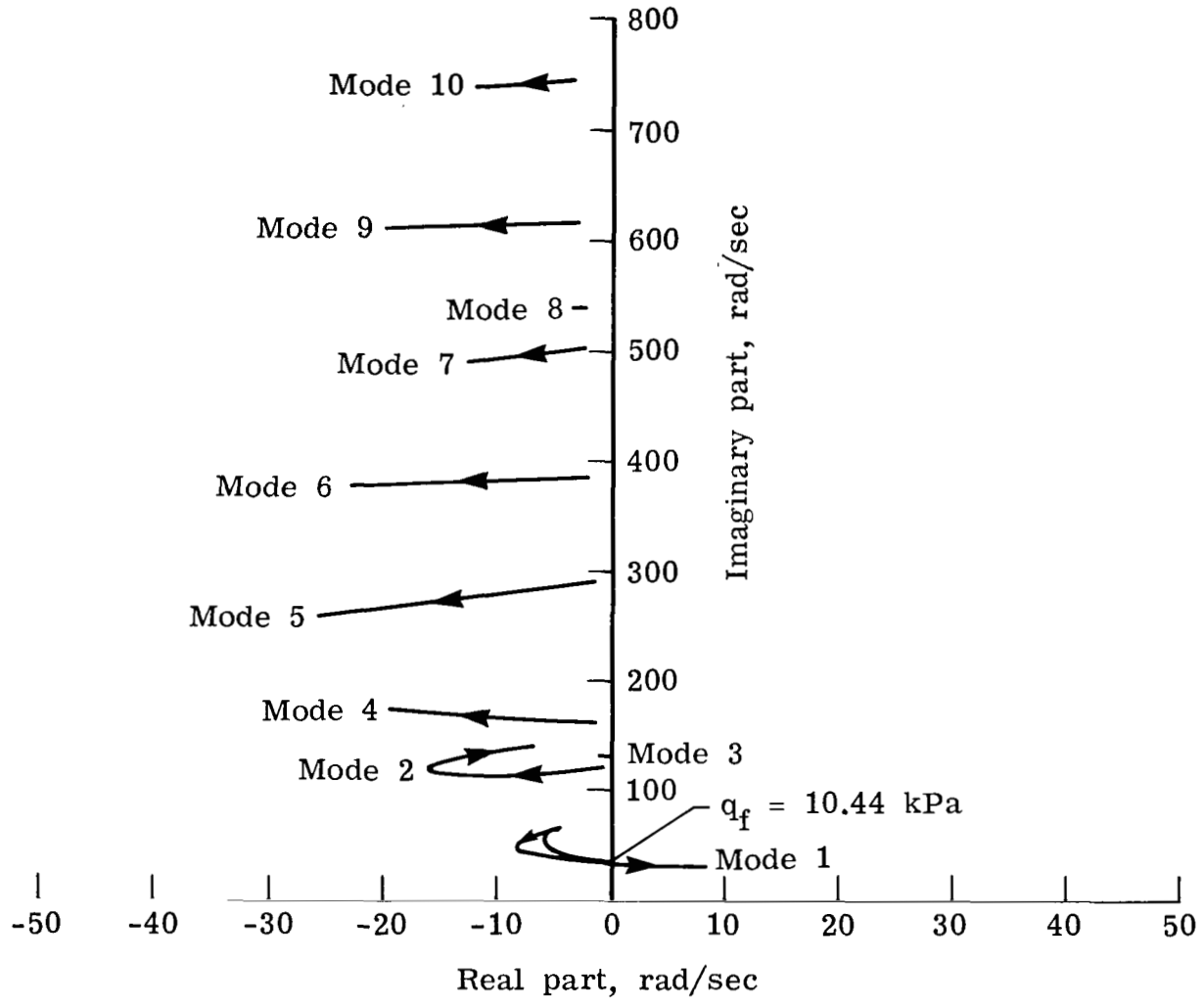

Figure 8.- Closed-loop root locus at M = 0.9. (Control law defined by eq. (5); arrows indicate increasing dynamic pressure.)

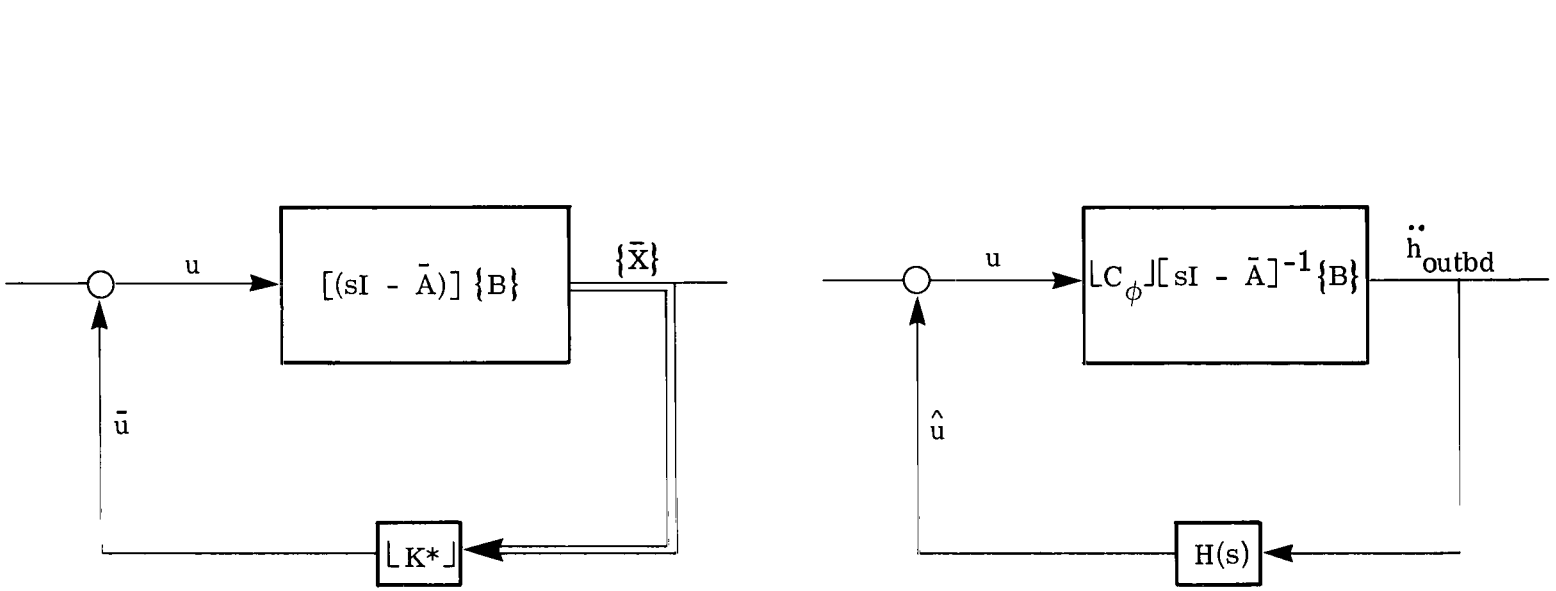

(a) Full state.

(b) Practical.

Figure 9.- Block diagrams of full-state and practical control laws.

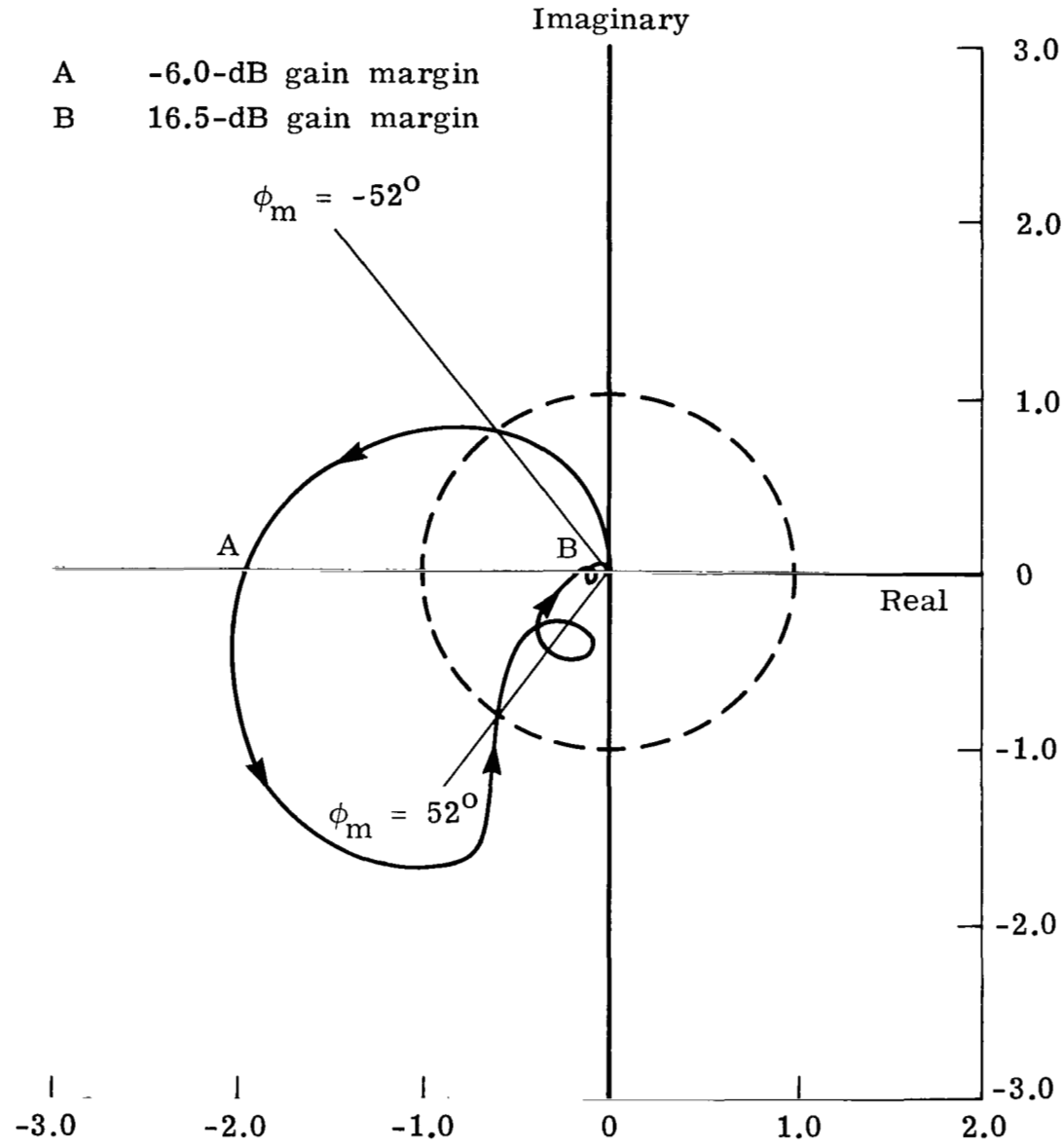

Figure 10.- Nyquist plot of open-loop transfer function $G(i\omega)\,H(i\omega)$. $M = 0.9$; $q = q_{max}$. ($H(i\omega)$ defined by eq. (9); arrows indicate increasing frequency.)

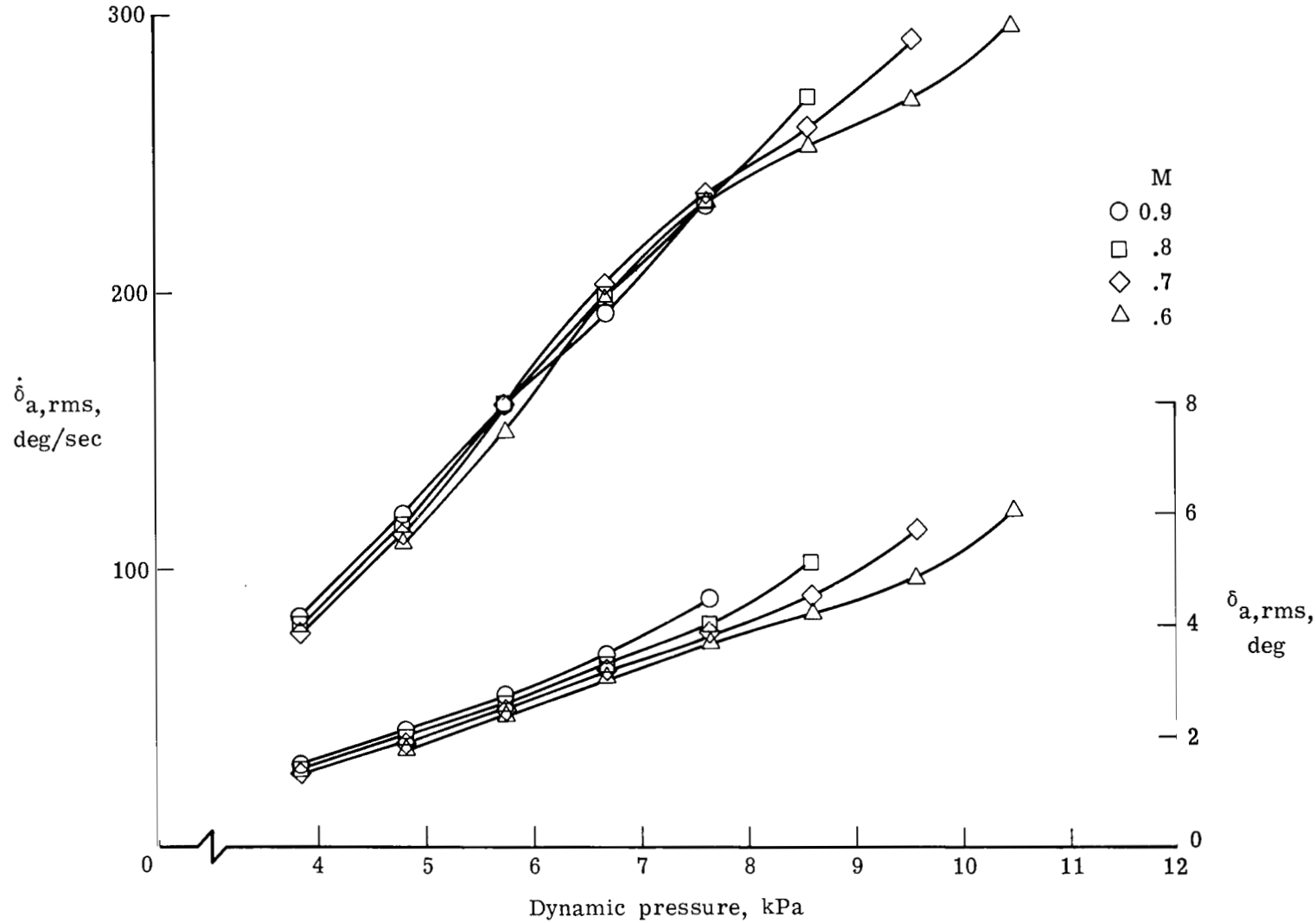

Figure 11.- Variation with dynamic pressure of rms response of control surface at various Mach numbers. (Control law defined by eq. (9).)

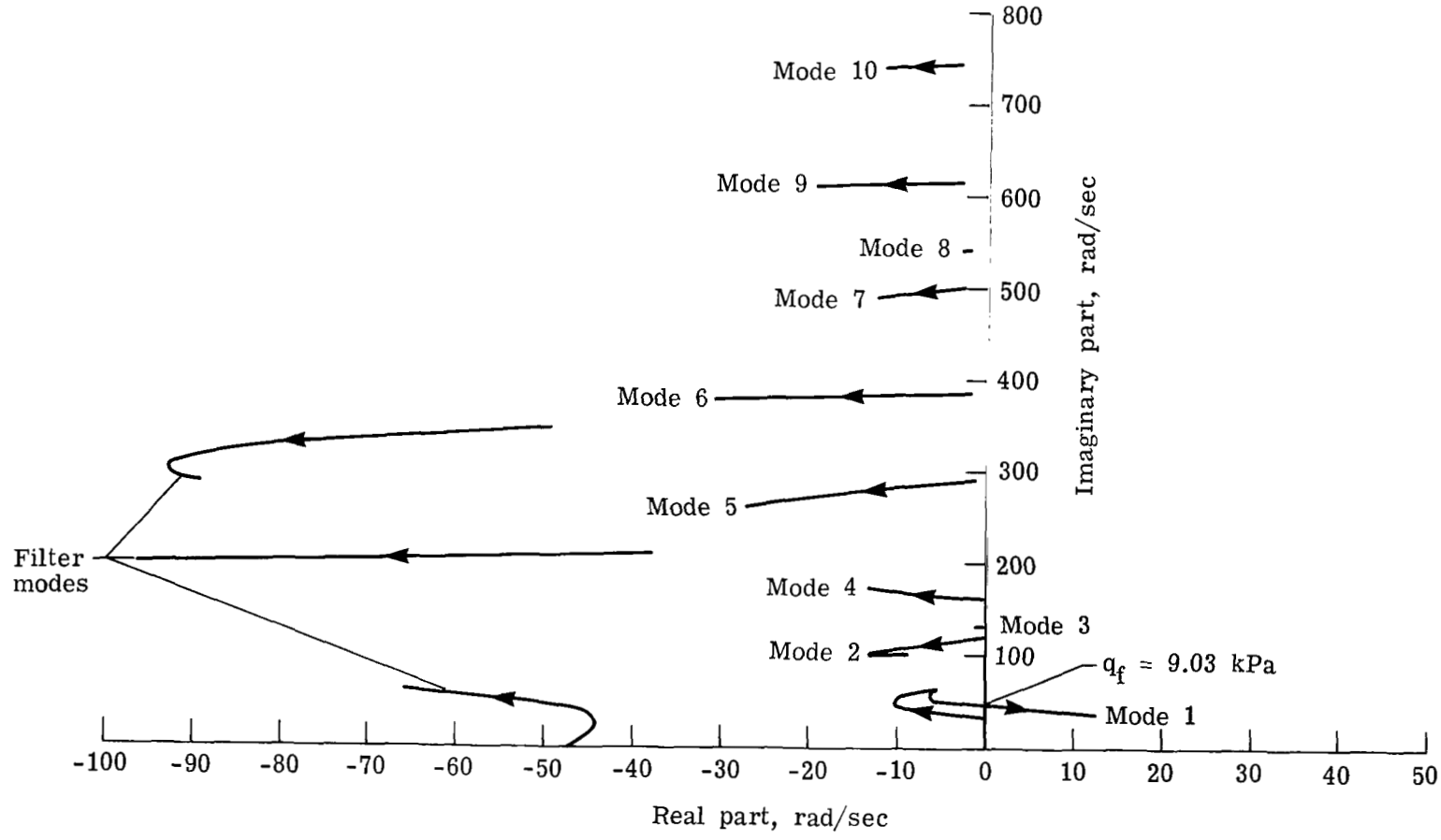

Figure 12.- Closed-loop root locus at M = 0.9. (Control law defined by eq. (9); arrows indicate increasing dynamic pressure.)

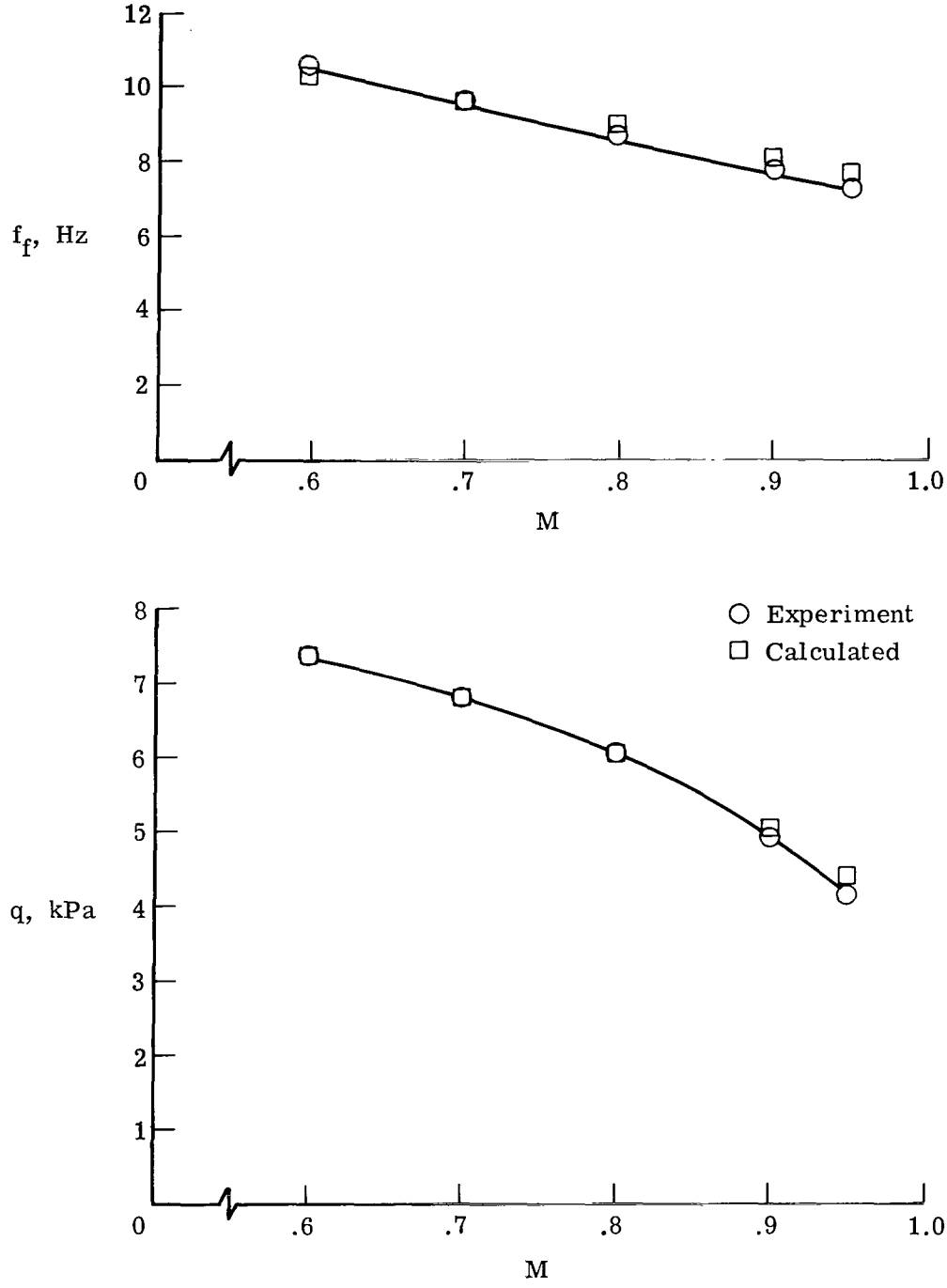

Figure 13.- Comparison of calculated and measured flutter characteristics (system off).

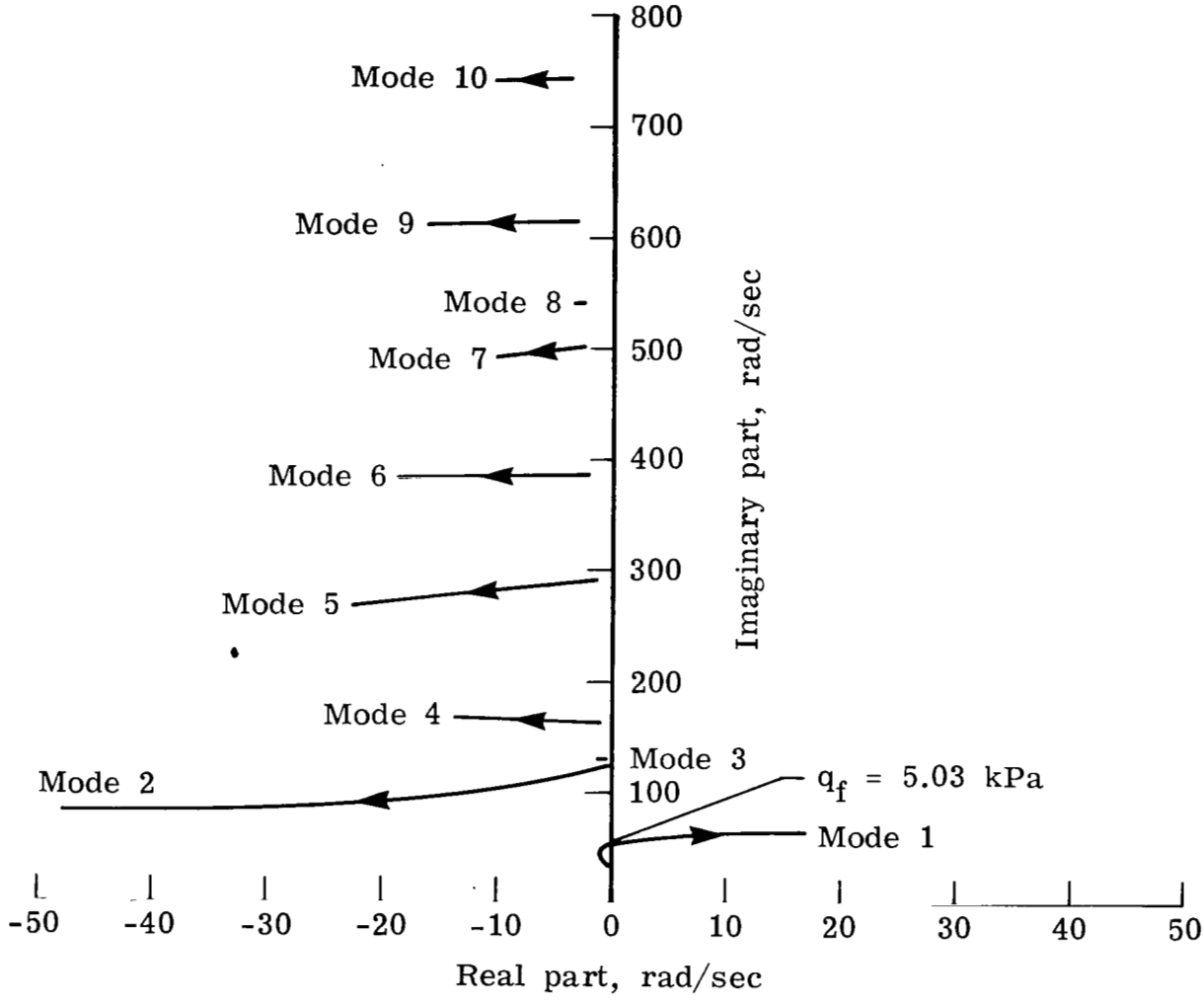

Figure 14.- Root locus at M = 0.9. (System off; arrows indicate increasing dynamic pressure.)

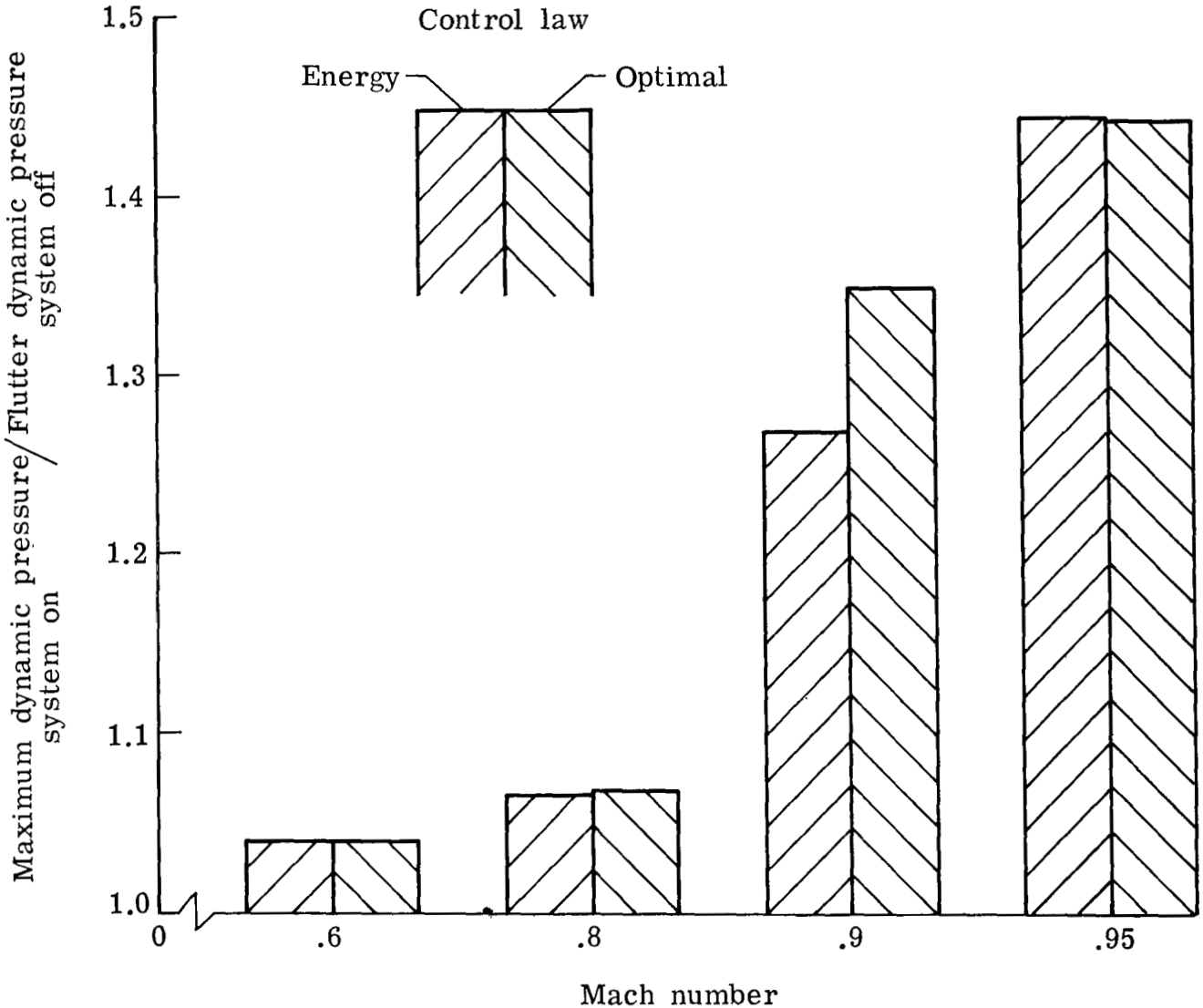

Figure 15.- Maximum dynamic pressures achieved during wind-tunnel tests.

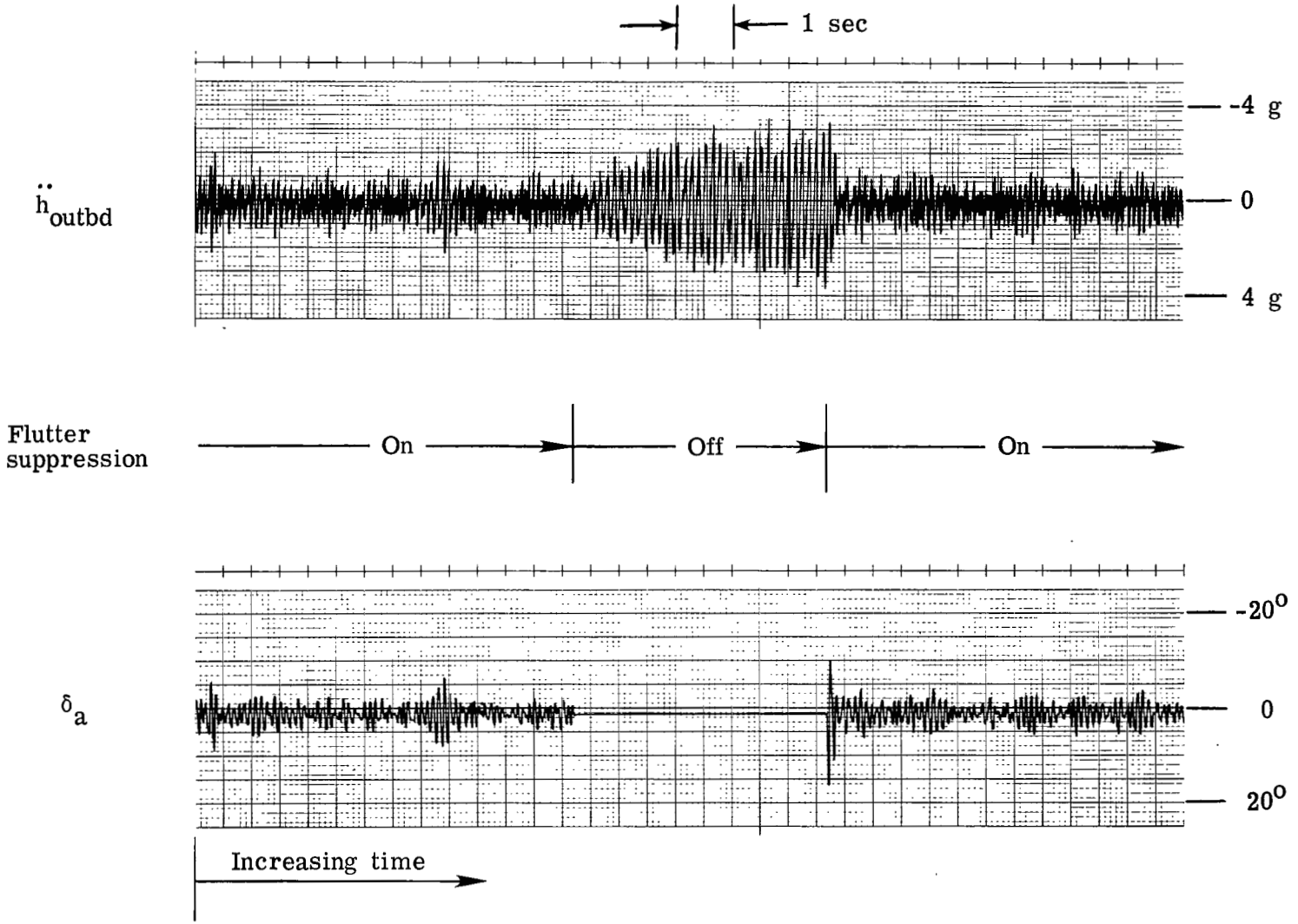

Figure 16.- Time history of acceleration at outboard accelerometer and control-surface deflection.

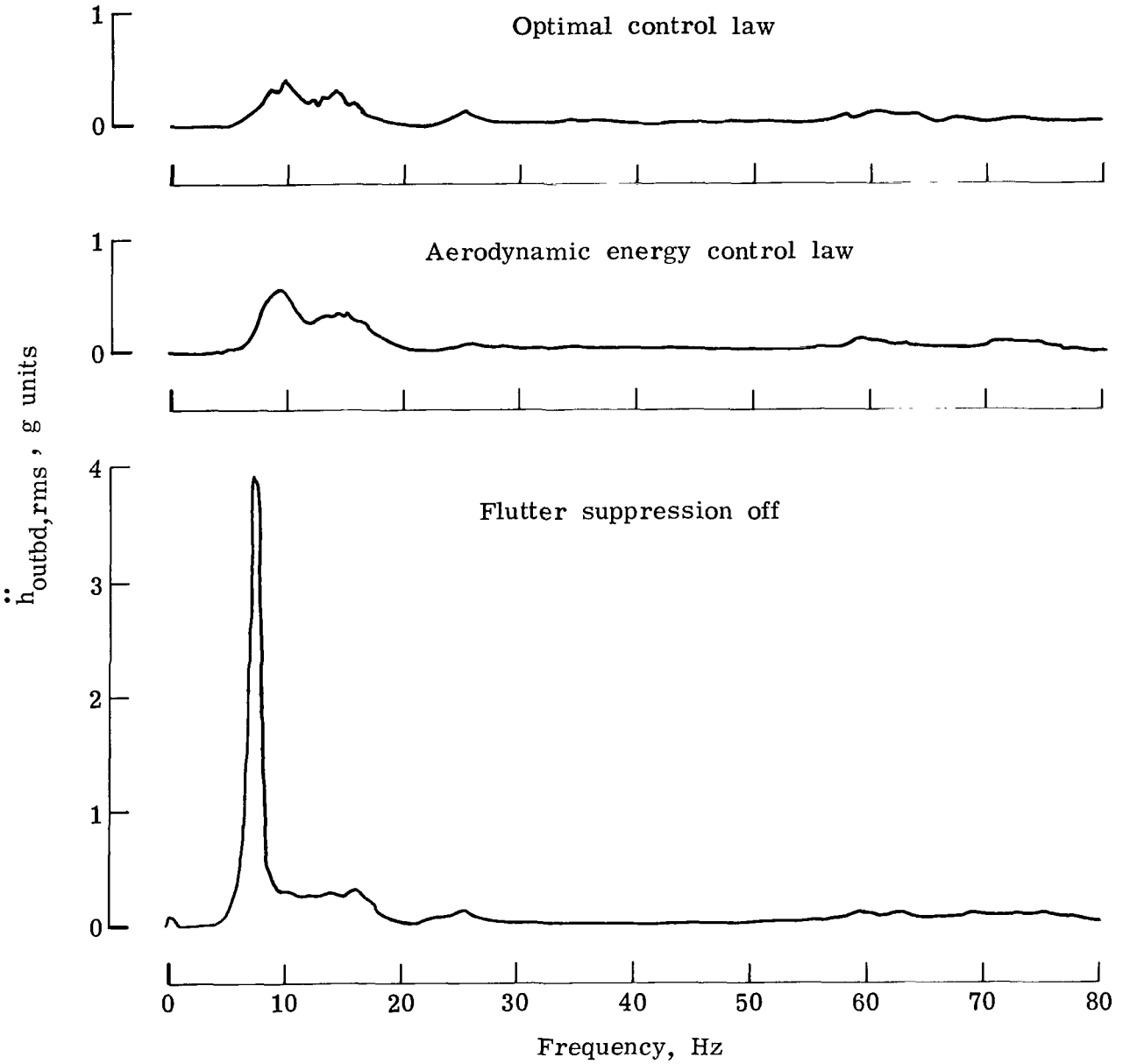

Figure 17.- Comparison of rms acceleration at outboard accelerometer with flutter-suppression system turned on and off. M = 0.9; q = 4.92 kPa.

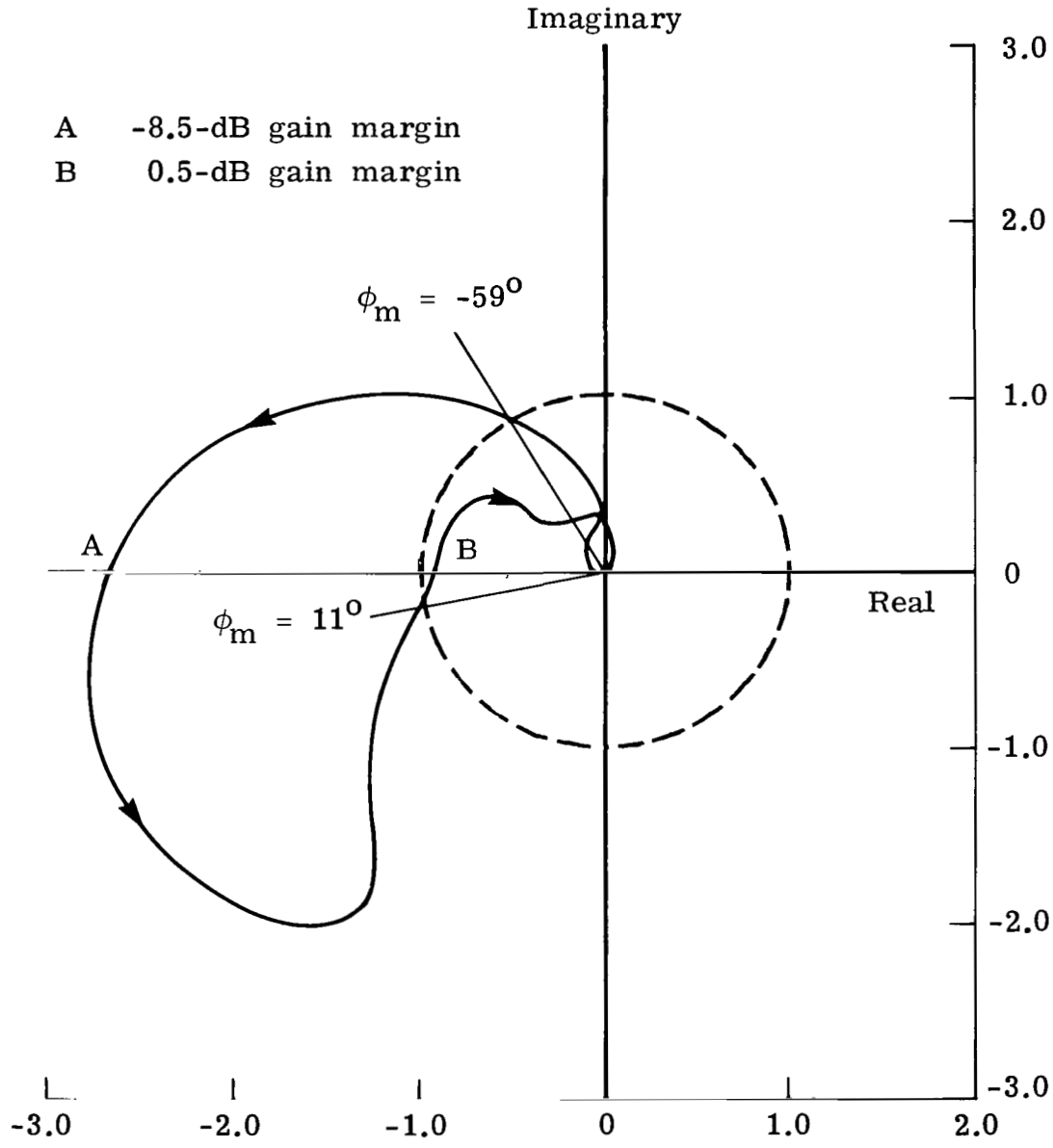

Figure 18.- Nyquist plot of open-loop transfer function for alternate aerodynamic energy control law. M = 0.9; $q = q_{max}$. (Arrows indicate increasing frequency.)

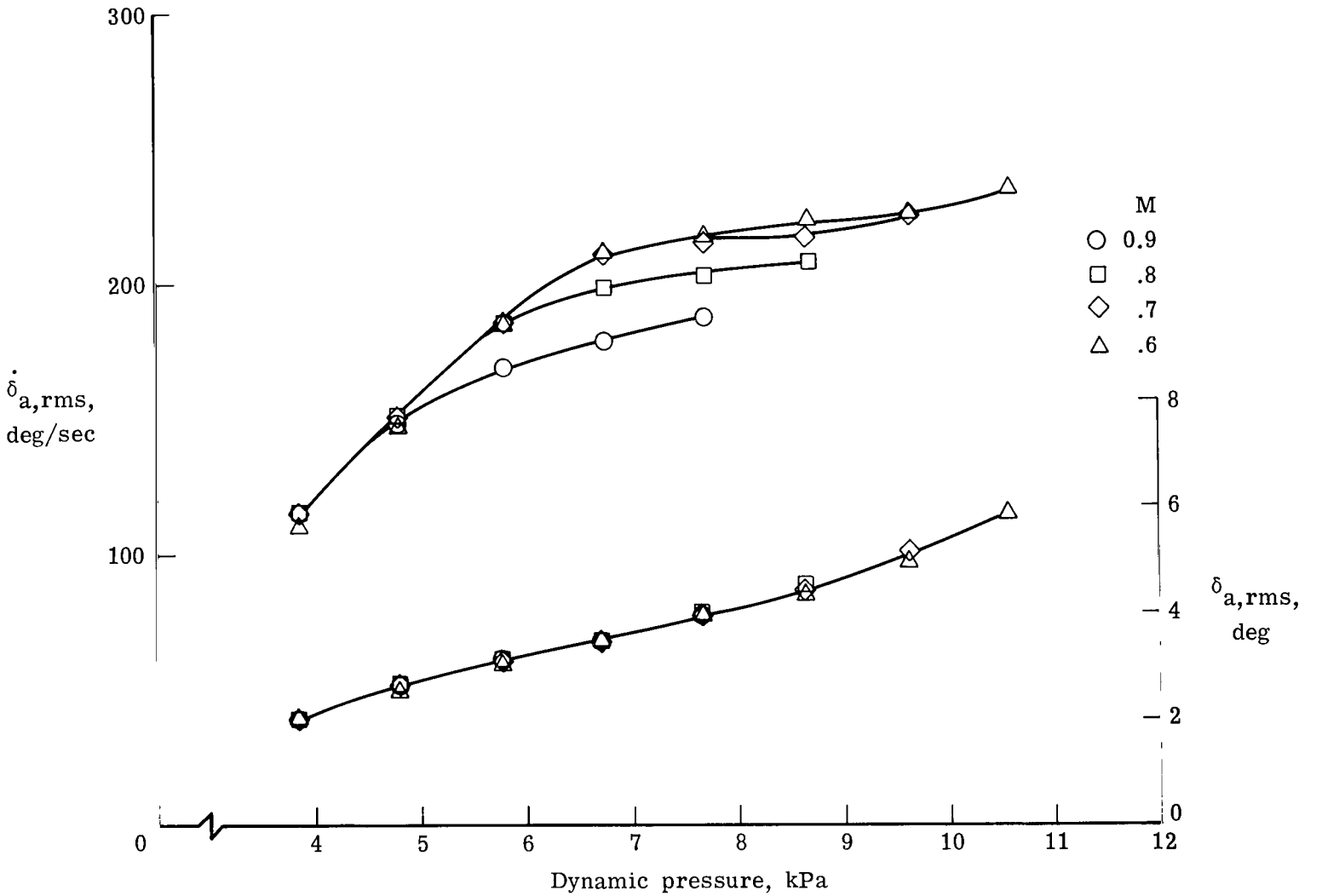

Figure 19.- Variation with dynamic pressure of control-surface rms response for alternate aerodynamic energy control law.

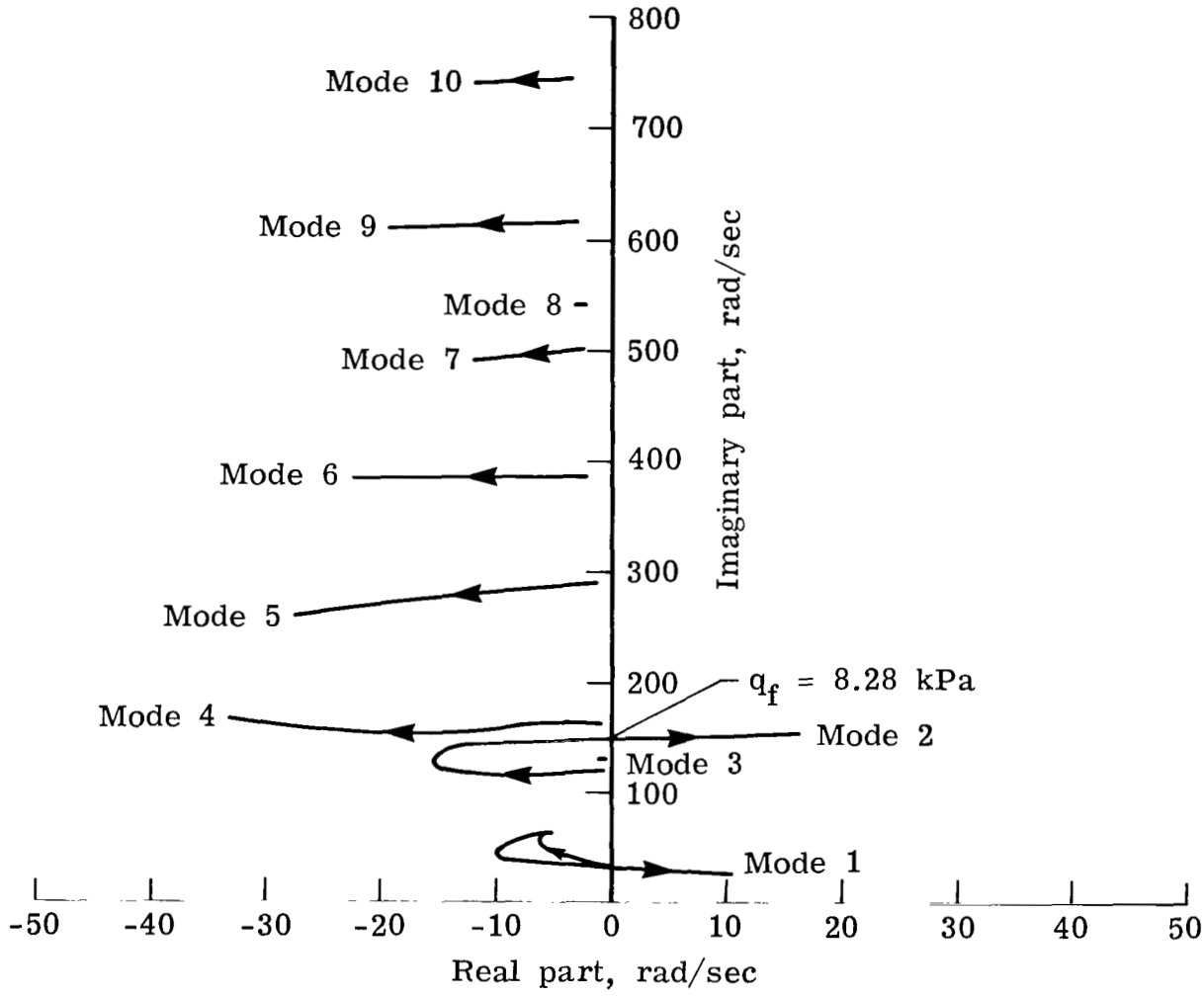

Figure 20.- Closed-loop root locus at M = 0.9 using alternate aerodynamic energy control law.

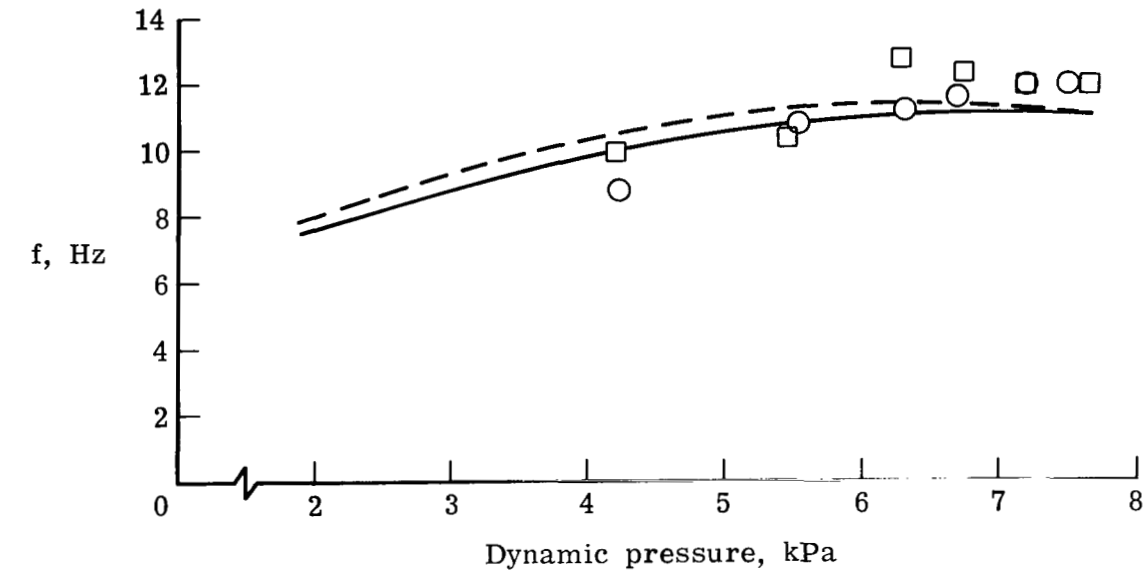

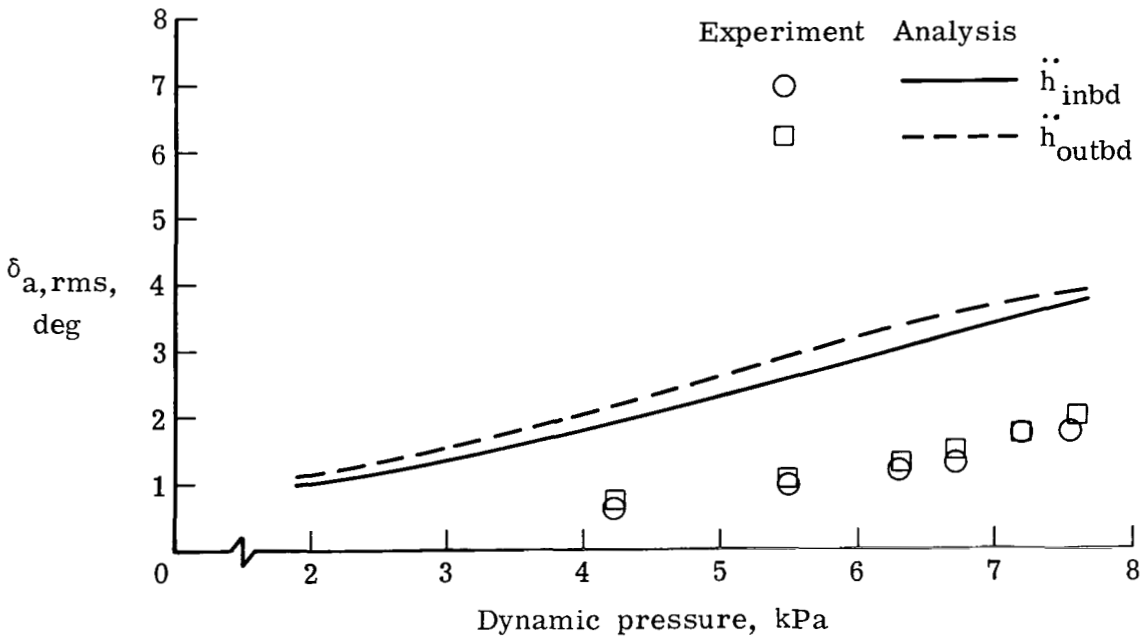

(a) M = 0.6.

Figure 21.- Comparison of experimental and analytical results for aerodynamic energy control law.

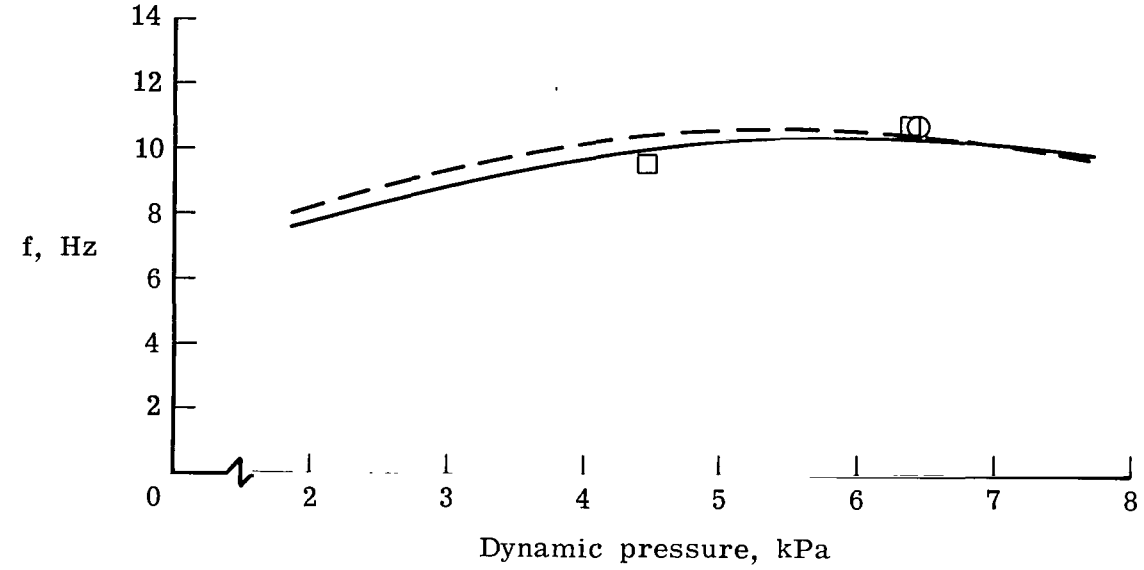

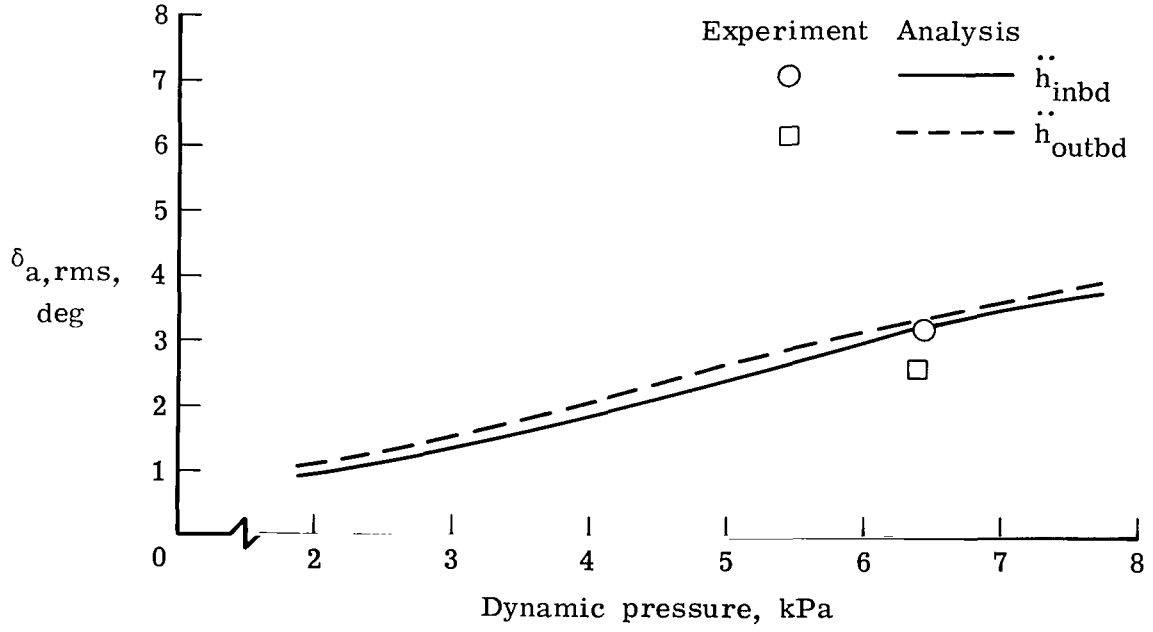

(b) M = 0.8.

Figure 21.- Continued.

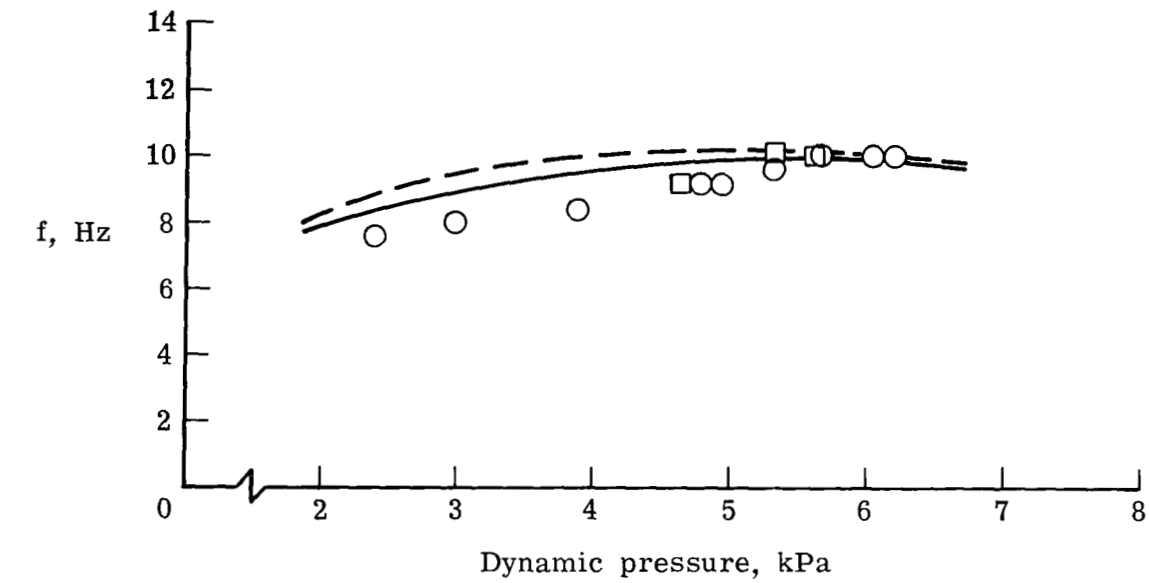

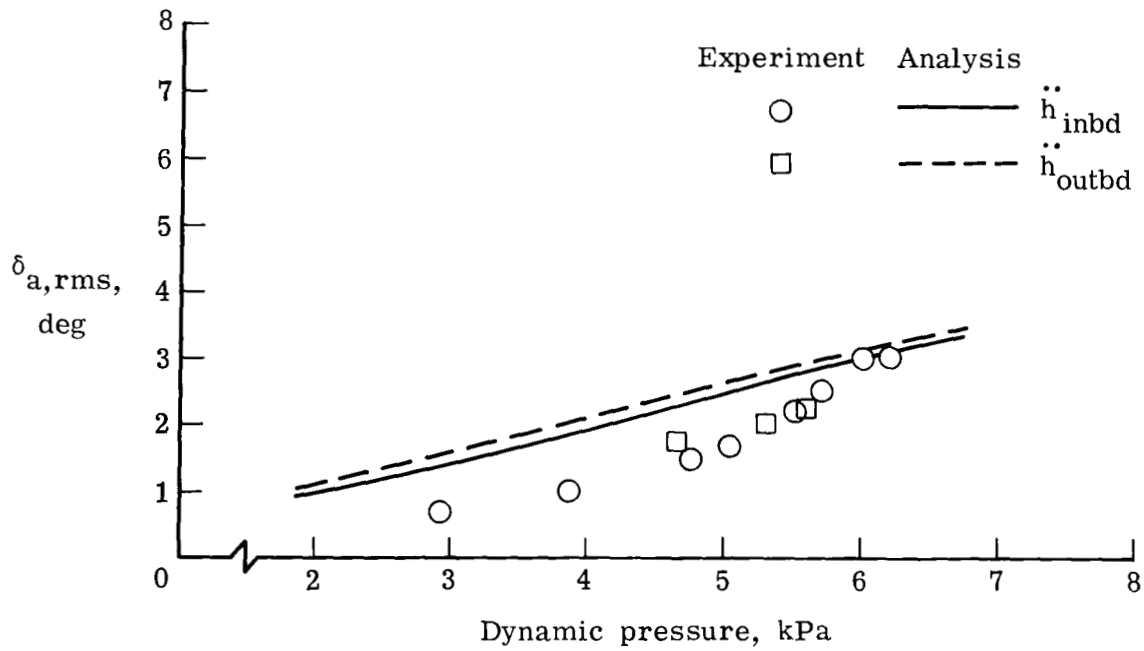

(c) M = 0.9.

Figure 21.- Continued.

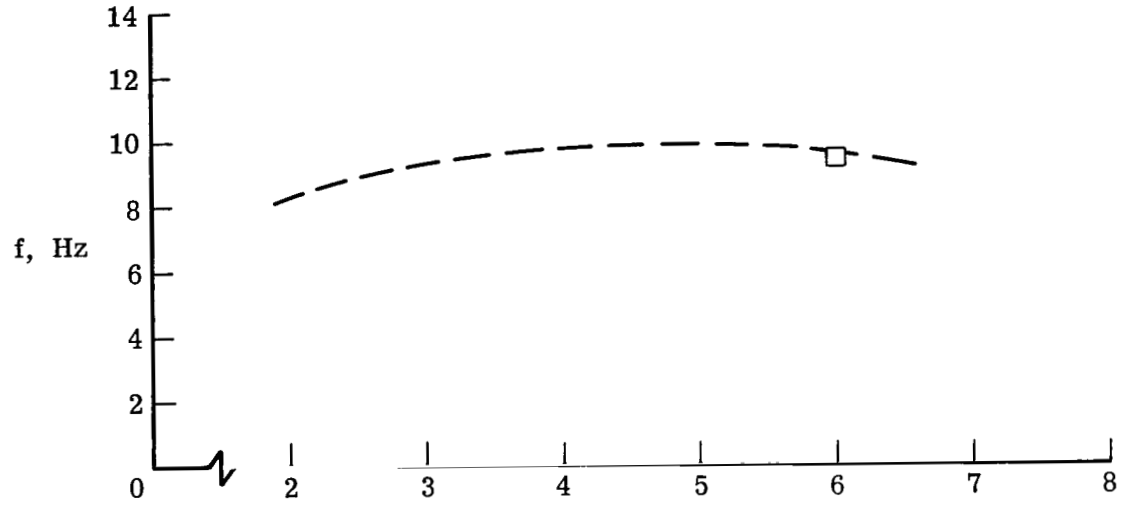

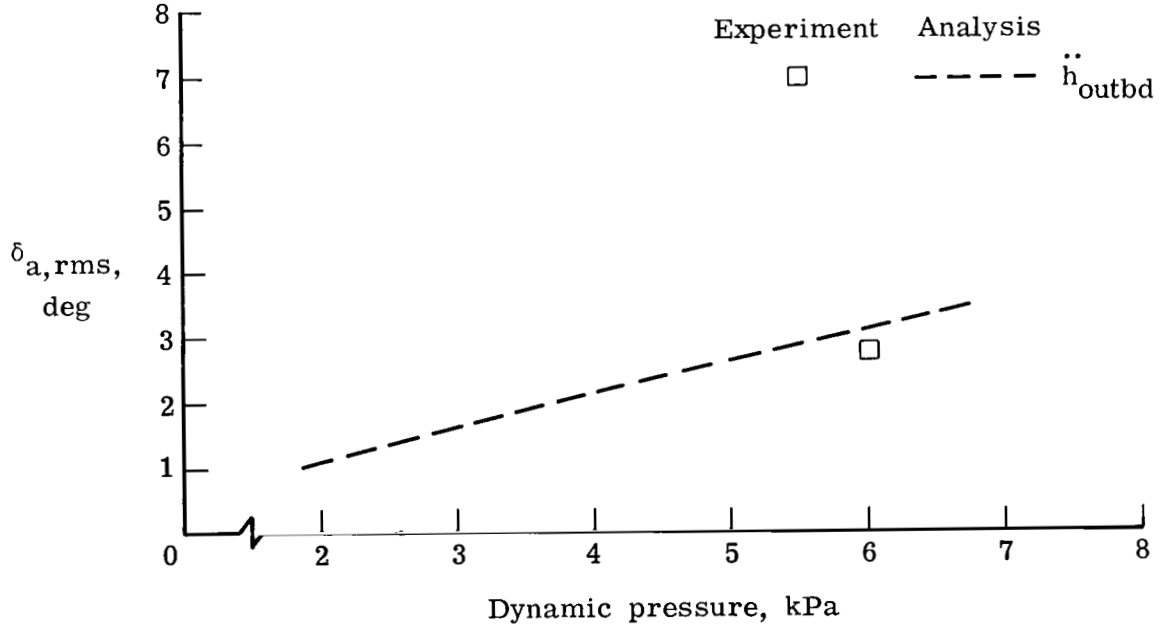

(d) M = 0.95.

Figure 21.- Concluded.

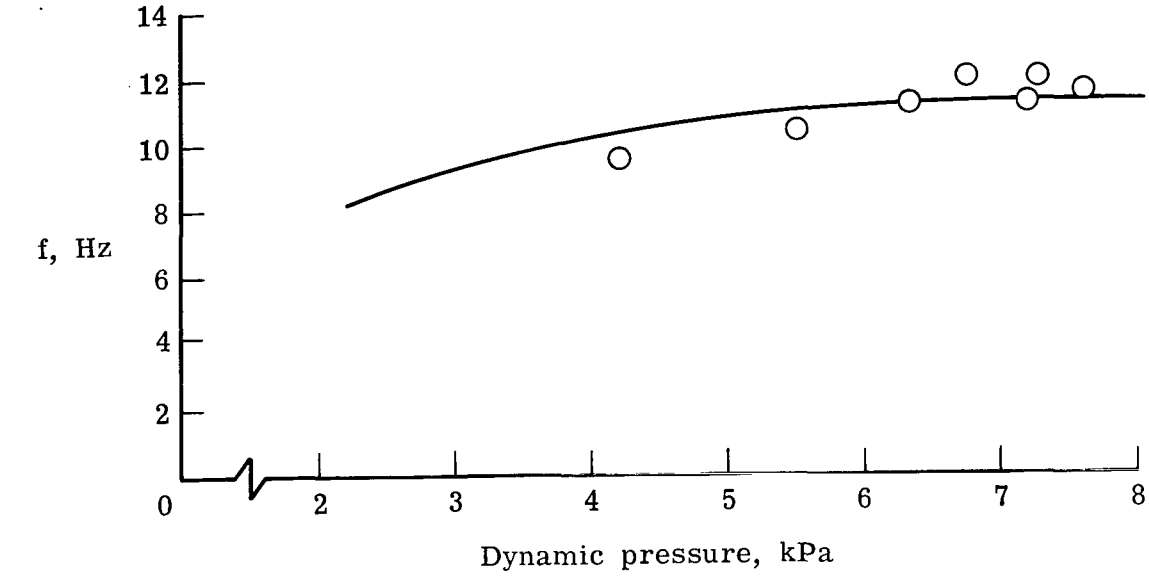

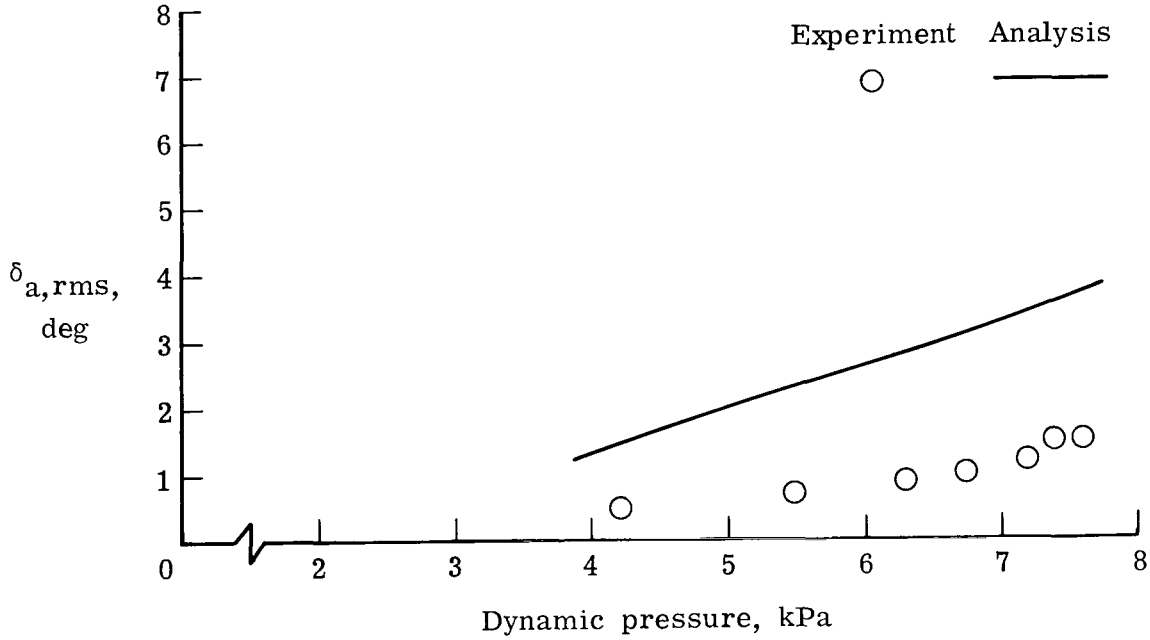

(a) M = 0.6.

Figure 22.- Comparison of experimental and analytical results for optimal control theory control law.

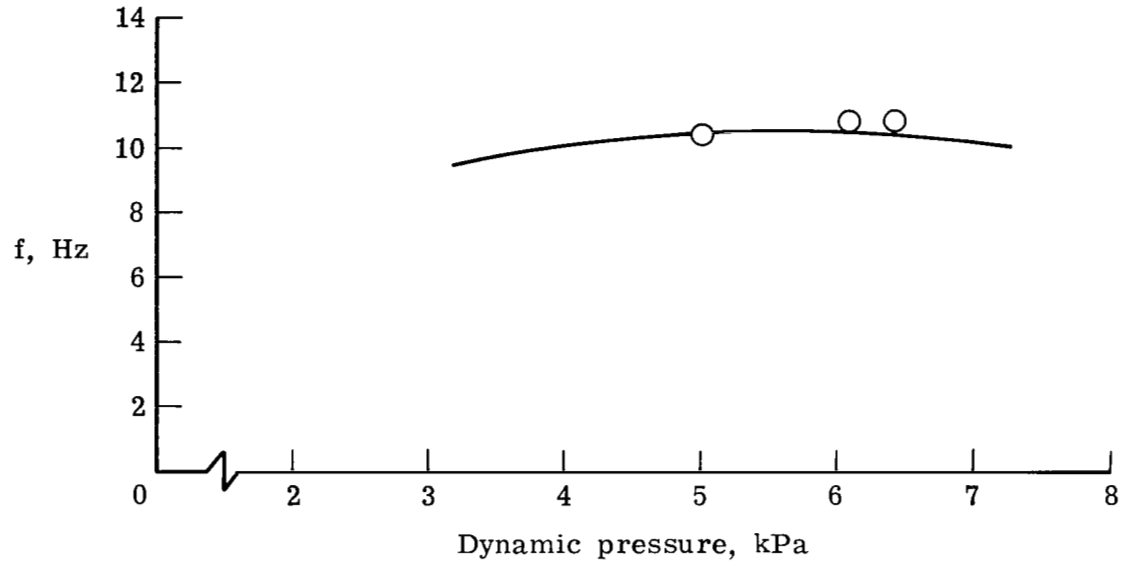

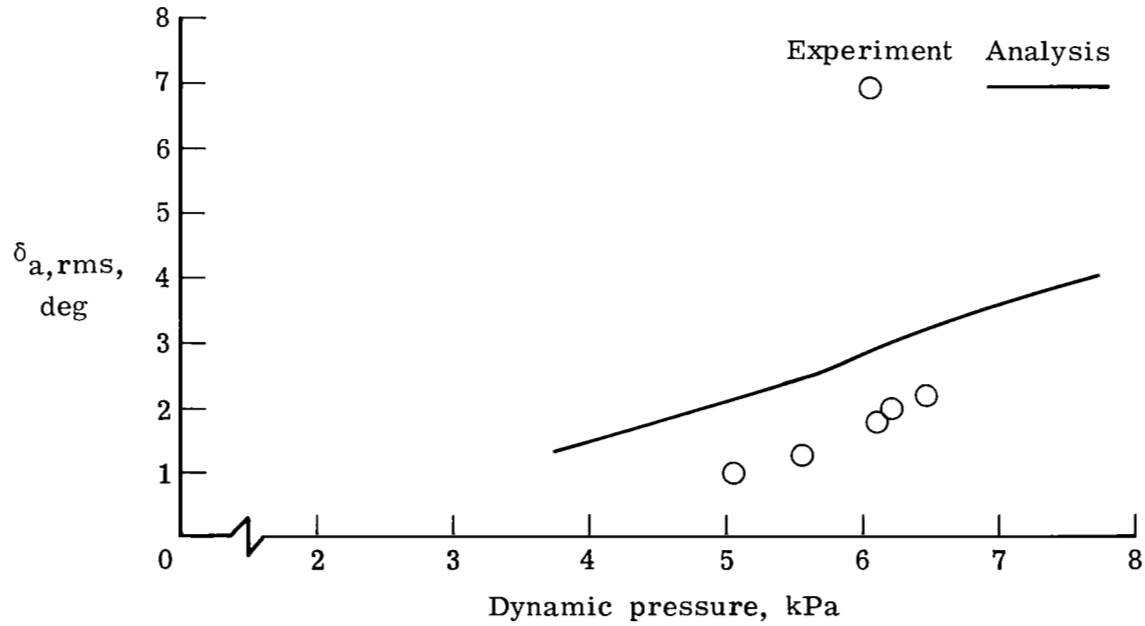

(b) M = 0.8.

Figure 22.- Continued.

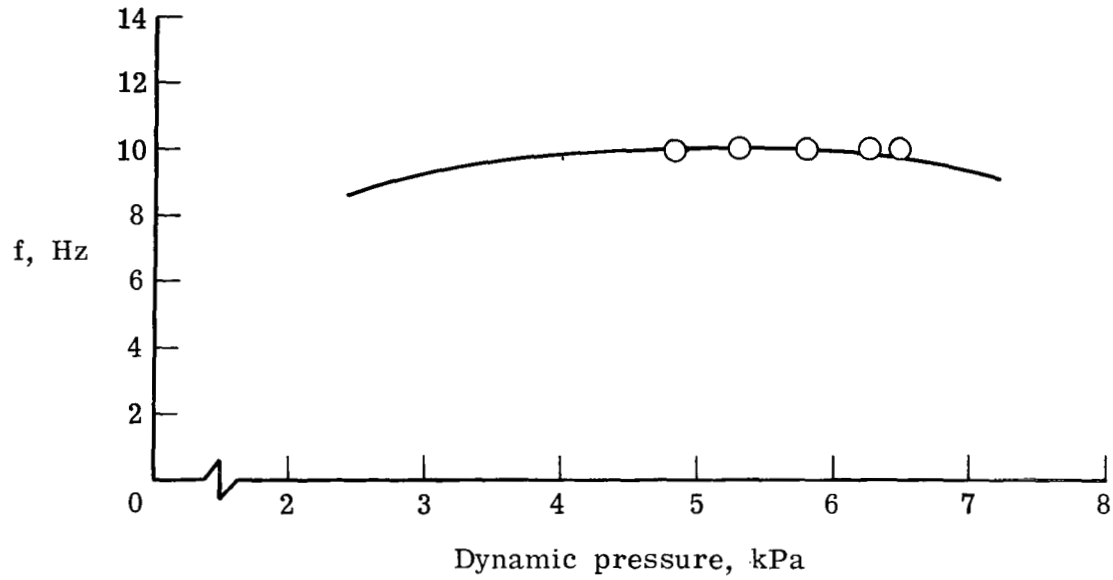

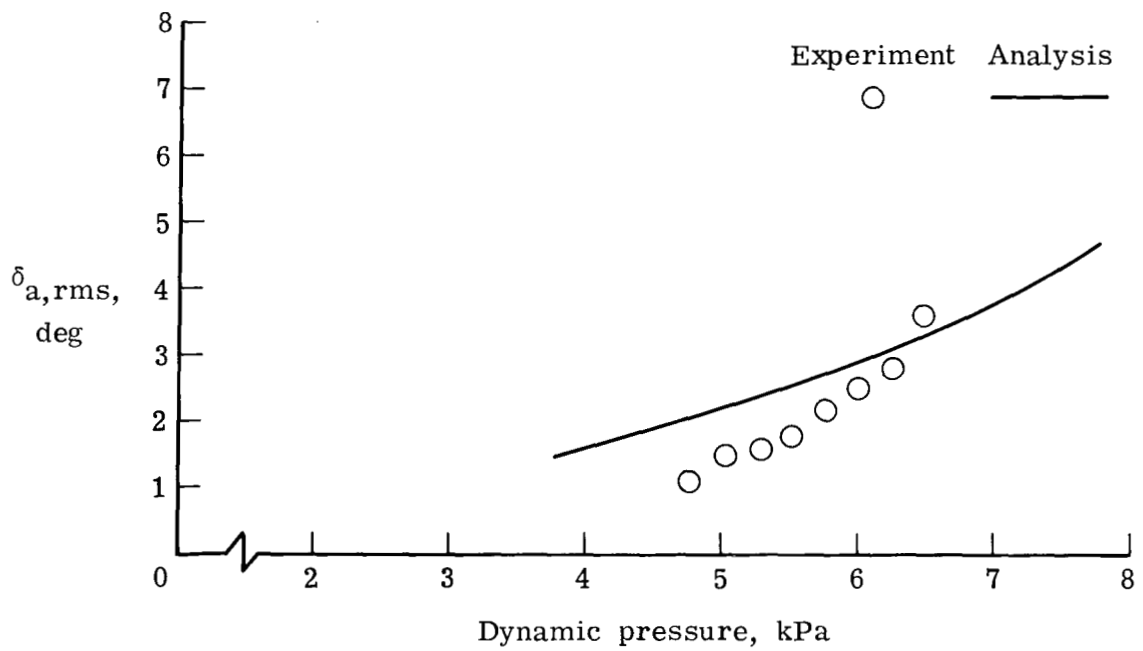

(c) M = 0.9.

Figure 22.- Continued.

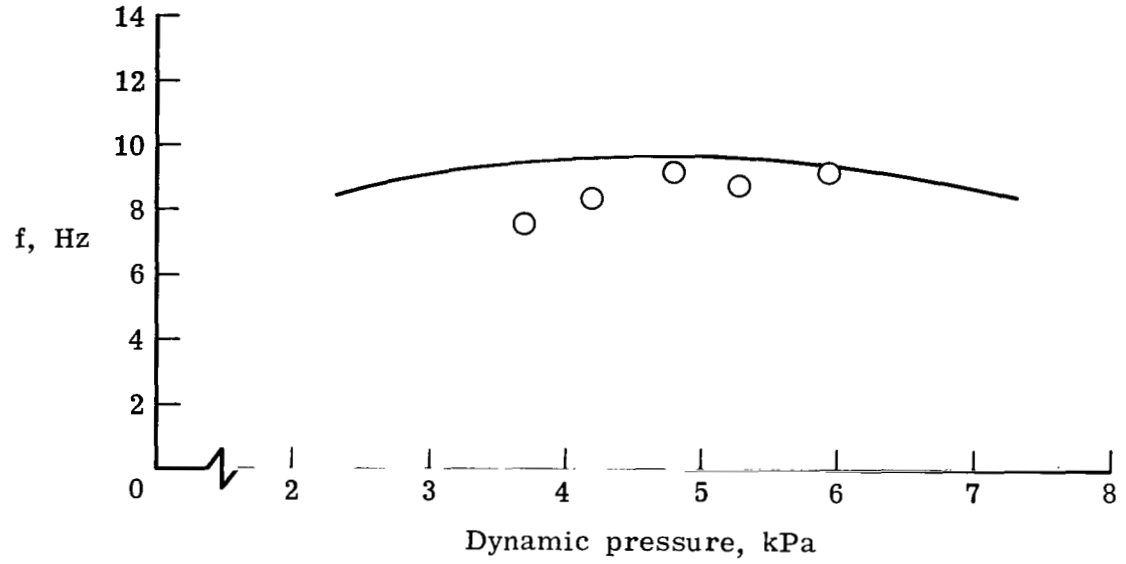

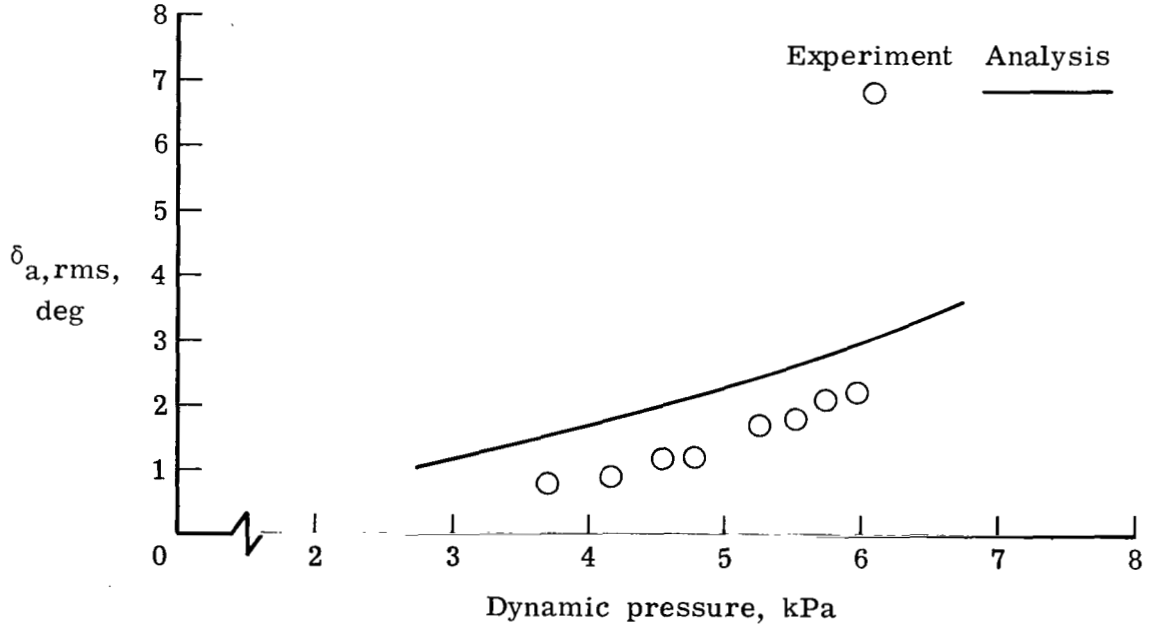

(d) M = 0.95.

Figure 22.- Concluded.

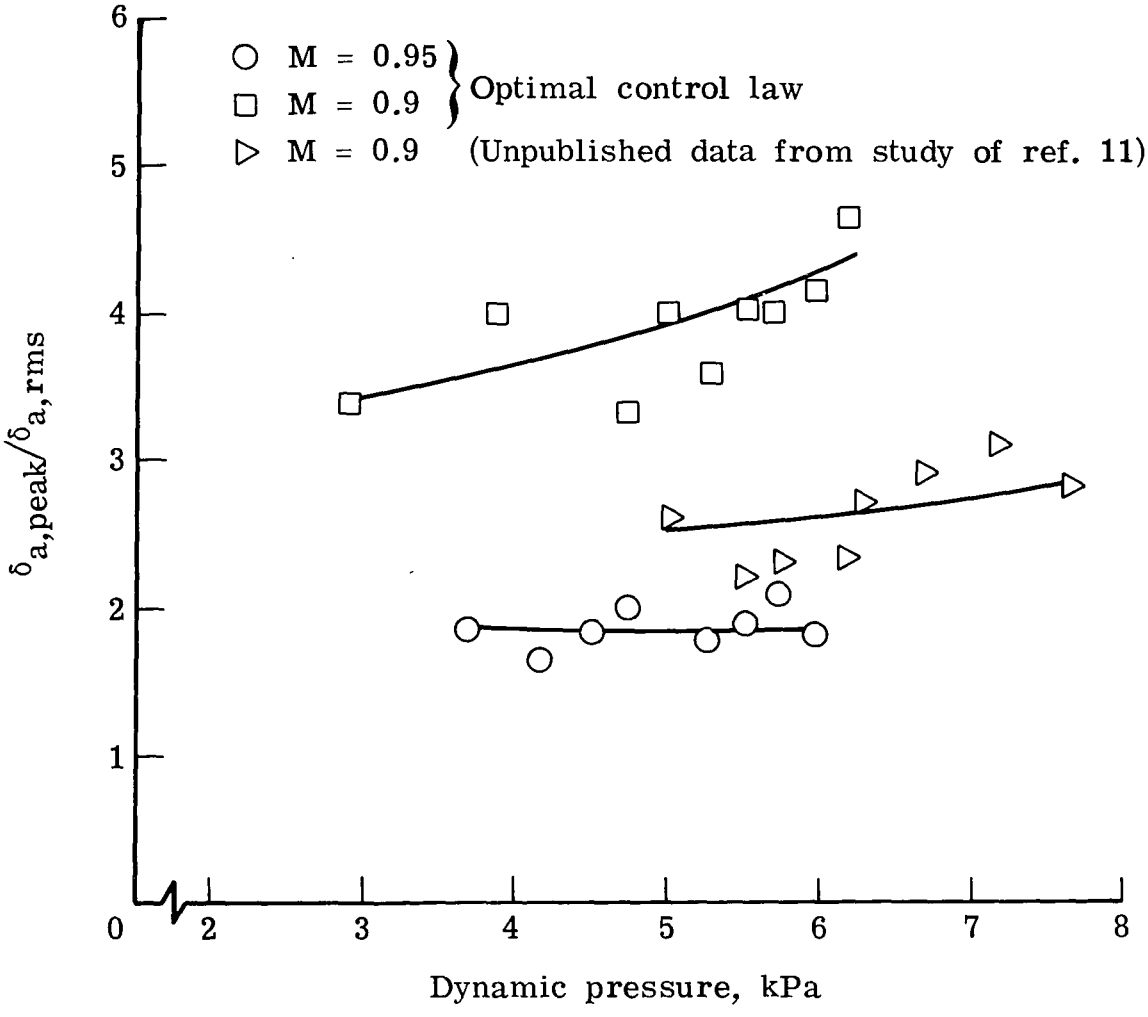

Figure 23.- Ratios of peak to rms control-surface deflection as function of dynamic pressure.

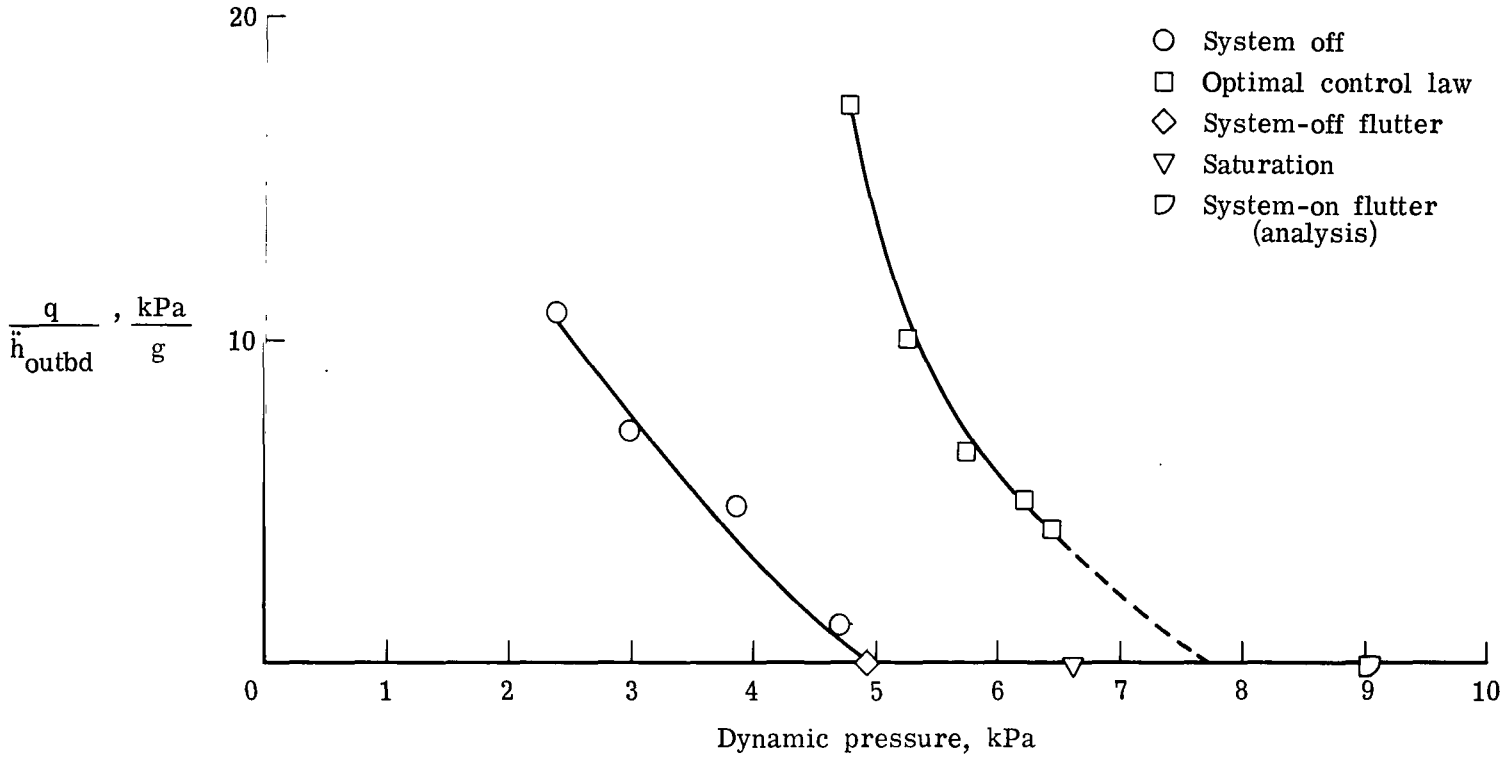

Figure 24.- Variation of inverse amplitude of acceleration at outboard accelerometer with dynamic pressure. M = 0.9.

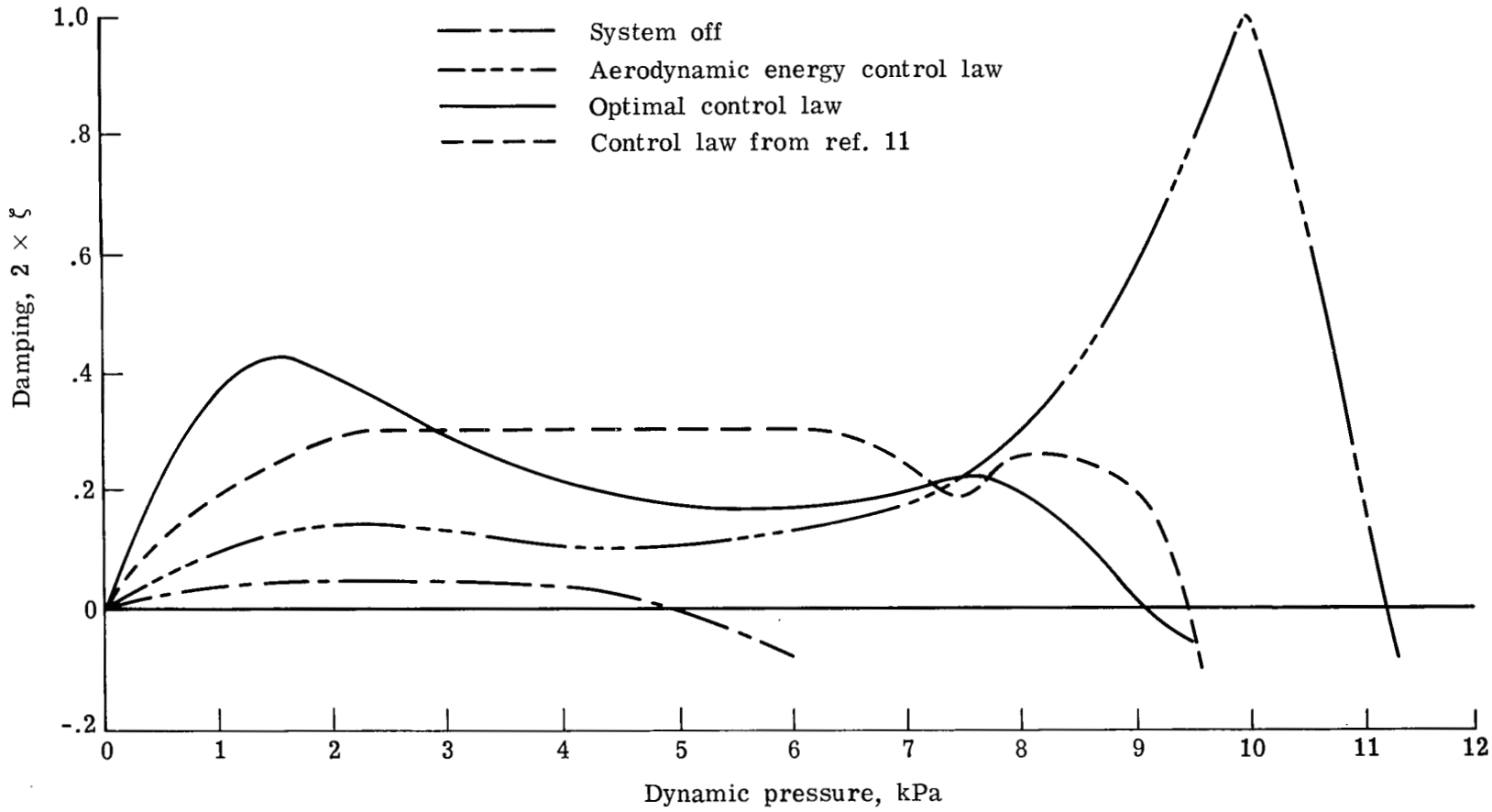

Figure 25.- Variation of calculated damping with dynamic pressure. M = 0.9.

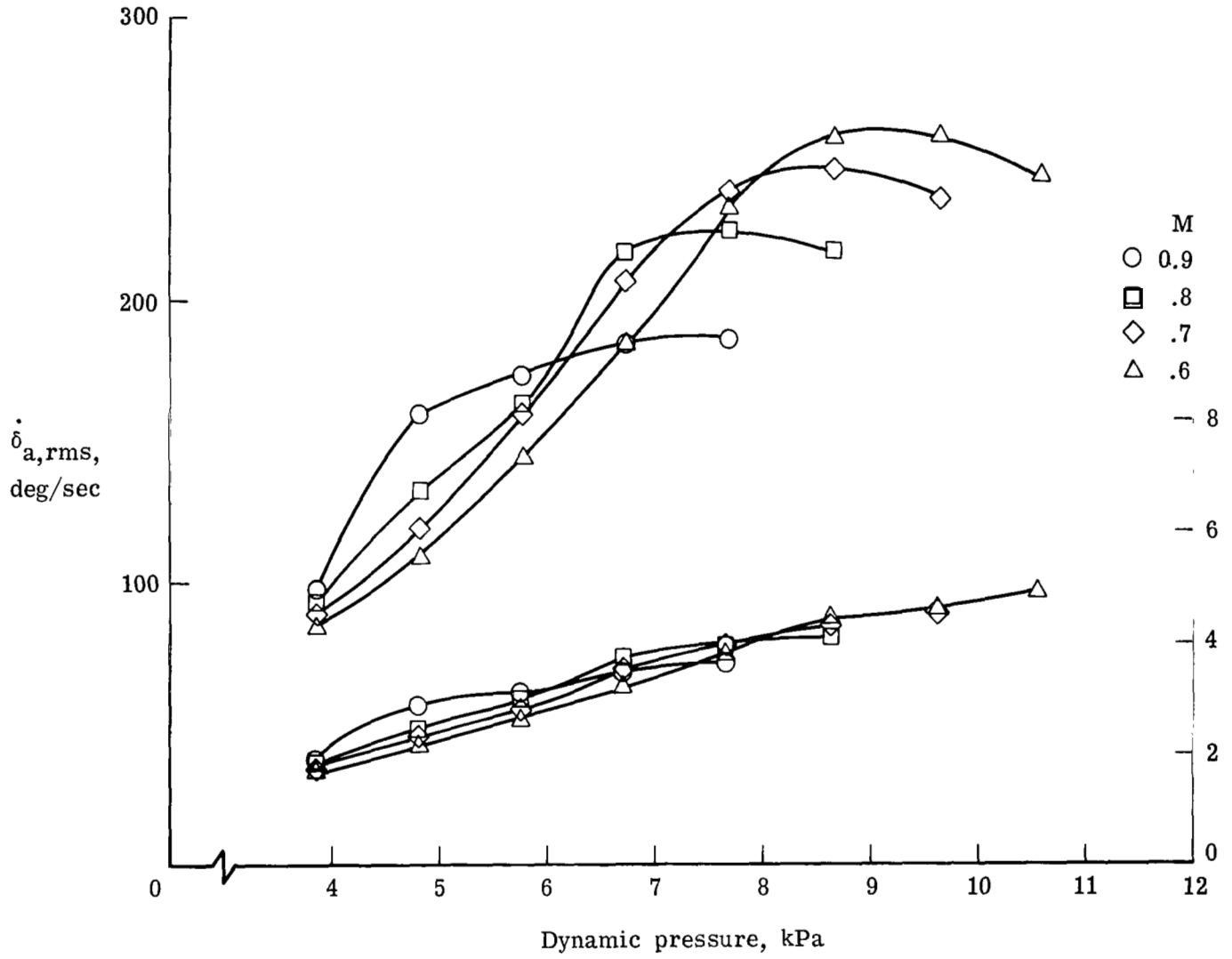

Figure 26.- Variation with dynamic pressure of rms response of control surface at various Mach numbers. (Control law defined by eq. (B1).)

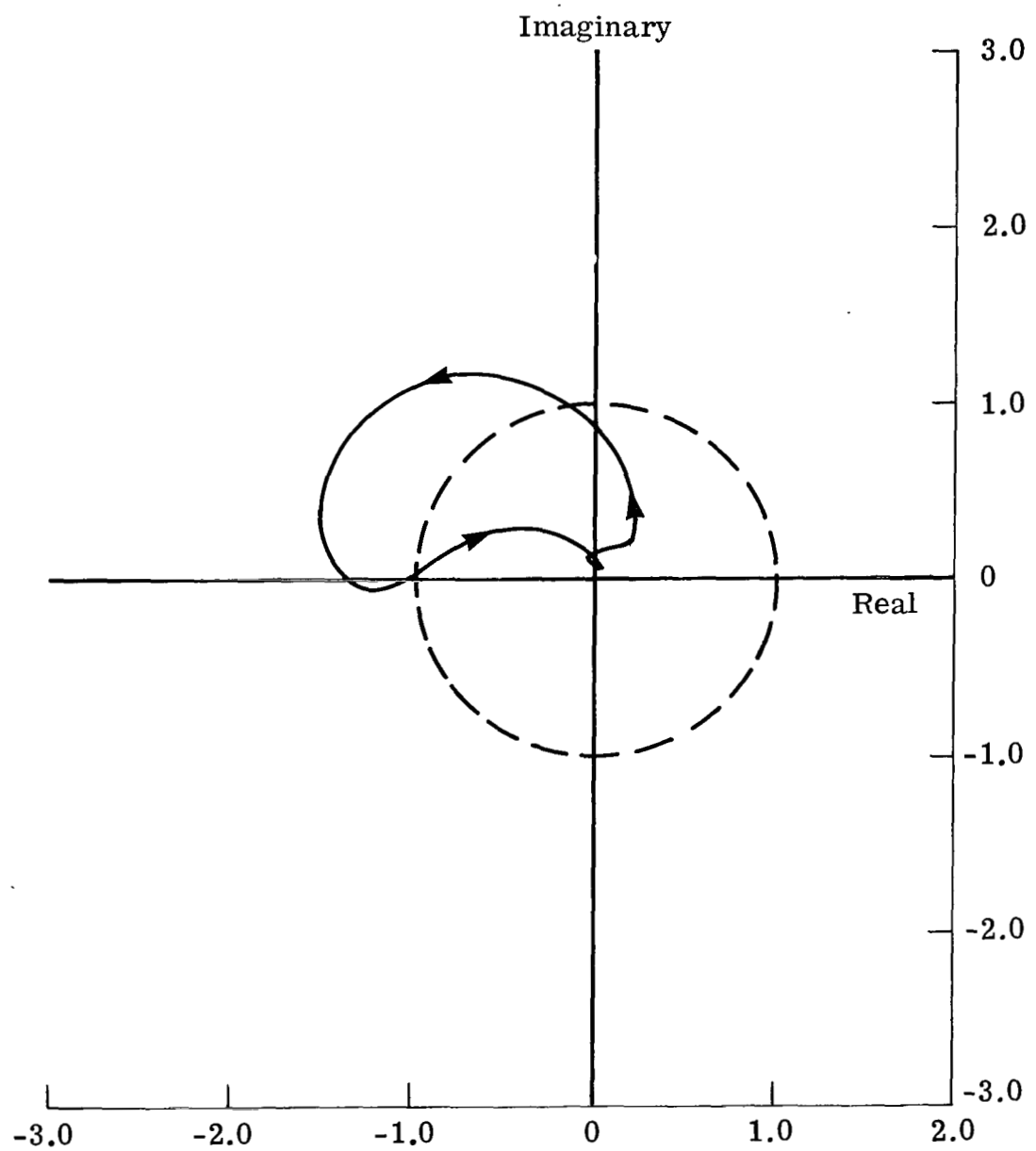

Figure 27.- Nyquist plot of open-loop transfer function $G(i\omega)\,H(i\omega)$ at design point. ($H(i\omega)$ defined by eq. (B1).)

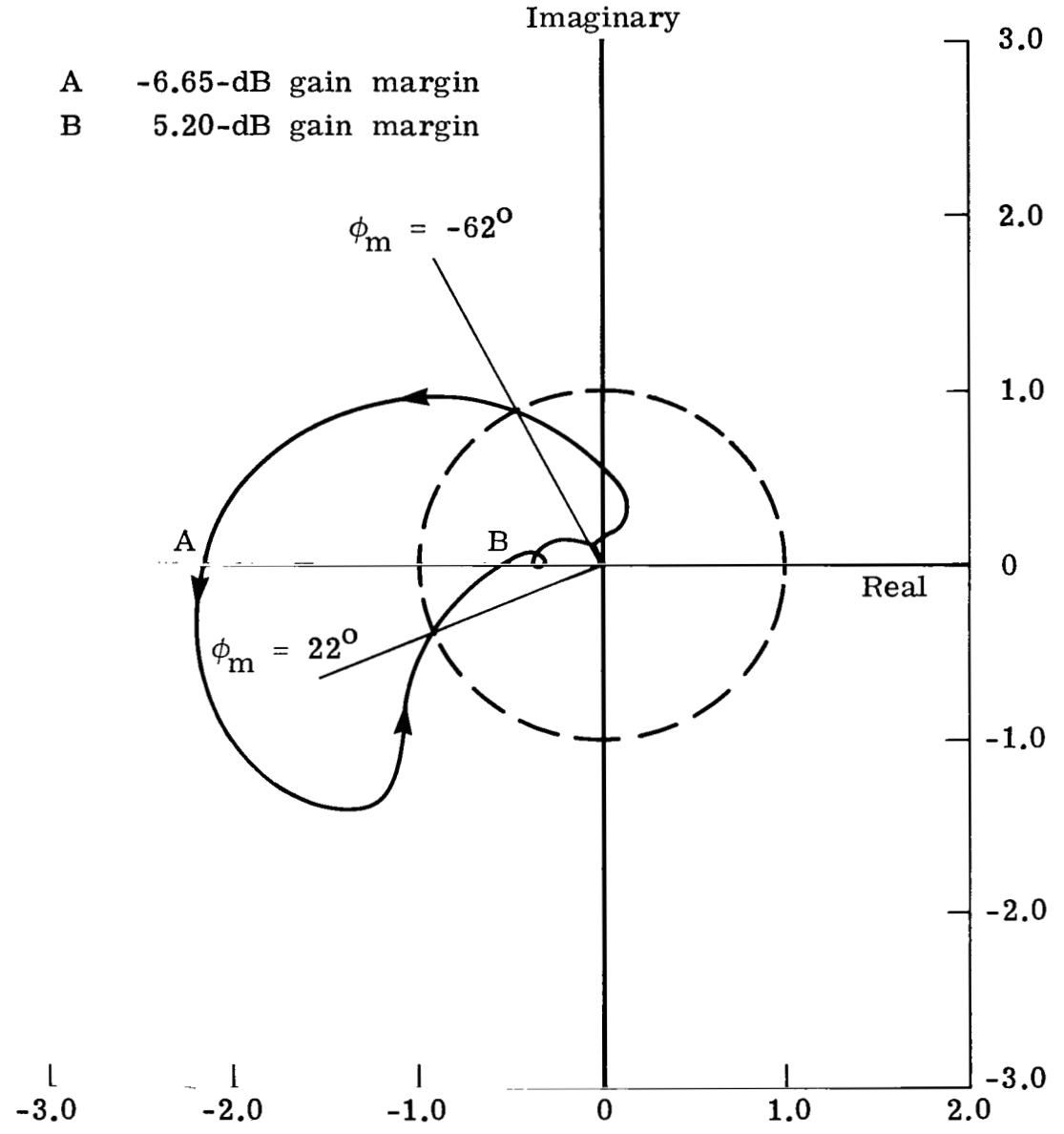

Figure 28.- Nyquist plot of open-loop transfer function $G(i\omega)\,H(i\omega)$. q_{max}; M = 0.9. ($H(i\omega)$ defined by eq. (B4).)

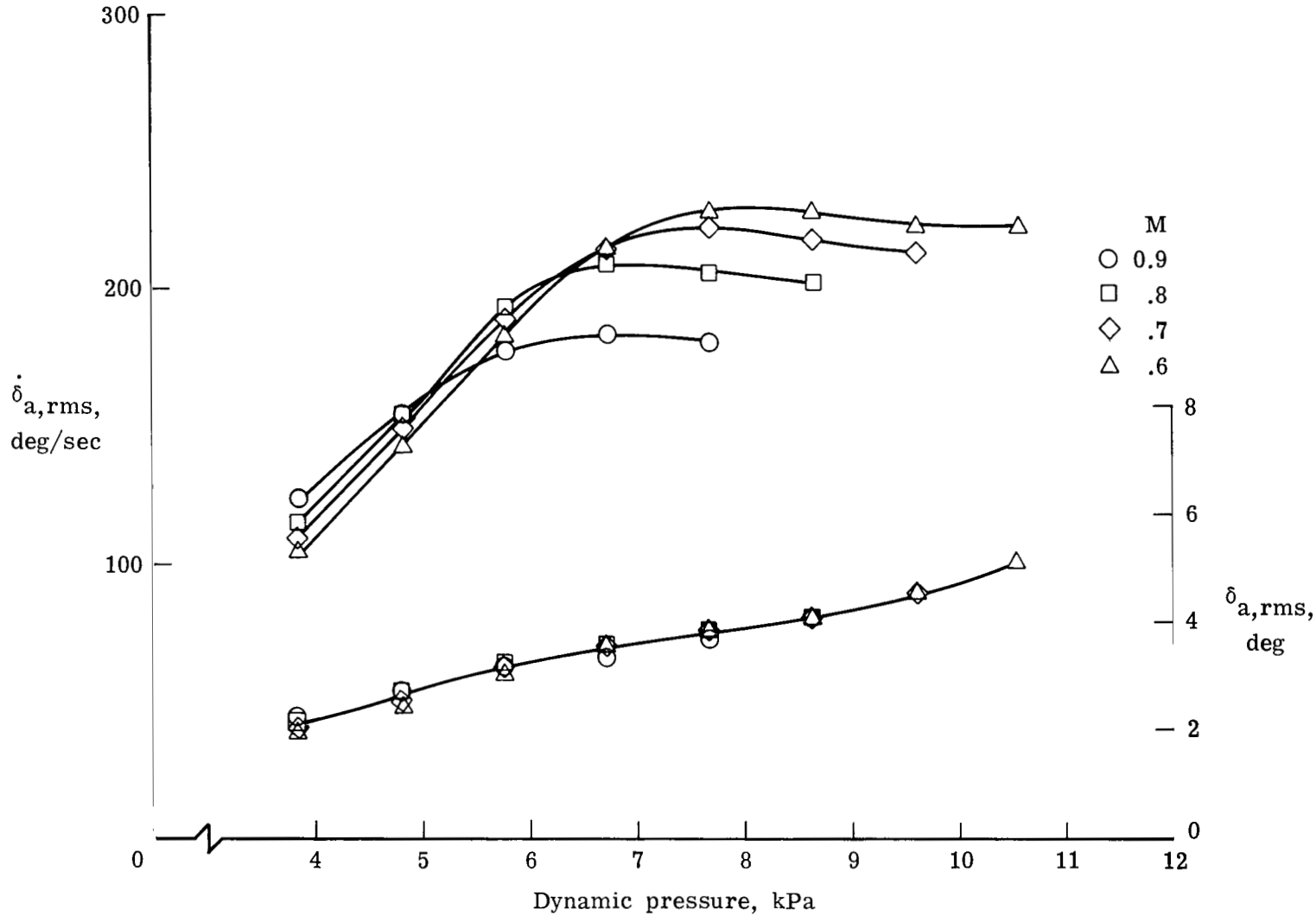

Figure 29.- Variation with dynamic pressure of rms response of control surface at various Mach numbers. (Control law defined by eq. (B4).)

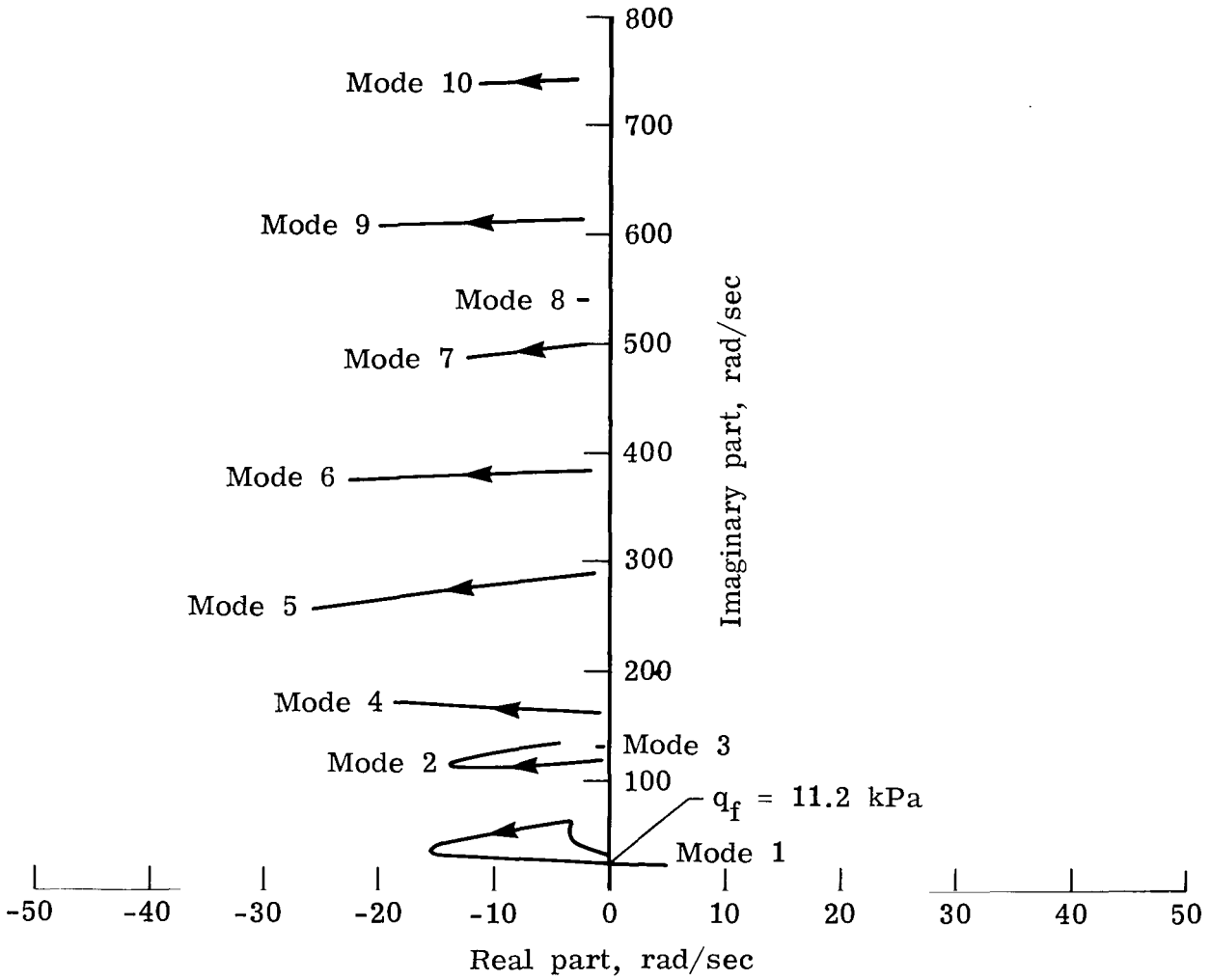

Figure 30.- Dynamic-pressure root locus at M = 0.9 for aerodynamic energy control law defined by equation (B4). (Arrows indicate increasing dynamic pressure.)

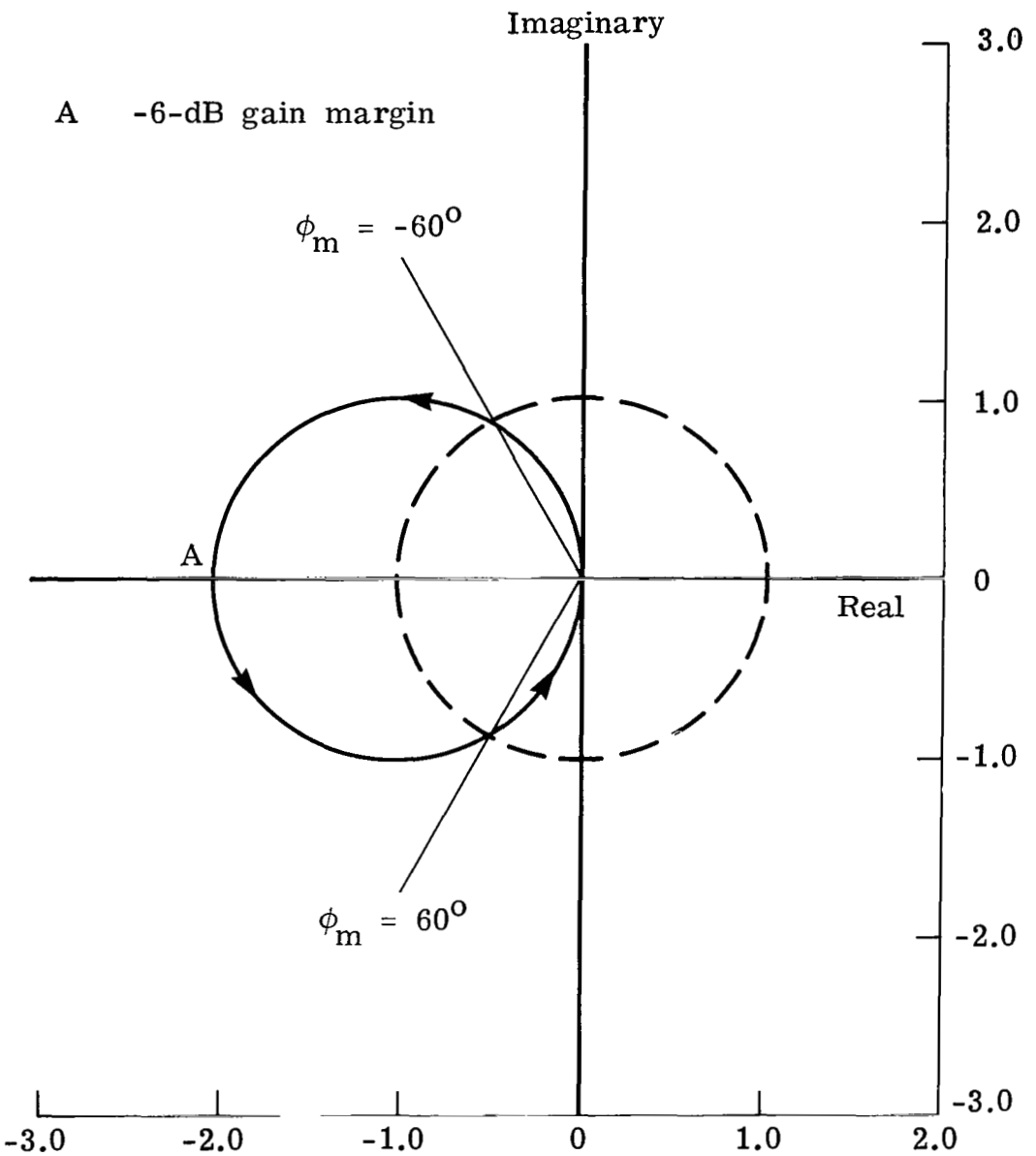

Figure 31.- Nyquist diagram of optimal full-state feedback control law. q_{max}; M = 0.9. (Arrows indicate increasing frequency.)

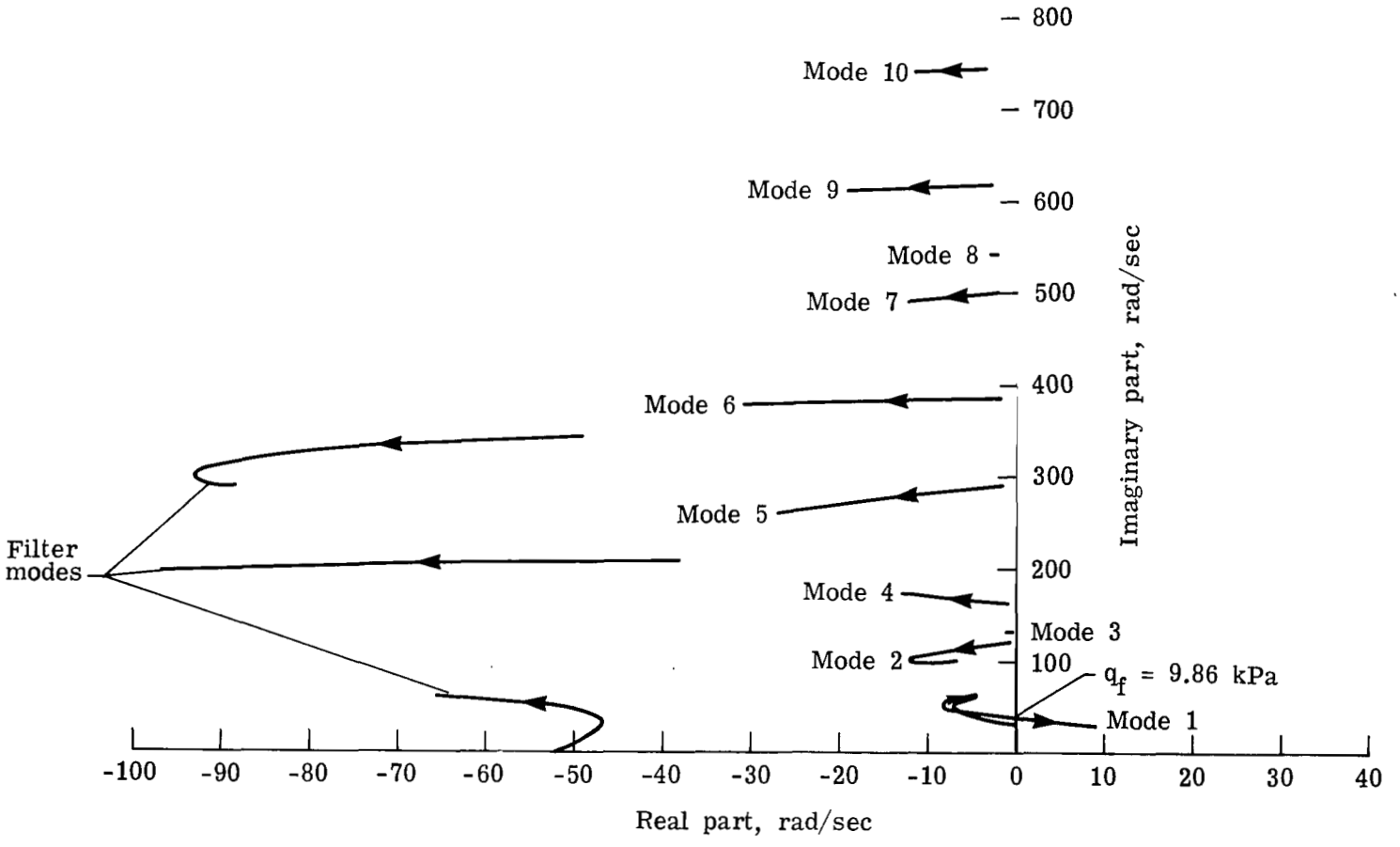

Figure 32.- Closed-loop root locus. (Control law defined by eq. (C4).)

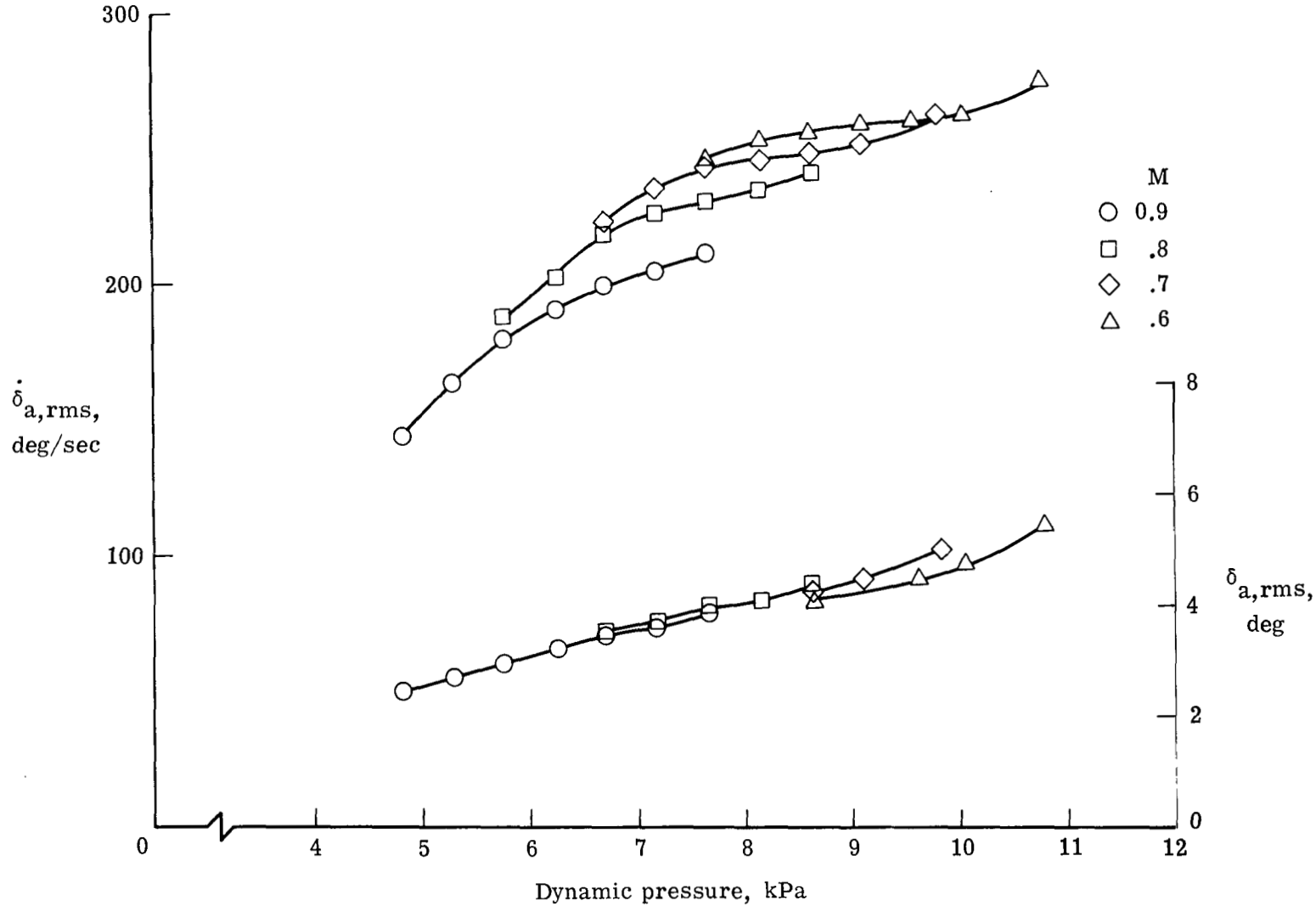

Figure 33.- Variation with dynamic pressure of rms response of control activity. (Control law defined by eq. (C4).)

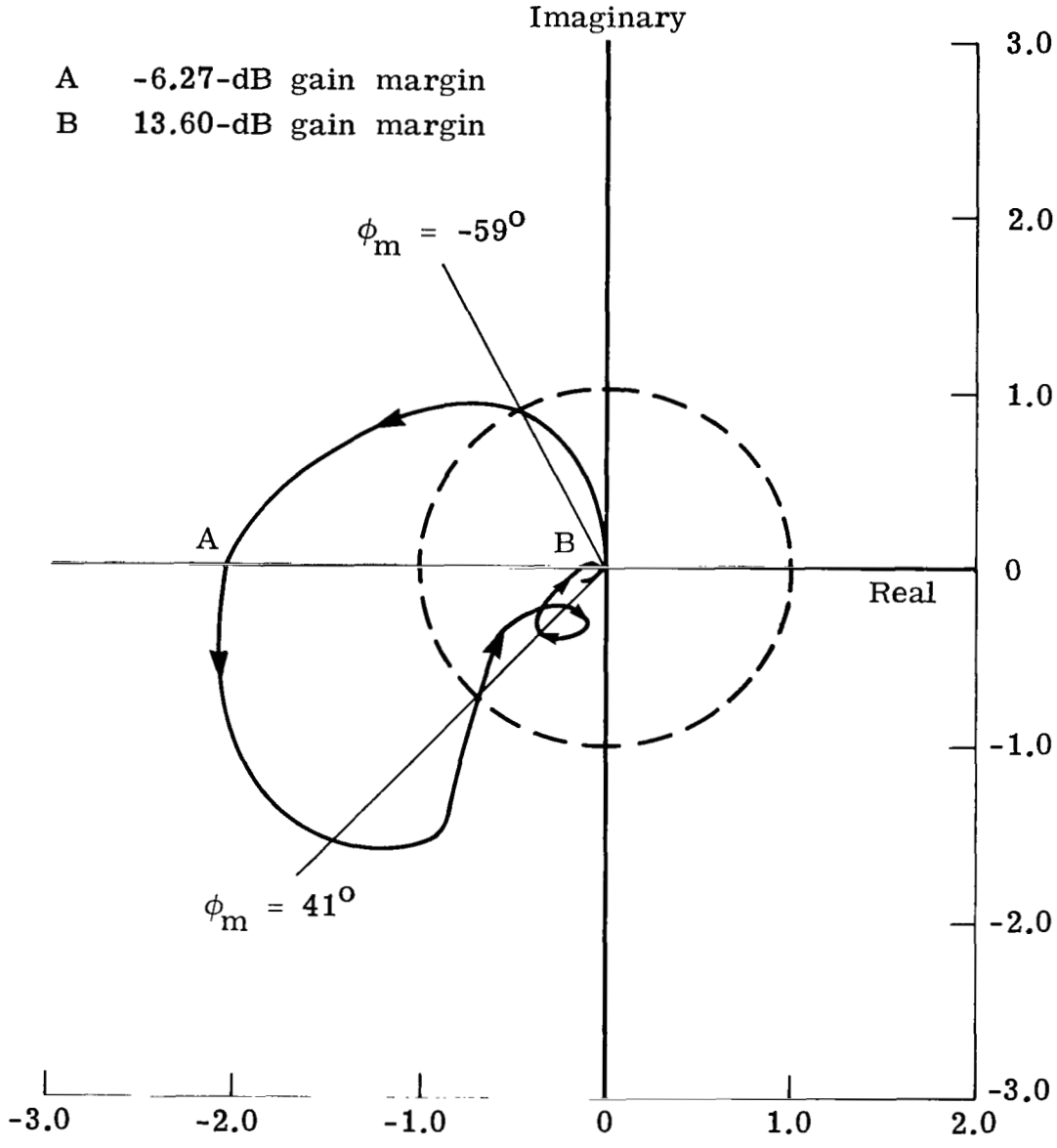

Figure 34.- Nyquist diagram of practical control law (eq. (C4)) that meets design requirements. q_{max}; M = 0.9. (Arrows indicate increasing frequency.)

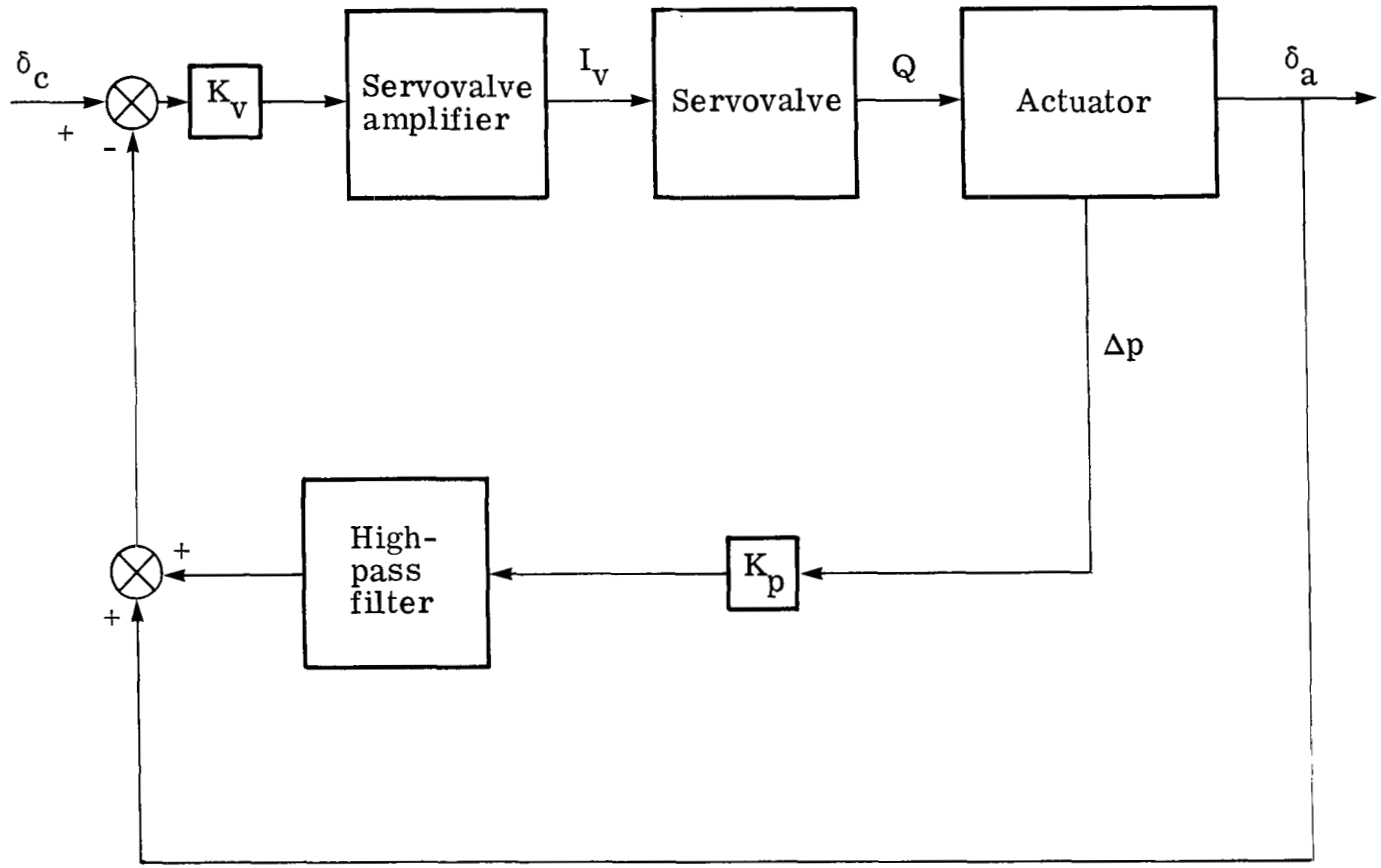

Figure 35.- Block diagram of actuator loop.

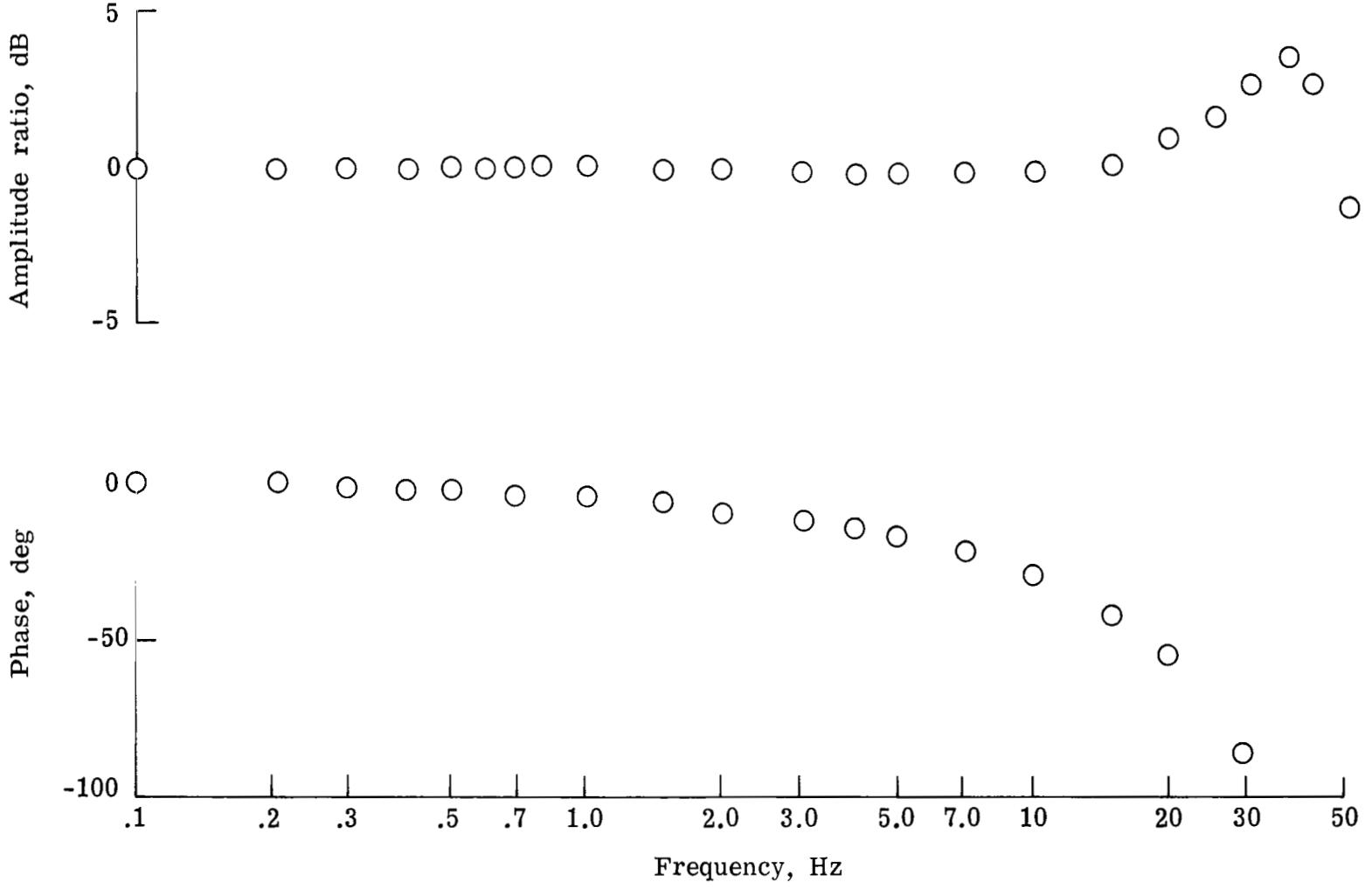

Figure 36.- Measured frequency response of actuator. K_v = 4.192 V/V; K_p = 0.760 μV/Pa; Input = 2 sin (ωt) deg.

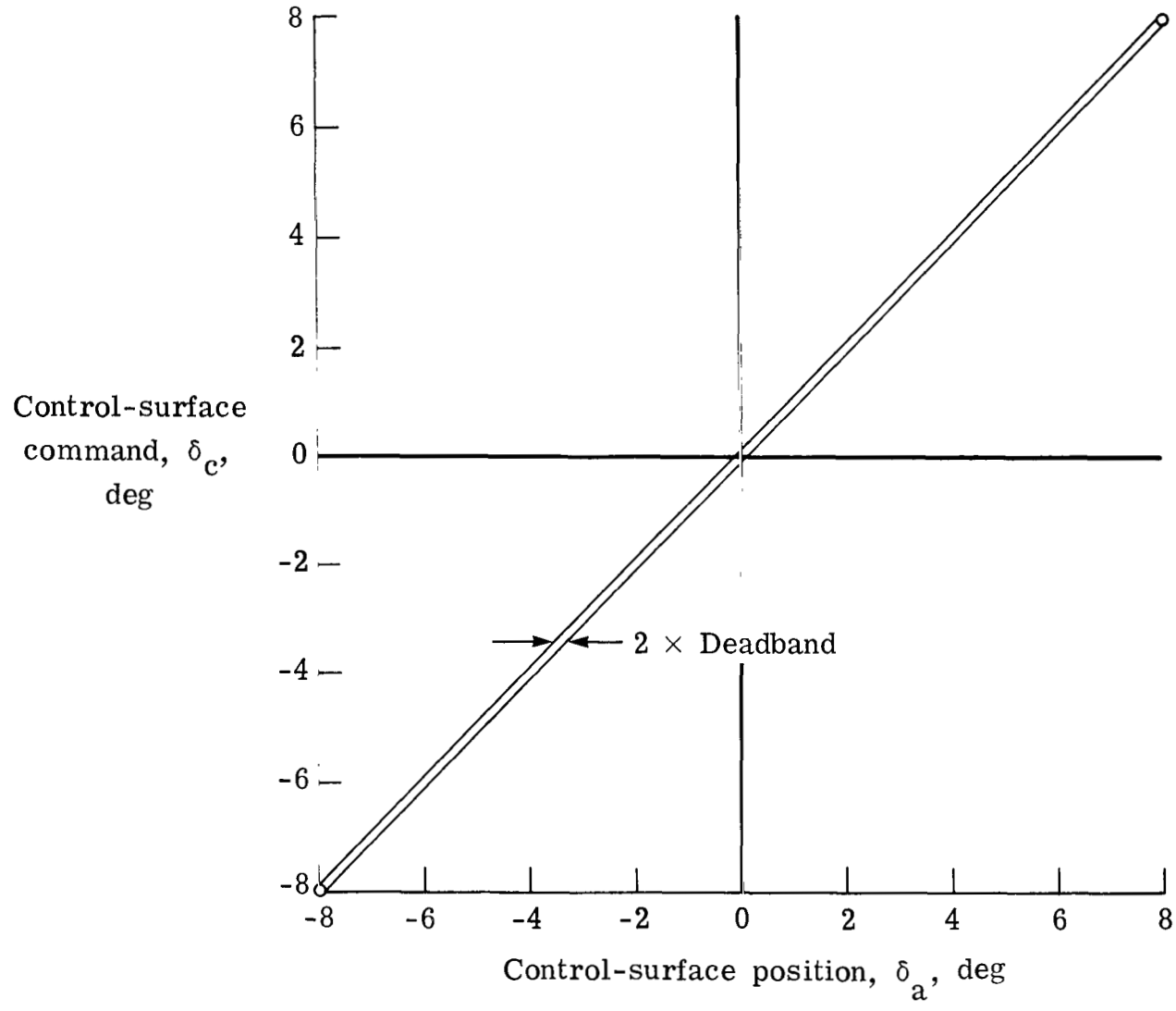

Figure 37.- Hysteresis of control-surface actuator loop.

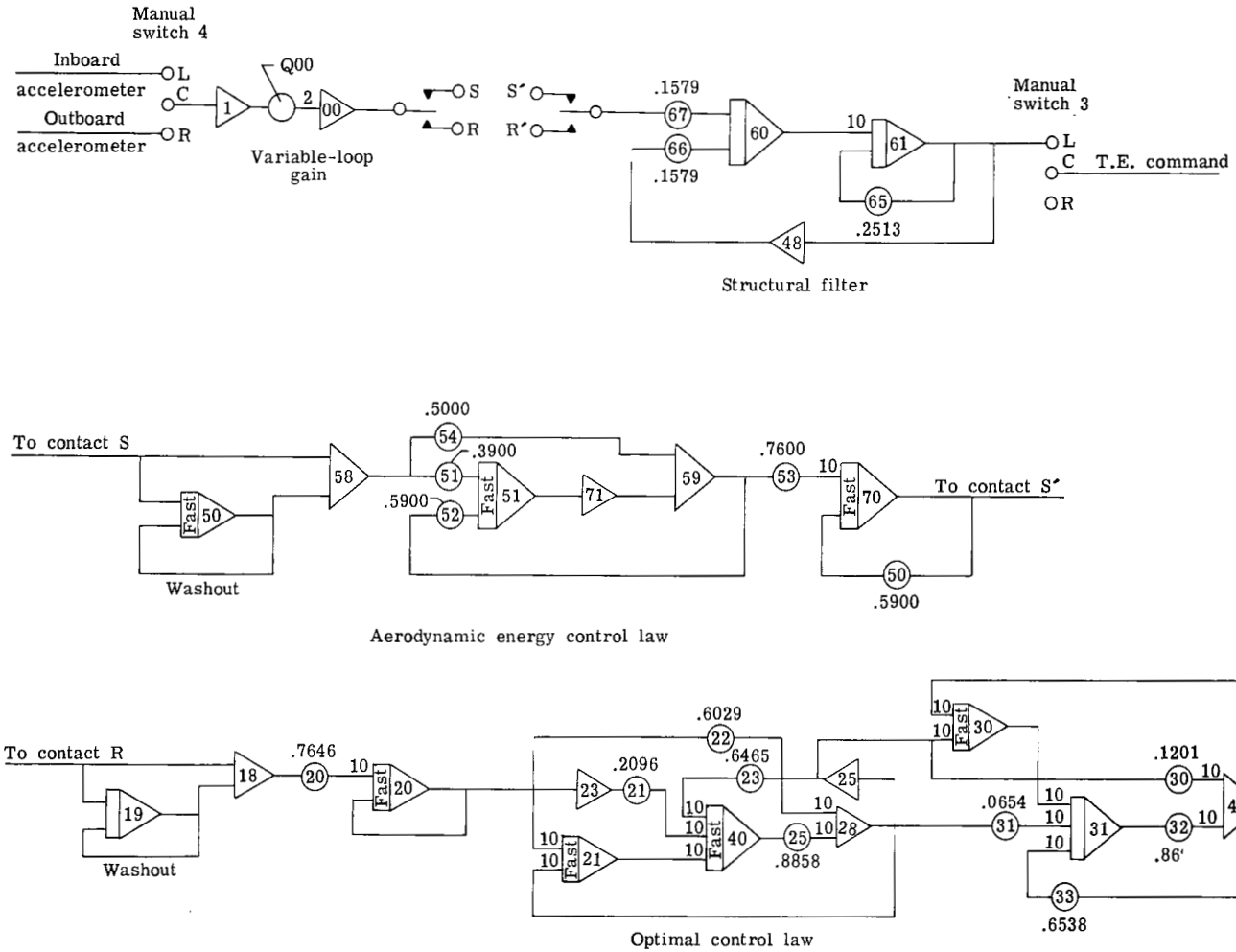

Figure 38.- Analog diagram of control-law mechanization.

1. Report No.	2. Government Accession No.	3. Recipient's Catalog No.
NASA TP-1653		

4. Title and Subtitle	5. Report Date
APPLICATION OF TWO DESIGN METHODS FOR ACTIVE FLUTTER SUPPRESSION AND WIND-TUNNEL TEST RESULTS	May 1980
	6. Performing Organization Code

7. Author(s)	8. Performing Organization Report No.
Jerry R. Newsom, Irving Abel, and H. J. Dunn	L-13177
	10. Work Unit No. 505-33-63-02

9. Performing Organization Name and Address	11. Contract or Grant No.
NASA Langley Research Center Hampton, VA 23665	
	13. Type of Report and Period Covered: Technical Paper

12. Sponsoring Agency Name and Address	14. Sponsoring Agency Code
National Aeronautics and Space Administration Washington, DC 20546	

15. Supplementary Notes

16. Abstract

The synthesis, implementation, and wind-tunnel test of two flutter-suppression control laws for an aeroelastic model equipped with a trailing-edge control surface are presented. One control law is based on the aerodynamic energy method, and the other is based on results of optimal control theory. Analytical methods used to design the control laws and evaluate their performance are described. The test objective was to demonstrate an increase in flutter dynamic pressure of at least 44 percent over a range of Mach numbers by using active flutter suppression. At Mach 0.6, 0.8, and 0.9, increases in flutter dynamic pressure were obtained but the full 44-percent increase was not achieved. However at Mach 0.95, the 44-percent increase was achieved with both control laws. Experimental results indicate that the performance of the systems is not so effective as that predicted by analysis. Also, the results indicate that wind-tunnel turbulence plays an important role in both control-law synthesis and demonstration of system performance.

17. Key Words (Suggested by Author(s))	18. Distribution Statement
Flutter suppression Aeroelasticity Analysis	Unclassified - Unlimited Subject Category 39

19. Security Classif. (of this report)	20. Security Classif. (of this page)	21. No. of Pages	22. Price*
Unclassified	Unclassified	81	$6.00

* For sale by the National Technical Information Service, Springfield, Virginia 22161

NASA-Langley, 1980

7 1 1U,D, 042180 S00903DS
DEPT OF THE AIR FORCE
AF WEAPONS LABORATORY
ATTN: TECHNICAL LIBRARY (SUL)
KIRTLAND AFB NM 87117